Johann Wolfgang Goethe-Universität

Frankfurt am Main

Institut für Theoretische Physik

Comparison of Kerr and dilaton black hole shadows: Impact of non-thermal emission
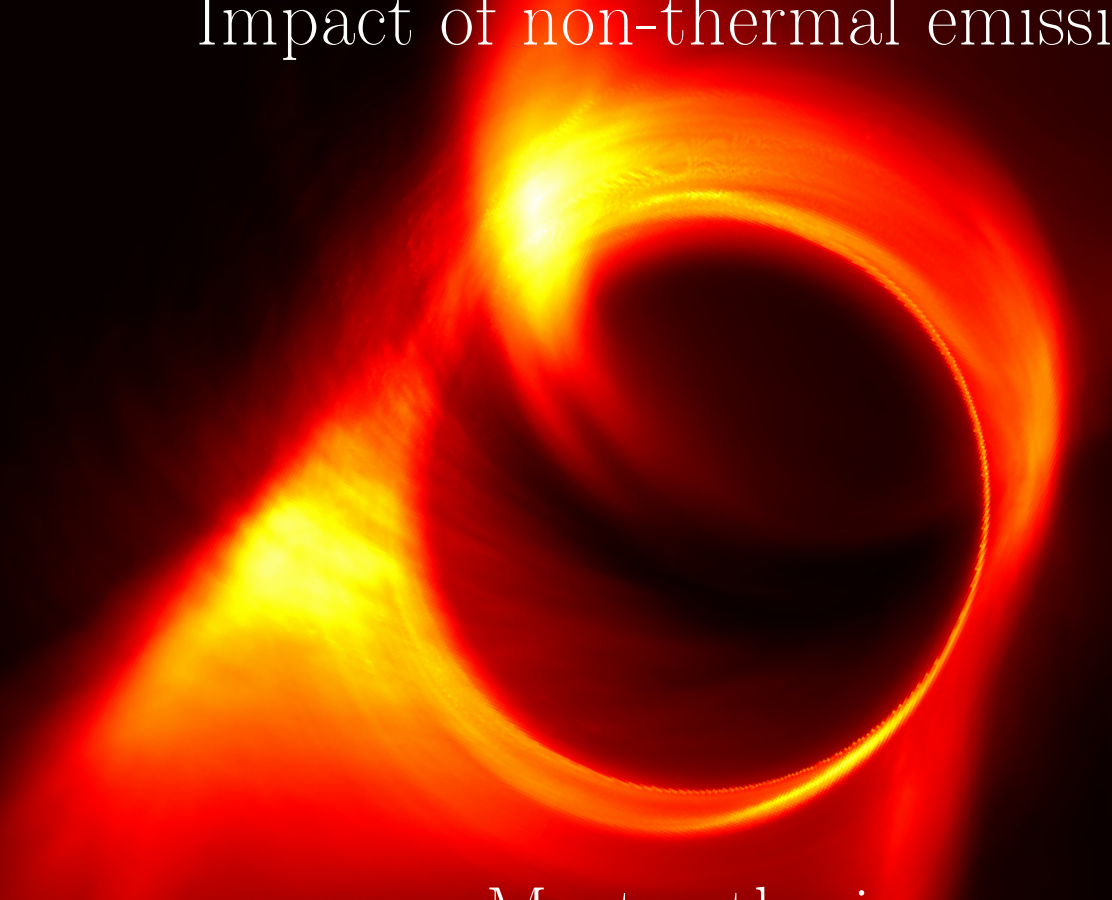
Master thesis
Jan Röder

Supervisor and first examiner:

Prof. Dr. Luciano Rezzolla

Advisor and second examiner:

Dr. Alejandro Cruz-Osorio

Contents

Abstract

With the Event Horizon Telescope, a very long baseline interferometry (VLBI) array, both temporal and spatial event horizon-scale resolutions needed to observe super-massive black holes were reached for the first time. Current open questions revolve around the type of compact object in the Galactic Center, plasma dynamics around it and emission processes at play. The main goal of this thesis is to assess whether it is possible to distinguish between two spacetimes by means of synthetic imaging, under the aspect of different emission models. Extending the studies conducted in the pioneering work of Mizuno *et al.* 2018, general relativistic radiative transfer (GRRT) calculations are carried out on general relativistic magneto-hydrodynamics (GRMHD) simulations of a Kerr and of a non-rotating dilaton black hole. The systems are matched at the innermost stable circular orbit, and both black holes are initially surrounded by a torus in hydrostatic equilibrium with a weak poloidal magnetic field. In order to investigate the plasma dynamics, GRMHD simulations were carried out using the "Black Hole Accretion Code" (BHAC). In the literature the ratio between the temperatures of simulated ions and radiating electrons is often taken to be a constant, while in reality it is expected to depend on plasma properties. In radiative post-processing with the code "Black Hole Observations in Stationary Spacetimes" (BHOSS) the temperature ratio was therefore parametrized. Additionally, in the jet wall, electrons are believed to be accelerated and should therefore be modeled with non-thermal electrons. To this end, both thermal and non-thermal electron energy distribution functions were employed. Lastly, images were reconstructed from synthetic VLBI data with the "eht-imaging" Python package to study how the effects of the emission models carry over to an observational environment. The most impactful result is the effect of the parameter R_{high} in the temperature ratio parametrization, splitting source structures into torus– and jet dominated configurations. Non-thermal emission turns out to be negligible at the field of view used and for the region it is applied in. Hence, given the present observational capabilities, it is unlikely that it is possible to distinguish spacetimes in observations. The striking visual differences are due to the difference in rotation between the black holes. In synthetic VLBI images, even the difference in shadow size is lost for most configurations. The situation may be improved in the future by a better VLBI array.

Acknowledgements

1 Astrophysical background

1.1 Supermassive black holes

When the first quasars were discovered in the early 1960s, studies of active galactic nuclei (AGN) started forming a prominent field in astronomy [1]. Up until then, observations restricted to optical wavelengths by for example Carl Seyfert in 1943 had insufficient impact for the field to get broad attention. The advances in radio astronomy during the 1950s then finally made it possible to advance AGN physics to the important part of astrophysical research it is today. From the mid-1960s and onward, accreting supermassive black holes were considered as explanation for the extreme energy output from quasars, albeit taking decades to receive broad support [1]. Until AGN surveys gave black hole accretion physics a stage, black holes had existed as merely theoretical constructs within Einstein's theory of general relativity. The first solution to Einstein's equations [2], carried out by Karl Schwarzschild in 1916, describes curvature around a point-like mass that does neither rotate nor is electrically charged. This solution, the so-called "Schwarzschild black hole", features a coordinate singularity at $2\,GM/c^2$, called the "Schwarzschild radius". In this solution, it coincides with the event horizon, from beyond which not even light rays can escape because the redshift diverges.

Over the past decades, more and more strong evidence for the existence of black holes was found, such as the movement of stars in the cluster located at the center of our own galaxy [3, 4]. These supermassive black holes residing in the hearts of most galaxies have masses in the range of about one million to billions of solar masses, and their origin is debated. Some assume that they formed in the early universe by direct collapse of large gas clouds [5–7], or that smaller black holes have merged together over time.

Of course there are also stellar-mass black holes created when massive stars explode in a supernova after burning up all their fusion material. The stellar core cannot withstand its own gravitational pull and collapses to a black hole. These stellar-mass black holes are regularly found in, for example, binary systems in the form of low-mass X-Ray binaries (LMXB) due to their characteristic X-Ray emission.

1.2 Accretion onto black holes

Matter accreting onto a massive (compact) object is believed to form an accretion torus or a disk around it. For a spinning accretor, this is likely to happen in the equatorial plane perpendicular to the spin axis.[1] Whether a disk or a torus is present mostly depends on the accretion rate onto the central object (from here on, a black hole). Both the accretion rate and the accretion luminosity are often expressed in terms of their "maximum" values, the Eddington accretion rate and luminosity:

$$L_{\text{Edd}} \equiv 4\pi GcM \left(\frac{m_p}{\sigma_{T,e}} \right) \approx 1.26 \cdot 10^{38} \left(\frac{M}{M_\odot} \right) \frac{\text{erg}}{\text{s}} \tag{1}$$

$$\dot{M}_{\text{Edd}} \equiv \frac{L_{\text{Edd}}}{c^2} \approx 1.39 \cdot 10^{17} \left(\frac{M}{M_\odot} \right) \frac{\text{g}}{\text{s}} \tag{2}$$

Both L_{Edd} and $\dot{M}_{\text{Edd}}$ are estimates calculated for purely spherical accretion onto the black hole, and Thomson scattering dominating the opacity. Moving away from this perfect scenario, the Eddington limit may be violated by non-spherical geometry of the system and other processes, as commonly found in astrophysical scenarios [10]. Accretion processes can therefore be divided into sub– and super-Eddington accretion.

With increasing accretion rate, the accretion luminosity emitted from the disk grows roughly as $L_{\text{acc}} = \varepsilon \dot{M}$ until $L_{\text{acc}} \approx L_{\text{Edd}}$. Then, the radiation pressure force becomes comparable with the gravitational force and the disk is inflated to a torus [11]. Introducing the relative thickness $h = H/r$ as the ratio of height H and radial position r, the different types of disks can be characterized as thin ($h << 1$), slim ($h \sim 1$) and thick disks ($h > 1$) [12].

In order to determine the structure and hydrodynamics of a disk or torus, a necessary ingredient is a prescription for fluid viscosity. For thin disks, Shakura and Sunyaev developed the alpha-disk model, characterizing angular momentum transport through the disk together with magnetic field and gas turbulence using a single dimensionless parameter α [13] parametrizing local viscosity [11]. While this model has since been extended to describe relativistic accreting systems [14] and continuously refined [15–17], it is not viable for thick disks or tori as required in this work. It is based on angular momentum transport as a local process, which is no longer true for accretion tori [11]: angular momentum is transported

---

[1]Systems where the spin axis of the accretor and the symmetry axis of the accreted material do not align have been studied as well ("tilted torus"), e. g. [8, 9].

by magnetic fields permeating the accretion flow, which is a non-local process. An important example for a process responsible for angular momentum transport is the "magneto-rotational instability" (MRI) [18–20]. In simulations of general relativistic magnetohydrodynamics (GRMHD) systems it is often triggered by a random excitation in the magnetic field to start the accretion process coming from a torus setup in hydrostatic equilibrium.

While a (GR)MHD code would technically need to solve for the distribution of angular momentum in the torus self-consistently, with both magnetic viscosity and accretion flow hydrodynamics taken into account, this work chooses a simplified approach. Angular momentum is set to be constantly distributed throughout the torus. That way, only the GRMHD equations need to be solved (the ideal gas equation of state is employed) [11, 21], as explained further in chapter 3.3.

1.3 Observations of the galactic center

In this work, the center of the Milky Way serves as the model system. In 1755 Immanuel Kant believed that a star, specifically Sirius, was located in the Galactic Center (GC) [22]. By the 20th century, it was clear that the GC was obscured by clouds of dust characteristic for the Milky Way band in the sky. Observations between soft X-ray and optical wavelengths are only possible in the so-called "Baade's Window", a small patch of sky with reduced dust on the line of sight.

In infra-red wavelengths, observations of the star cluster located in the central parsec provided strong evidence for the existence of a supermassive black hole in the GC (e. g. [3, 23–25]). For this effort, the Nobel Prize in Physics 2020 was awarded to Roger Penrose, Reinhard Genzel and Andrea Ghez.

While studying the star cluster already produced invaluable results such as mass of and distance to the black hole, the resolution of infrared telescopes is insufficient to resolve the direct vicinity. This is however necessary to study plasma dynamics and emission processes at play. In order to reach the desired resolution of $\sim 10\,\mu\text{as}$, very long baseline interferometry (VLBI) is required. Several interferometric GC observations at various frequencies have been carried out [26–31]; while suited for their respective studies, they lack either a sufficient coverage of the source and/or operate at a frequency so low that interstellar scattering dominates.

Resolving and observing the shadow cast by a black hole on its surroundings was theorized and methods were developed for over two decades (e. g. [32, 33]). With the Event Horizon Telescope (EHT), this effort finally became reality in 2019 with

the first-ever image of a supermassive black hole (namely, M 87* [34–39]). For the first time, emission from the direct vicinity of the event horizon of a low-luminosity AGN could be observed. The exact source of the observed synchrotron radiation is debated: it may be produced mainly in the torus (or disk), or in the jet [40–42]. This work focuses on calculations of said synchrotron radiation (or magneto-bremsstrahlung) [43]. Other emission mechanisms such as inverse Compton scattering or bremsstrahlung on ions will be part of future studies, as well as polarization and interstellar scattering of observed radiation.

2 VLBI techniques

2.1 Synthetic imaging

2.1.1 Interferometric measurements

General relativistic radiative transfer (GRRT) images, explained in section 4, provide important information on source morphology and radiative properties of the accretion flow. Since they can be calculated to arbitrary resolution, they however cannot be compared directly to actual observations. In order to assess whether it is possible to e. g. test general relativity by means of black hole imaging, as is the goal in this work, an observation has to be mimicked. In reality, systems like the central black holes of active galactic nuclei have very small angular sizes on the sky. The only way of observing such sources with the required micro-arcsecond resolution is by VLBI with, e. g., the EHT. Compared to GRRT data, these (mimicked) interferometric measurements account for effects caused by the reconstruction algorithm and can include e. g. interstellar scattering and station dependent noise.

In interferometry, a measurement of a source intensity distribution is carried out on a set of baselines, each formed by two antennas. On each baseline, both signals from the antennas are multiplied and averaged over by the "correlator". This leads to an output on each baseline proportional to the interferometric fringe function with an envelope depending on the bandwith pattern. Since in interferometry the observed angular distances on the sky are small, the bandwith pattern can safely be set to unity. Then, the interferometric output on each baseline is not proportional to the source intensity; rather, it is given by

$$ r\left(\vec{b}_{ij}, \vec{s}_0\right) = A_0 \Delta\nu \, |\mathcal{V}| \cos\left(2\pi\vec{b}_{ij}\cdot\vec{s}_0 - \phi_v\right), \tag{3} $$

with the baseline vector $\vec{b}_{ij}$ connecting the antennas, phase reference position on the sky $\vec{s}_0$, normalization factor for the antenna's power reception pattern A_0, bandwith $\Delta\nu$, visibility amplitude $|\mathcal{V}|$ and visibility phase ϕ_v [44]. The measured quantity is therefore not the source intensity distribution, but the complex visibility. The cosine term corresponds to the interferometric fringe function, and the visibility phase is measured relative to the fringe phase.

By the van Cittert-Zernike theorem, in a best-case scenario, the observed complex visibility is a 2D Fourier transform of the source intensity distribution $I(x, y)$

(where (x, y) are angular coordinates on the sky) [44]. However, an interferometer consists of a finite number of baselines $\vec{b}_{ij}$, each formed by stations i and j. Projecting these baseline vectors onto a plane orthogonal to the line of sight, the projections change their direction and length when Earth rotates. Since it is possible to orient the vector such that either one of the two telescopes on a baseline has the projected position $(u, v) = (0, 0)$, the projected endpoints of $\vec{b}_{ij}$ trace two point symmetric arcs in the $u - v$ plane. u and v are the projected baseline coordinates measured in wavelengths, often referred to as "spatial frequencies" [45]. All arcs traced during an observation together are called the "$u - v$ coverage", an incomplete sample of the $u - v$ plane. As an example, the coverage used in this work is shown in figure (1): each pair of point symmetric arcs w. r. t. $(u, v) = (0, 0)$ corresponds to one baseline, rotating around the earth. The arcs are color coded with the time during the observation to illustrate the "tracing" in the $u - v$ plane. The arcs are not continuous, but consist of individual points an interferometric output is recorded (or, where the $u - v$ plane is sampled). All stations partaking in the mimicked observation are listed in table 2. For a continuous measurement, the complex visibility reads

$$V \equiv \tilde{I}(u, v) = \int \int I(x, y) e^{-2\pi i (ux + vy)} \, dx \, dy \, . \tag{4}$$

On a single baseline $\vec{b}_{ij}$, a Gaussian thermal noise term ϵ_{ij} is often added to the single-baseline visibility V_{ij} to account for electronics, atmosphere and background noise. The result is again multiplied with one gain term $G_i \, e^{i\phi}$ per station describing signal processing upon reception, modifying amplitude and phase of the sampled Fourier transformed source intensity distribution. The single-baseline visibility V_{ij} then reads

$$V_{ij} = G_i \, G_j \, e^{i(\phi_i - \phi_j)} \left(\tilde{I}_{ij}(u, v) + \epsilon_{ij} \right) . \tag{5}$$

Note that in the above expression, $\tilde{I}_{ij}$ denotes only the u, v points actually sampled by the baseline $\vec{b}_{ij}$. The complex gain terms can conveniently be mostly removed from the measurement by introducing the so-called "closure quantities", explained below. In this work, for the sake of comparability the noise on all images must be the same. Therefore, no such random processes are employed and will instead be part of a future study. This includes interstellar scattering.

2.1.2 Closure quantities

In order to rid the imaging process of errors due to complex gains and calibration, two kinds of "closure quantities" can be employed: closure amplitudes, and closure phases. The former does not provide the total flux density, while the latter does not contain information about the absolute position of the image. These have to be constrained separately. Even though in this work the synthetic VLBI data set is not contaminated by random effects, the imaging algorithm is still based on closure quantities. The closure phase is the phase ψ of the bispectrum V_B around a triangle of stations:

$$V_B \equiv |V_B|\, e^{\mathrm{i}\psi} = V_{12}V_{23}V_{31}\,, \tag{6}$$

which is insensitive to station-based phase error [45].

Closure amplitudes, on the other hand, aim to cancel out the station-based gain terms G_i using four visibilities instead of three. Each set of four stations leads to three closure amplitudes $|V_C|_{a,b,c}$

$$|V_C|_a = \left|\frac{V_{12}V_{34}}{V_{13}V_{24}}\right|,\quad |V_C|_b = \left|\frac{V_{13}V_{24}}{V_{14}V_{23}}\right|,\quad |V_C|_c = \left|\frac{V_{14}V_{23}}{V_{12}V_{34}}\right|. \tag{7}$$

Both closure phases and amplitudes, while successfully removing station-based errors, are in reality still affected by thermal noise [44]. Even though they contain less information about the image, requiring additional constraints, and being potentially difficult to interpret physically due to mixing of Fourier components, closure phases and amplitudes are robust quantities desirable to use in image reconstruction.

2.2 The EHTIM package

Synthetic VLBI data is generated and reconstructions are carried out with the EHT-Imaging (EHTIM) python package by A. Chael *et al.* [45, 49]. The objective function (9) is minimized using the Limited-Memory BFGS algorithm [50] implemented in SciPy [51]. It is a quasi-Newton gradient descent method based on iterative approximation of the Hessian matrix to carry out the update of every pixel with respect to the gradient of the objective function.

In order to ensure the flux to be positive in each pixel, a change of variables $I_i = \exp \xi_i$ is employed, where $-\infty < \xi_i < \infty$. The data term gradients need to be adjusted accordingly. The image representation is continuous [45], and the

imaging algorithm is run repeatedly, where each input image is the output of the last run convolved with 30% of the beam size.

2.2.1 Image reconstruction

Images are reconstructed using the regularized maximum likelihood method, trying to find the image $\mathbf{I}$ minimizing the objective function $J(\mathbf{I})$. This section will follow closely the description by Chael *et al.* 2018 [45]. To generate a synthetic data set, trial visibilities are computed by directly Fourier transforming a GRRT image (see equation (8)) and sampling it based on the $u - v$ coverage.

The reconstruction algorithm then does not directly operate on the GRRT image, but procedurally modifies a "trial" image. First, a "prior" image is chosen consisting of a Gaussian intensity distribution with the desired total flux and reasonable spatial extent. This is the first instance of the trial image. From the trial image $\mathbf{I}$, the 2D array collapsed into a 1D vector of M pixels, N trial visibilities are computed as $\mathbf{V'}=\mathbf{AI}$ with a matrix

$$A_{pq} = e^{-2\pi \mathrm{i}(u_p x_q + v_p y_q)}, \tag{8}$$

with indices for pixel p and number of the visibility measurement q. The trial visibilities are again obtained by sampling this Fourier transformed trial image with the $u - v$ coverage. The objective function $J(\mathbf{I})$ reads

$$J(\boldsymbol{I}) = \underbrace{\sum \alpha_D \chi_D^2(\boldsymbol{I}, \boldsymbol{d})}_{\text{data terms}} - \underbrace{\sum \beta_R S_R(\boldsymbol{I})}_{\text{regularizers}}, \tag{9}$$

with weighting terms α_D and β_R, goodness-of-fit functions χ_D^2 and regularizing functions S_R. The weights are usually set manually to aid convergence of the algorithm. The data terms for closure quantities read

$$\chi_{\mathrm{cl\ phase}}^2 = \frac{2}{N_\psi} \sum_j \frac{1 - \cos(\psi_j - \psi_j')}{\sigma_{\psi j}^2}, \tag{10}$$

$$\chi_{\mathrm{cl\ amp}}^2 = \frac{1}{N_C} \sum_j \frac{(|V_{Cj}| - |V_{Cj}'|)^2}{\sigma_{Cj}^2}, \tag{11}$$

where $\sigma_{\psi j}^2$ and σ_{Cj}^2 are estimated variances of the respective values and N_ψ, N_C are the number of times the quantities were measured. Data terms may as well be constructed for visibilities, amplitudes or bispectra.

Further, four regularizer terms have been chosen, constraining entropy, total squared variation (TSV), total flux and image centroid.

$$S_{\text{entropy}} = -\sum_i I_i \log\left(\frac{I_i}{P_i}\right), \tag{12}$$

$$S_{TSV} = -\sum_l \sum_m \left[(I_{l+1,m} - I_{l,m})^2 + (I_{l,m+1} - I_{l,m})^2\right], \tag{13}$$

$$S_{\text{tot flux}} = -\left(\sum_i I_i - F\right)^2, \tag{14}$$

$$S_{\text{centroid}} = -\left(\sum_i I_i x_i - F\delta_x\right)^2 + \left(\sum_i I_i y_i - F\delta_y\right)^2. \tag{15}$$

The sums are always taken over all pixels. In the entropy regularizer, P_i are pixel values of a prior image. F is the total flux of the image, and (δ_x, δ_y) is the centroid position the interferometer is pointed at. In practice, the image centroid is set to be $(\delta_x, \delta_y) = (0,0)$ in the center of the image (x_i, y_i). In short, data terms work on convergence in visibility space, while regularizer terms work in intensity space. The goal is to minimize the χ^2 between the synthetic VLBI data set obtained from the GRRT image and visibilities calculated by Fourier transforming the trial image. Once the imaging algorithm is finished, the output is convolved with 30 % of the observing beam and used as input for the next iteration.

2.2.2 Imaging parameters

While the observational parameters were kept the same across all frequencies (86 GHz, 230 GHz, 340 GHz), each frequency requires its own array of stations or modified versions of the same array, leading to different beam size, antenna positions and $u - v$ coverage. At 86 GHz, the Global mm-VLBI Array (GMVA) with ALMA and ATCA was used, whereas the Event Horizon Telescope (EHT 2017) array was employed for 230 and 340 GHz. A full list of stations can be found in table 2.

While in Mizuno *et al.* 2018 (M18) the image reconstruction was carried out with BSMEM, this work makes use of EHTIM exclusively. For this reason, the scan length is no longer a free parameter. Further, at 230 GHz the PdB station did not partake in the EHT 2017 observing campaign of Sgr A* and other sources and was therefore removed from the list of stations used in M18. The observation time was increased from 6 h to 12 h in order for the European stations to have non-zero

on-source time and increasing the $u - v$ coverage. All other parameters were kept the same as in M18 (table 1).

2.3 Image comparison

There is a number of ways to describe the differences between two images, the most obvious one being a pixel-by-pixel difference in the image plane. The resulting image provides information on the visual differences, such as asymmetries of the torus and shadow geometries in the case of this work. In order to describe these differences, or rather the similarities, in a more quantitative manner, various "image comparison metrics" can be calculated.

The first comparison metric is the l^2 norm of the pixel-by-pixel differences between images I and K mentioned above. For the difference between the j-th pixels of each image $\Delta S_j = I_j - K_j$ out of N total pixels in one image:

$$||\Delta S_j||_{l^2} \equiv \left(\sum_{j=1}^{N} |I_j - K_j|^2 \right)^{\frac{1}{2}}, \tag{16}$$

where I_j and K_j are intensities of the j-th pixel of each image, respectively ($j \in \{1, \ldots, N\}$). Closely related to the l^2 norm is the mean square error (MSE), defined as

$$\text{MSE} = \frac{\sum_{j=1}^{N} |I_j - K_j|^2}{\sum_{j=1}^{N} |I_j|^2}, \tag{17}$$

Further, Wang et al. [46] proposed a similarity index between images based on the ability of the human visual system to recognize structures within them. The similarity is a function of the luminance l, contrast c and structure s of both images I and K:

$$S(I, K) = f(l(I, K), c(I, K), s(I, K)). \tag{18}$$

$S(I, K)$ satisfies three conditions: symmetry in I and K, boundedness ($S(I, K) \leq 1$) and $S(I, K) = 1$ only if $I_j = K_j$, $\forall j$. The luminance and contrast functions are

also functions of the mean intensities $\mu_{I,K}$ and standard deviations $\sigma_{I,K}$:

$$\mu_X = \frac{1}{N} \sum_{j=1}^{N} X_j \,, \tag{19}$$

$$\sigma_X = \left(\frac{1}{N-1} \sum_{j=1}^{N} (X_j - \mu_X)^2 \right)^{\frac{1}{2}} \,, \tag{20}$$

where $X = I, K$. For the structure comparison, an additional deviation function is needed:

$$\sigma_{IK} = \frac{1}{N-1} \sum_{j=1}^{N} (I_j - \mu_I) (K_j - \mu_K) \,. \tag{21}$$

The three comparison functions, as defined in [46], read

$$l(I,K) = \frac{2\mu_I \mu_K + C_1}{\mu_I^2 + \mu_K^2 + C_1}, \quad c(I,K) = \frac{2\sigma_I \sigma_K + C_2}{\sigma_I^2 + \sigma_K^2 + C_2}, \quad s(I,K) = \frac{\sigma_{IK} + C_3}{\sigma_I \sigma_K + C_3}. \tag{22}$$

While $C_3 = C_2/2$ [46], C_1 and C_2 remain in the final result, called structural similarity index (SSIM)

$$\text{SSIM}(I,K) = \left(\frac{2\mu_I \mu_K + C_1}{\mu_I^2 + \mu_K^2 + C_1} \right) \left(\frac{2\sigma_{IK} + C_2}{\sigma_I^2 + \sigma_K^2 + C_2} \right). \tag{23}$$

The constants are supposed to avoid instabilities in the case of otherwise very small denominators. For this work, a simplified form [47, 48] is adopted, setting $C_1 = C_2 = 0$. Further, to be more consistent with the MSE, instead of the SSIM the structural dissimilarity index (DSSIM) is calculated,

$$\text{DSSIM}(I,K) = \frac{1}{|\text{SSIM}(I,K)|} - 1 \,, \tag{24}$$

so that both image metrics are equal to zero for identical images. For the same reason, the third image metric used in this work, the normalized cross-correlation (NCC),

$$\text{NCC}(I,K) = \frac{\sum_{j=1}^{N} (I \cdot K)_j}{\left(\sum_{k=1}^{N} (I^2)_k \cdot \sum_{l=1}^{N} (K^2)_l \right)^{\frac{1}{2}}} \,, \tag{25}$$

is always reported as $1 - \text{NCC}$. Here, I and K are the images in matrix form, every bracket therefore contains a simple matrix multiplication, with the sum again taken over a super-index of all pixels.

scan length/s	(420)
integration time/s	12
off-source time/s	600
date	April 7, 2017
start time	04:00:00 (08:30:00) (UT)
end time	16:00:00 (14:30:00) (UT)
bandwidth	4096 MHz

Table 1: Synthetic imaging observational parameters in M18 and the present work. In brackets: M18 parameters.
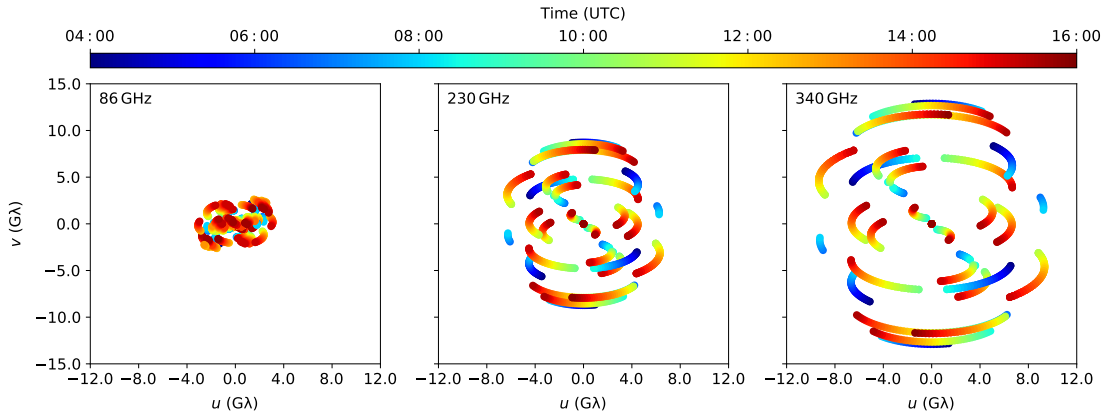
Figure 1: $u - v$ coverage for the simulated observation campaign at 86, 230 and 340 GHz.

GMVA, 86 GHz	EHT 2017, 230 GHz (340 GHz)
North Liberty (NL)	South Pole T. (SPT)
Fort Davis (FD)	Sub-Millimeter T. (SMT)
Los Alamos (LA)	Sub-Millimeter A. (SMA)
Kitt Peak (KP)	J. C. Maxwell T. (JCMT)
Owens Valley (OV)	PV
Brewster (BR)	LMT
Mauna Kea (MK)	ALMA
Plateau de Bure (PdB)	At. Pathfinder Experiment (APEX)
Pie Town (PT)	
OAN (Yebes, YB)	
Green Bank T. (GBT)	
Pico Veleta (PV)	
OSO (Onsala, ON)	
Metsähovi (MET)	
Large Millimeter T. (LMT)	
At. Large Millimeter A. (ALMA)	
Australia T. Compact A. (ATCA)	

Table 2: All stations partaking in mimicked observations. "T.": Telescope, "A.": Array, "At.": Atacama.
Taken from: https://github.com/achael/eht-imaging/tree/master/arrays

3 Mathematical background

In 1905, Albert Einstein first proposed a concept of relativity as an explanation for some phenomena observed in Maxwellian electrodynamics. Namely, if in a magnet-concductor system either one is moving, an electric current can be measured in the conductor. This could not be explained by well-established Newtonian electrodynamics. Taking the speed of light to be constant regardless of the emitter's movement and employing the so-called principle of covariance, Einstein arrived at a Maxwellian theory free of contradictions [52]. Additionally, the concept of an "aether" filling empty space became naturally obsolete. The principle of covariance, often referred to as "equivalence principle", states that any physical law must hold independently of the coordinate choice. More precisely, it must hold in all inertial systems. A little over a decade later Einstein had generalized his theory of relativity to include gravity. Coming from his theory of special relativity, he added what today is known as the Einstein equivalence principle, stating that gravitational forces and accelerations are indistinguishable. Further, non-gravitational experiments yield identical results regardless of position and movement in a gravitational field, as long as the experiment takes place locally [53]. The full theory of general relativity was published in 1915 and 1916 (e.g. [2,54]) with the Einstein field equations as most important (and famous) result. Essentially, they describe how presence of matter affects curvature of spacetime, and in turn how spacetime curvature affects kinematics of matter:

$$R_{\mu\nu} - \frac{1}{2}R\,g_{\mu\nu} + \Lambda\,g_{\mu\nu} = 8\pi\,T_{\mu\nu}\,. \tag{26}$$

The first two terms, often abbreviated to $G_{\mu\nu}$ (the "Einstein tensor"), contain the Ricci tensor $R_{\mu\nu}$, Ricci scalar R and determinant g of the spacetime metric $g_{\mu\nu}$. Λ is called cosmological constant and set to zero for this work, however it is important in cosmological studies. On the right hand side, the energy-momentum tensor $T_{\mu\nu}$ includes all matter and energy terms needed to describe the system.

3.1 Black hole spacetimes

3.1.1 Isolated spinning black hole

The first of two spacetimes compared in this work is the well-known Kerr metric originally introduced in 1963 [55]. In Boyer-Lindquist coordinates the line element reads (t, r, θ, ϕ) [56]:

$$ds^2 = -\left(1 - \frac{2Mr}{\Sigma}\right) dt^2 - \frac{4Mra\sin^2\theta}{\Sigma} \, dt \, d\phi + \frac{\Sigma}{\Delta} \, dr^2 + \Sigma \, d\theta^2 + \frac{A}{\Sigma} \sin^2\theta \, d\phi^2, \quad (27)$$

where the metric functions are

$$\Sigma = r^2 + a^2\cos^2\theta, \quad \Delta = r^2 - 2Mr + a^2, \quad A = \left(r^2 + a^2\right)^2 - a^2\Delta\sin^2\theta, \quad (28)$$

with the spin parameter $a = J/M$ and angular momentum J and $0 < a < 1$. In the limiting case $a \to 0$, (27) reduces to the Schwarzschild metric for non-rotating black holes.

While in the Schwarzschild spacetime the characteristic radii (event horizon (EH), photon orbit (PO) and innermost stable circular orbit (ISCO)) take on values of $2\,\mathrm{M}$, $3\,\mathrm{M}$ and $6\,\mathrm{M}$, they depend on the spin parameter for a rotating black hole. Moreover, surfaces of infinite redshift no longer coincide with the event horizon and both are again split in two [56]:

$$r_{\mathrm{s},\pm} = M \pm \sqrt{M^2 - a^2\cos^2\theta}, \quad r_{\mathrm{eh},\pm} = M \pm \sqrt{M^2 - a^2}. \quad (29)$$

Equations (29) are derived from the conditions $g_{tt} = 0$ and $\Delta = 0$, respectively. $r_{\mathrm{s},+}$ is called "ergosurface" and the region "down" to $r_{\mathrm{eh},+}$ is the "ergoregion", where the spacetime is forced into corotation with the black hole (called "frame dragging"). Correspondingly, $r_{\mathrm{s},+}$ and $r_{\mathrm{eh},-}$ are the inner ergosurface and horizon. The physical singularity is no longer a single point but is extended to a ring in the equatorial plane. Further, the ISCO reads

$$r_{\mathrm{ISCO},\,\mathrm{p/r}} = M\left[3 + Z_2 \mp (3 - Z_1)(3 + Z_1 + 2Z_2)\right] \quad (30)$$

where

$$Z_1 = 1 + \sqrt[3]{1 - a^2}\left(\sqrt[3]{1 + a} + \sqrt[3]{1 - a}\right), \quad Z_2 = \sqrt{3a^2 + Z_1^2}, \quad (31)$$

14

and the $\mp$ sign in (30) corresponds to the index p/r indicating pro- and retrograde orbits.

Especially for numerical calculations it is essential to remove singularities whenever possible, i. e. when the singularity is non-physical and only a consequence of coordinate choice. Transformations removing the singularity at the horizon permit its penetration and numerical schemes are able to handle calculations in the direct vicinity of the black hole. It is then unnecessary to terminate e. g. integrations of geodesics before reaching the event horizon, thereby avoiding loss of information about physical processes. Introducing the transformations

$$dt' = dt + \frac{2Mr}{\Delta}\, dr, \quad d\phi' = d\phi + \frac{a}{\Delta}\, dr, \tag{32}$$

and their corresponding integral forms (see e. g. [56]), the metric (27) can be rewritten in Kerr-Schild coordinates (t', r, θ, ϕ') as

$$\begin{aligned}
ds^2 = {}&-(1 - B)\, dt'^2 - 2Ba \sin^2\theta\, dt'\, d\phi' + 2B\, dt'\, dr - 2a(1 + B)\sin^2\theta\, dr\, d\phi' \\
&+ (1 + B)\, dr^2 + \Sigma\, d\theta^2 + \frac{A \sin^2\theta}{\Sigma}\, d\phi'^2,
\end{aligned} \tag{33}$$

with $B = 2Mr/\Sigma$. This form of the Kerr metric only exhibits the physical singularity $\Sigma = 0$; note that its ring structure is not obvious in this coordinate choice [56].

McKinney and Gammie [57] introduced another modification to the line element (33) in order to control the grid resolution both near the event horizon and in the equatorial plane. Originally, the coordinate transformation read [57]

$$\tilde{r} = e^r, \quad \tilde{\theta} = \pi\theta + \frac{1 - h}{2}\sin(2\pi\theta). \tag{34}$$

where h is a parameter determining how fine the grid is near the equatorial plane. In the basic form (34), the expression for $\tilde{r}$ however lacks a control parameter, whereas $\tilde{\theta}$ can only be inverted numerically. Therefore, (34) are exchanged with

$$\tilde{r} = R_0 + e^r \tag{35}$$

$$\tilde{\theta} = \theta + \frac{2h\theta}{\pi^2}(\pi - 2\theta)(\pi - \theta) \tag{36}$$

where in $\tilde{r}$ a new parameter R_0 was introduced. The new expression for $\tilde{\theta}$ shows

sufficiently similar behavior compared to (34) but can be inverted analytically [21]. The configuration $R_0 = 0, h = 0$, leaving the azimuthal coordinate unchanged and modifying the Kerr-Schild coordinate system only in the radial direction, leads to the so-called "logarithmic Kerr-Schild coordinates" [21].

Employing these modified coordinates and subsequently spacing the grid non-uniformly is beneficial in numerical simulations for two reasons. Firstly, plasma dynamics near the horizon and accretion disk can be captured more precisely since resolution is now naturally concentrated there. Secondly, the computational cost is significantly reduced compared to a uniform grid that would require to be fine over the whole simulation domain, even though the increased resolution is only desired in a region surrounding the equatorial plane.

3.1.2   Black holes in alternative theories of gravity

Even though Einstein's general relativity has proven its validity numerous times in both weak (e. g. [58,59]) and strong field-regime [60] since it was first published, it has some inherent pathologies. For one, it cannot be brought together with quantum theory, and the existence of physical singularities in the real world is still debated. Seeking to tackle these issues, a large number of alternative theories, based on an equivalently large number of motivations, have been developed. For decades, models such as non-singular black holes [61–63], the so-called "Einstein-aether theory" [64] or connections of general relativity to string theory [65–68], as used in this work, have been investigated.[2] With an increasing number of such theories it became desirable to employ generalized frameworks into numerical codes [69–72], as further explained below.

Additionally, parallel to altering the underlying theory of gravity, observational evidence for black holes is regularly tested with models of so-called black hole "mimickers". Those include for example boson stars [73–75] and naked singularities [76]. This work focuses on a simplified class of solution to the Einstein-Maxwell-Dilaton-Axion gravity, the so-called "dilaton black hole".

---

[2]For additional sources, see for example [69].

3.1.3 Spinning black hole with Dilaton and Axion fields

From string theory, after dimensional reduction the action in Einstein-Maxwell-Dilaton-Axion gravity reads [65]

$$S_{\text{EMDA}} = \int d^4x \sqrt{-g} \left(R - 2\partial_\mu\varphi\,\partial^\mu\varphi - \frac{1}{2}e^{4\varphi}\partial_\mu\kappa\,\partial^\mu\kappa \right.$$
$$\left. - e^{-2\varphi}F_{\mu\nu}F^{\mu\nu} - \kappa F_{\mu\nu}{}^*F^{\mu\nu} \right), \tag{37}$$

adapting the notation of [77]. R is the Ricci scalar and $F_{\mu\nu}$, ${}^*F^{\mu\nu}$ are the electromagnetic tensor and its dual, respectively. The newly introduced dilaton and axion fields φ and κ couple to the electromagnetic tensor. Due to this coupling, in the case of a rotating dilaton black hole, nonzero magnetic field contributions emerge in the line element indirectly in the form of a number of free parameters used in the derivation of the line element from (37) [65]. Even though in this work the dilaton black hole is non-rotating, in future investigations this magnetic field contribution introduces an additional difference to the Kerr spacetime that potentially has a significant impact on the accretion flow. The line element, for one class of solutions, reads [65]

$$ds^2 = -\frac{\Delta - a^2\sin^2\theta}{\Sigma}\,dt^2 - \frac{2a\sin^2\theta\,(\Xi - \Delta)}{\Sigma}\,dt\,d\phi + \frac{\Sigma}{\Delta}\,dr^2$$
$$+ \Sigma\,d\theta^2 + \frac{\Xi^2 - \Delta\,a^2\sin^2\theta}{\Sigma}\sin^2\theta\,d\phi^2. \tag{38}$$

Compared to the Kerr spacetime, the functions Δ, Σ and Ξ contain now the "dilaton parameter" b, quantifying the deviation from general relativity and resembling a coupling strength between the dilaton field and the electromagnetic tensor:

$$\Sigma = r^2 + 2br + a^2\cos^2\theta, \tag{39}$$

$$\Delta = r^2 - 2Mr + a^2, \tag{40}$$

$$\Xi = r^2 + 2br + a^2. \tag{41}$$

The mass M consists of the dilaton parameter and the ADM mass M_{ADM} as $M_{\text{ADM}} = M + b$. Analogously to the Kerr spacetime, the horizon is described by

$$r_{\text{eh},\pm} = (M_{\text{ADM}} - b) \pm \sqrt{(M_{\text{ADM}} - b)^2 - a^2}. \tag{42}$$

3. MATHEMATICAL BACKGROUND

Impact of the dilaton field on the shadow size

A detailed comparison of black hole shadow sizes for Kerr- and dilaton spacetimes has been carried out in detail by Wei & Liu [77]. Moving to "celestial coordinates" α and β resembling apparent distances on the sky for an infinitely far away observer,

$$\alpha = \lim_{r \to \infty} \left(-r^2 \sin \theta_0 \frac{d\phi}{dr} \bigg|_{\theta \to \theta_0} \right) \equiv -\xi \csc \theta_0 \,, \tag{43}$$

$$\beta = \lim_{r \to \infty} \left(r^2 \frac{d\theta}{dr} \bigg|_{\theta \to \theta_0} \right) \equiv \pm \sqrt{\eta + a^2 \cos^2 \theta_0 - \xi^2 \cot^2 \theta_0} \,, \tag{44}$$

and setting $\theta_0 = \pi/2$ (equatorial observer),

$$\alpha = -\xi, \quad \beta = \pm \sqrt{\eta} \,. \tag{45}$$

Explicit expressions for ξ and η depend on the spacetime but maintain the form of (45). For the Kerr metric, they are derived in [78], while for the dilaton case they are given in [77] based on an analogous calculation.

The shadows are constructed by integrating a large number of geodesic equations for $-10 < \alpha < 10$ and $-10 < \beta < 10$, i.e. creating a full back-lit image and plotting only the outer edge of the shadow region. Observables are defined as the radius of a circular overlay for each a-b-configuration and the deviation of said overlay from the shadow edge.

Plots for a number of example configurations of a and b are shown in figure 2. The plots are centered on the black hole and the observer is placed in the equatorial plane. It is apparent that, while the overall size of the shadow decreases with larger values for b and fixed a, the deformation from a circular shape increases significantly. Moreover, according to Wei & Liu, from these observables the spin and dilaton parameter could be deduced from an image of the shadow taken with sufficient resolution.
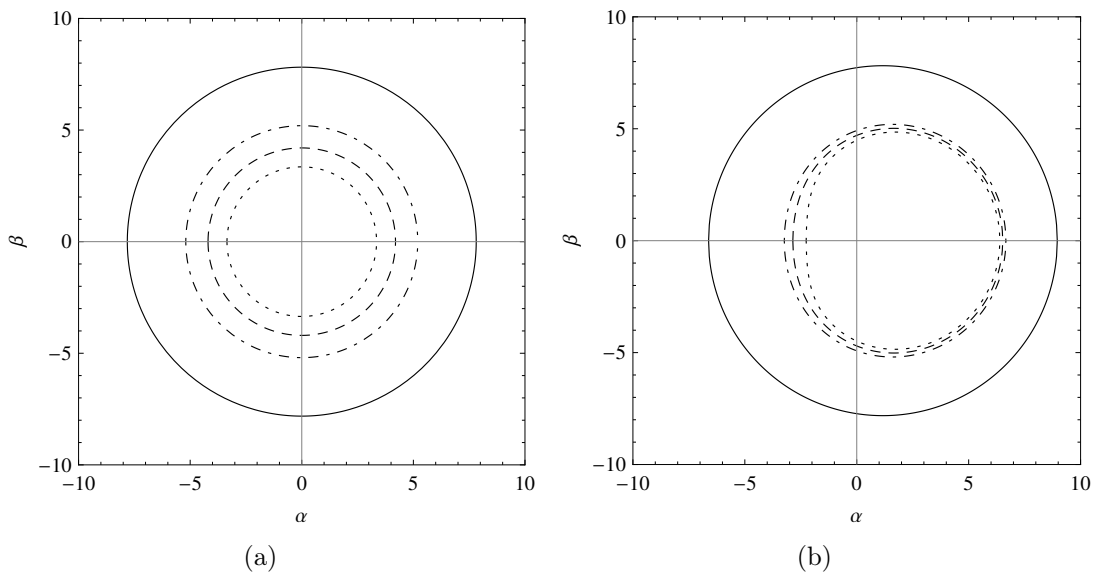
Figure 2: Shadow calculations taken from [77]. On the left, $a = 0$ and inner shadow edges for $b \in \{-2.0, 0.0, 0.5, 0.8\}$ from outside to inside. In the right panel, $a = 0.8$ and $b \in \{-2.0, 0.0, 0.1, 0.19\}$ where the line types have been assigned to fit the order on the left.

Vanishing spin and axion field

Since in this work only a non-rotating dilaton black hole is considered, along with a vanishing axion field, the EMDA metric (38) can be rewritten as [48]

$$ds^2 = -\left(\frac{r - 2M}{r + 2b}\right) dt^2 + \left(\frac{r + 2b}{r - 2M}\right) d\tilde{\rho}^2 + \tilde{\rho}^2 \, d\Omega^2, \qquad (46)$$

with a pseudo-radial coordinate $\tilde{\rho}^2 = r^2 + 2br$ and $M = M_{\text{ADM}} - b$ as defined above. This constrains the dilaton parameter as $0 < b < M_{\text{ADM}}$ [79].

For comparability, the dilaton and Kerr spacetimes have to be matched in a way such that the systems exhibit similar dynamical properties. This leaves as options the three characteristic radii: event horizon, photon orbit, and ISCO. The matching results in relations between the spin parameter a and the dilaton parameter b by equating said radii for both spacetimes. The spin is of course not physically dependent on the dilaton parameter, or vice versa. Once a matching is chosen, values for a and b for the rotating Kerr- and the non-rotating dilaton black hole simply correspond to each other in pairs. Derivations of the reported expressions (appendix (C)) can be found in the supplementary information to [48] and in [80] for Kerr and dilaton spacetimes, respectively.

3. MATHEMATICAL BACKGROUND

3.1.4 RZ parametrized implementation

Rezzolla, Zhidenko, and later Konoplya *et al.* [71, 72] developed generic parametrizations for spherically symmetric and axisymmetric spacetimes, respectively. These approximations are capable of reproducing the analytical forms of such metrics to high precision and are advantageous to employ in numerical codes since only a single model-independent framework needs to be implemented. Each new metric or spacetime can then be added in terms of the parametrization coefficients to the desired order. In Boyer-Lindquist coordinates, the Kerr metric can be exactly reproduced using the axisymmetric parametrization [71], whereas parametrizing the dilaton spacetime yields a small error of order 10^{-6} [48]. Even though in the GRRT code the analytically known dilaton metric could have been used, the implementations were chosen to be consistent with the GRMHD code. In the following, the spherically symmetric parametrization applied to the dilaton black hole will be quickly described. Any spherically symmetric metric can be written as [72]

$$ds^2 = -N(r)\,dt^2 + \frac{B(r)}{N(r)}\,dr^2 + r^2\,d\theta^2 + r^2\sin^2\theta\,d\phi^2, \tag{47}$$

where $N(r_{\rm eh}) = 0$. Introducing $x = 1 - r_{\rm eh}/r$, $\epsilon = 2M/r_{\rm eh} - 1$ and $N(x) = x\,A(x)$, the metric functions are expanded as

$$A(x) = 1 - \epsilon\,(1 - x) + (a_0 - \epsilon)(1 - x)^2 + \widetilde{A}(x)(1 - x)^3, \tag{48}$$

$$B(x) = 1 + b_0\,(1 - x) + \widetilde{B}(x)(1 - x)^2. \tag{49}$$

$\widetilde{A}(x)$ and $\widetilde{B}(x)$ are given in the form of Padé expansions up to order n:

$$\widetilde{A} \equiv \cfrac{a_1}{1 + \cfrac{a_2\,x}{1 + \cfrac{a_3\,x}{\cdots}}}, \quad \widetilde{B} \equiv \cfrac{b_1}{1 + \cfrac{b_2\,x}{1 + \cfrac{b_3\,x}{\cdots}}}. \tag{50}$$

In order to approximate the metric terms accurately, $n = 2$ is sufficient [48, 72]. In the special case of a dilaton spacetime, the coefficients up to second order are again given in [48] or [72] ($\psi \equiv b/2M$, $\omega \equiv \sqrt{1 + b/M}$) with $\epsilon = \omega - 1$:

$$a_0 = \psi\,, \qquad\qquad\qquad b_0 = 0\,, \tag{51}$$

$$a_1 = 2\,\omega + \frac{1}{1 + \psi} - 3 - \psi\,, \qquad b_1 = \frac{\omega}{1 + \psi} - 1\,, \tag{52}$$

$$a_2 = \frac{\omega - \psi}{1 + \psi} - \frac{1}{2\,(1 + \psi)^2}\,, \qquad b_2 = \frac{\omega}{1 + \psi} - 1 - \left(\frac{\psi}{1 + \psi}\right)^2. \tag{53}$$

3.2 The 3+1 split of spacetime

In complex systems, analytical solutions to equations are often hard or impossible to obtain, and numerical solutions are required to investigate physical processes. Even though space and time are equivalent in their role as coordinates, it is often convenient to detach the time-like part from the spatial part of the equations that need to be solved. Most numerical schemes were therefore developed to be applied to systems of equations with a space-time split structure. Equations are taken from [21], [56] and references therein. A more detailed derivation can be found in [56].

The spatial part of spacetime consists of hypersurfaces Σ_t along the time coordinate t, with a four-velocity n_μ normal to it, defining an Eulerian observer:

$$n_\mu \equiv -\alpha \nabla_\mu t\,, \tag{54}$$

where α is called "lapse function". The spatial projection operator γ^μ_ν defined by the four-dimensional metric $g_{\mu\nu}$ and the purely spatial metric $\gamma_{\mu\nu} = g_{\mu\nu} + n_\mu n_\nu$ reads

$$\gamma^\mu_\nu \equiv g^{\mu\rho}\gamma_{\rho\nu} = \delta^\mu_\nu + n^\mu n_\nu\,. \tag{55}$$

The last term can be identified with the time projection operator $N^\mu_\nu = -n^\mu n_\nu$. Note that while μ, ν still range from 0 to 3, the spatial projection operator is indeed purely spatial, with all timelike and mixed terms being equal to zero.

With these tensors, any four-vector can be split into its time– and space–like parts. Time evolution from one hypersurface to the next takes place along a basis vector $\boldsymbol{t}$:

$$\boldsymbol{t} \equiv \alpha \boldsymbol{n} + \boldsymbol{\beta}, \tag{56}$$

where α is again the lapse and $\boldsymbol{\beta}$ is called the "shift vector". From the expressions for the spatial metric, the time evolution vector and the components of $n_\mu = (-\alpha, 0, 0, 0)$ and $n^\mu = \frac{1}{\alpha}(1, -\beta^i)$, the line element of an arbitrary 3+1 decomposed metric can be constructed:

$$ds^2 = -\left(\alpha^2 - \beta_i \beta^i dt^2\right) + 2\beta_i dx^i dt + \gamma_{ij} dx^i dx^j \,, \tag{57}$$

where i, j are spatial indices and the metric components can be written as

$$g_{\mu\nu} = \begin{pmatrix} -\alpha^2 + \beta_i \beta^i & \beta_i \\ \beta_i & \gamma_{ij} \end{pmatrix}, \quad g^{\mu\nu} = \begin{pmatrix} -1/\alpha^2 & \beta^i/\alpha^2 \\ \beta^i/\alpha^2 & \gamma^{ij} - \beta^i \beta^j/\alpha^2 \end{pmatrix}. \tag{58}$$

Both the Kerr metric in different coordinate systems (27, 33) and the dilaton metric (46) have been used in the $3 + 1$ decomposed form in the GRMHD simulations in accordance to the formulation of fluid quantities and equations.

3.3 GRMHD equations

Plasma accretion dynamics in black hole systems are governed by the equations of GRMHD describing local conservation of mass, energy and momentum along with Faraday's law:

$$\nabla_\mu \left(\rho u^\mu\right) = 0, \quad \nabla_\mu T^{\mu\nu} = 0, \quad \nabla_\mu {}^*F^{\mu\nu} = 0, \tag{59}$$

with rest mass density ρ, fluid four-velocity u^μ, energy-momentum tensor $T^{\mu\nu}$ and the dual of the Faraday tensor ${}^*F^{\mu\nu}$:

$$T^{\mu\nu} = \rho h_{\text{tot}} u^\mu u^\nu + p_{\text{tot}} g^{\mu\nu} - b^\mu b^\nu, \quad {}^*F^{\mu\nu} = b^\mu u^\nu - b^\nu u^\mu \tag{60}$$

with total pressure $p_{\text{tot}} = p + b^2/2$, total specific enthalpy $h_{\text{tot}} = h + b^2/\rho$, magnetic field strength in the fluid frame $b^2 = b^\mu b_\mu$ and magnetic field four-vector b^μ.

As explained above, the majority of numerical schemes available in the literature for solving complex systems such as hyperbolic partial differential equations is built for time-space decomposed systems. Applying the spatial projection operator (55) to (59), the GRMHD equations can be recast into a $3 + 1$ split and conservative formulation [21], ensuring convergence to the correct solution even if shocks are present [56]. The conservative form of (59) reads [21]:

$$\partial_t \left(\sqrt{\gamma}\boldsymbol{U}\right) + \partial_i \left(\sqrt{\gamma}\boldsymbol{F}^i\right) = \sqrt{\gamma}\boldsymbol{S}, \tag{61}$$

with conserved variables $\boldsymbol{U}$ and numerical fluxes $\boldsymbol{F}^i$

$$\boldsymbol{U} = \begin{bmatrix} D \\ S_j \\ \tau \\ B_j \end{bmatrix}, \quad \boldsymbol{F}^i = \begin{bmatrix} \mathcal{V}^i D \\ \alpha W_j^i - \beta^i S_j \\ \alpha \left(S^i - v^i D \right) - \beta^i \tau \\ \mathcal{V}^i B^j - B^i \mathcal{V}^j \end{bmatrix}, \tag{62}$$

and source terms [21]:

$$\boldsymbol{S} = \begin{bmatrix} 0 \\ \frac{1}{2} \alpha W^{ik} \partial_j \gamma_{ik} + S_i \partial_j \beta^i - U \partial_j \alpha \\ \frac{1}{2} W^{ik} \beta^j \partial_j \gamma_{ik} + W_i^j \partial_j \beta^i - S^j \partial_j \alpha \\ 0 \end{bmatrix}. \tag{63}$$

These building blocks of the GRMHD equations consist of transport velocity $\mathcal{V}^i$, Eulerian density D, rescaled energy density τ, conserved Eulerian total energy density U, spatial stress-energy tensor W^{ij}, and covariant three-momentum S^i:

$$\mathcal{V}^i \equiv \alpha v^i - \beta^i \tag{64}$$

$$D \equiv -\rho u^\nu n_\nu \tag{65}$$

$$\tau \equiv U - D \tag{66}$$

$$U \equiv T^{\mu\nu} n_\mu n_\nu = \rho h \Gamma^2 - p + \frac{1}{2} \left[B^2 \left(1 + v^2 \right) - \left(B^j v_j \right)^2 \right], \tag{67}$$

$$W^{ij} \equiv \gamma_\mu^i \gamma_\nu^j T^{\mu\nu} = S^i v^j + p_{\text{tot}} \gamma^{ij} - \frac{B^i B^j}{\Gamma^2} - \left(B^k v_k \right) v^i B^j, \tag{68}$$

$$S_i \equiv \gamma_i^\mu n^\alpha T_{\alpha\mu} = \rho h \Gamma^2 v_i + B^2 v_i - \left(B^k v_k \right) B_i. \tag{69}$$

B^i are the magnetic field three-vectors in the Eulerian frame, Γ is the Lorentz factor and v^i is the three-velocity.

4 Photon dynamics in curved spacetimes

4.1 Emission models

There are two emission-related novelties employed in this work coming from the pioneering release in 2018 by Mizuno *et al.* Firstly, the electron temperature is now governed by a parametrization dependent on plasma β and some hyper-parameters. Secondly, together with the well-established thermal electron distribution, non-thermal emission is included.

Electron temperature

In a majority of cases, in GRMHD codes only ions (protons) are simulated due to their dynamical importance. Since the bulk of radiation comes from electrons, a bridge between protons and electrons, or rather their temperatures, has to be established. In past works such as Mizuno *et al.* 2018, the electron– to proton temperature ratio has often been assumed to be a constant. In this work, it is instead parametrized with two parameters R_{high} and R_{low} while also depending on the ratio of gas and magnetic pressure $\beta \equiv p_{\text{gas}}/p_{\text{mag}}$. This $T_{\text{p}}/T_{\text{e}} = R(\beta)$ parametrization is defined as [81,82]

$$\frac{T_{\text{p}}}{T_{\text{e}}} = R(\beta) = \frac{R_{\text{high}}\,\beta^2 + R_{\text{low}}}{1 + \beta^2} \,. \tag{70}$$

R_{high} controls the temperature ratio in the accretion disk, where $\beta \gg 1$; R_{low} accordingly controls the temperature ratio in the jet, i.e. the magnetized region where $\beta \ll 1$. Aside from a test case defined by $T_{\text{p}}/T_{\text{e}} = 3$ used only to reproduce Mizuno *et al.* 2018, equation (70) is used in the simplified form [38,83]

$$\frac{T_{\text{p}}}{T_{\text{e}}} = \frac{R_{\text{high}}\,\beta^2 + 1}{1 + \beta^2} \,, \tag{71}$$

where $R_{\text{low}} = 1$. The electron temperature is then calculated as

$$T_{\text{e}} = \frac{m_{\text{e}}c^2}{k_{\text{B}}}\,\Theta_{\text{e}} = \frac{m_{\text{e}}c^2}{k_{\text{B}}}\,\Theta_{\text{p}}\,\frac{m_{\text{p}}}{m_{\text{e}}}\,\left(\frac{T_{\text{p}}}{T_{\text{e}}}\right)^{-1} \,. \tag{72}$$

$\Theta_{\text{e}} \equiv k_{\text{B}}T/m_{\text{e}}c^2$ is the dimensionless electron temperature; its proton (ion) equivalent Θ_{p} is known from the GRMHD simulation.

For R_{high}, three representative values are chosen. The goal was to study a torus–

and a jet-dominated configuration along with preferably one in between, it was however unknown where along the range of $R_{\rm high}$ this shift happened. $R_{\rm high} = 10$ turned out to be the clearly torus-dominated configuration, whereas $R_{\rm high} = 80$ is already purely jet-dominated. Exploring the range $10 < R_{\rm high} < 80$ will be part of a future work.

Synchrotron emission

The sole radiative process considered this work is synchrotron emission, sometimes called magnetobremsstrahlung. In future studies, bremsstrahlung (free-free emission) and in verse Compton scattering will be included. Synchrotron radiation is the ultrarelativistic limit to "cyclotron radiation", emitted by charged particles forced into helical motion in a magnetic field [84]. The frequency of this gyration is equal to the frequency of emitted cyclotron radiation, whereas for synchrotron emission the emitted frequencies can far exceed that of gyration.

Due to relativistic beaming effects, synchrotron radiation is emitted in a conical shape of angular width $2/\gamma_{\rm e}$, where $\gamma_{\rm e}$ is the Lorentz factor of the electrons. The emission cone is centered on the direction of particle velocity and its half angle is equal to the pitch angle between the field and velocity direction. The power received has to be corrected for the Doppler beaming during the particle's movement towards the observer. [84].

Upon interaction with a charge, an emitted photon may be absorbed, raising the energy state of the charged particle. This is called "self-absorption". The total intensity depends on both emissivity and absorptivity. These appear in the radiative transfer equations in the form of their respective coefficients that can be constructed by the emitted power and the electron energy distribution function [84]. Distribution functions and their respective emissivities and absorptivities are shown below.

At low frequencies, in the optically thick regime, the source function dominates the intensity expression (explained in section 4.2). Moving to higher frequencies, a turning point or cutoff in the spectrum is caused by the emission function taking over [84].

Electron energy distribution function

Matter in thermodynamic equilibrium emits radiation dependent on its temperature T and internal properties. In the limit of optically thick media, thermal emission becomes blackbody radiation. In an ideal gas in equilibrium, the electron number density is described by the Maxwell-Boltzmann distribution function, in the following referred to as "thermal energy distribution function (eDF)". For relativistic but still ideal gases, special relativistic effects have to be taken into account and the Maxwell-Boltzmann distribution turns into the Maxwell-Jüttner distribution. It reads [43, 85]

$$\frac{dn_{\mathrm{e}}}{d\gamma_{\mathrm{e}}\, d\cos\xi\, d\phi} = \frac{n_{\mathrm{e}}}{4\pi\Theta_{\mathrm{e}}} \frac{\gamma_{\mathrm{e}}\left(\gamma_{\mathrm{e}}^2 - 1\right)^{1/2}}{K_2\left(1/\Theta_{\mathrm{e}}\right)} \exp\left(-\frac{\gamma_{\mathrm{e}}}{\Theta_{\mathrm{e}}}\right), \tag{73}$$

with gyrophase ϕ, Lorentz factor of the electrons γ_{e}, pitch angle ξ and modified Bessel function of the second kind K_2. K_2 is evaluated numerically, and thus implemented into BHOSS as a table.

Many space plasmas have been found to show non-thermal electron energy distributions. In 1968, Vasyliunas first constructed a distribution function consisting of a thermal core for low energies and a power-law tail to fit the high energy bins in his data [86]. Two decades later, Tsallis developed non-extensive thermodynamics by deforming the entropy with a parameter q that could reproduce the equilibrium limit for $q \to 1$ [87]. Proceeding with the well-known canonical calculations readily yielded a kappa distribution. In 1998, Tsallis once again refined his theory with modified descriptions of thermodynamic expectation values [88]. Apart from reproducing Vasyliunas' empirically constructed kappa distribution, the theory of non-extensive thermodynamics most importantly shows temperature to be well-defined even out of equilibrium, in the form of the purely kinetic temperature. A full description of non-extensive thermodynamics can be found in appendix D and [89]. The kappa eDF can be rewritten to the same set of "coordinates" $(\phi, \gamma_{\mathrm{e}}, \xi)$ used in the thermal distribution above [85, 90]:

$$\frac{dn_{\mathrm{e}}}{d\gamma_{\mathrm{e}}\, d\cos\xi\, d\phi} = \frac{N}{4\pi}\gamma_{\mathrm{e}}\left(\gamma_{\mathrm{e}}^2 - 1\right)^{1/2}\left(1 + \frac{\gamma_{\mathrm{e}} - 1}{\kappa w}\right)^{-(\kappa+1)}, \tag{74}$$

where the normalization factor N is again usually evaluated numerically, as its analytical form is complex [85]. In the ultra-relativistic limit $\kappa w \gg 1$, $N =$

$n_e(\kappa - 2)(\kappa - 1)/(2\kappa^2 w^3)$ [85]. Figure (3) shows a thermal–, power-law and two representative kappa distribution functions in this limit. In this work, κ is not set to a constant value (e. g. [91]) but is calculated from the fluid variables [92] (see also [82]). κ is set by the power law index for high energies $\widetilde{p} = \kappa - 1$ (the tilde is to distinguish p from the pressure):

$$\widetilde{p} = A_{\widetilde{p}} + B_{\widetilde{p}} \tanh\left(C_{\widetilde{p}}\beta\right), \tag{75}$$

$$A_{\widetilde{p}} = 1.8 + 0.7\sigma^{0.5}, \tag{76}$$

$$B_{\widetilde{p}} = 3.7\sigma^{-0.19}, \tag{77}$$

$$C_{\widetilde{p}} = 23.4\sigma^{0.26}. \tag{78}$$

Ball *et al.* obtain these fits by developing eDFs in sub-grid particle-in-cell simulations of a two-dimensional magnetic reconnection layer for different β and σ and fitting them to analytical eDF models [92]. These fits are viable for $10^{-4} < \beta < 1.5$ and $0.1 < \sigma < 7.2$, consistent with typical values found in the outer jet wall. The "width" of the distribution w can be rewritten to contain a thermal and a magnetic energy term [82]:

$$w = \frac{\kappa - 3}{\kappa}\left(\Theta_{\mathrm{e}} + \tilde{\epsilon}\frac{m_{\mathrm{p}}}{m_{\mathrm{e}}}\frac{\sigma}{6}\right), \tag{79}$$

where

$$\tilde{\epsilon} = \frac{\epsilon}{2}\left(1 + \tanh\left(r - r_{\mathrm{inj}}\right)\right). \tag{80}$$

$\tilde{\epsilon}$ sets the weight of the magnetic energy contribution to the electron temperature. ϵ is not to be confused with the specific internal energy; it is a measure for the amount of electrons injected past the radius r_{inj}, depending on the magnetic energy [82]. For $r \gg r_{\mathrm{inj}}$, $\tilde{\epsilon} \to \epsilon$. The second term in equation (79) acts as a magnetization-dependent dimensionless temperature. Directly adapting from Davelaar *et al.* 2019, ϵ is set to be quasi-boolean as $\epsilon \in \{0, 0.015\}$, "switching on" the magnetic contribution to the distribution for $\epsilon \neq 0$.
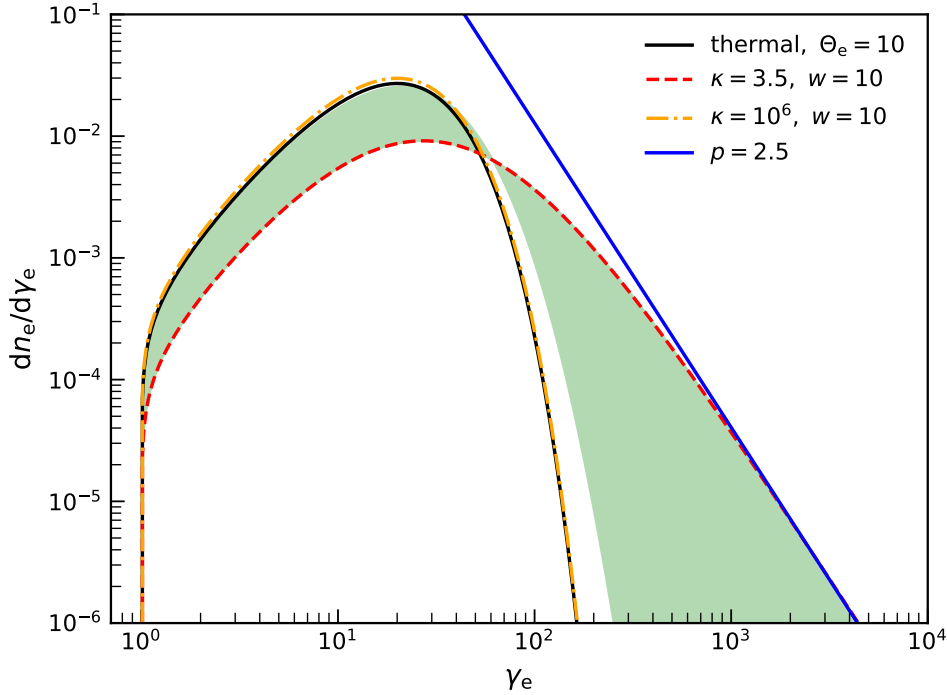
Figure 3: Example electron distribution functions. n_e: electron number density, γ_e: electron Lorentz factor, Θ_e: dimensionless electron temperature. Black: thermal blackbody spectrum (Maxwell-Jüttner distribution). Blue: power law distribution with index 2.5. Red/Yellow: kappa distributions with the same w but different values for κ. The green shaded region is formed by $\kappa \in [3.5, 20]$, believed to be found in astrophysical jets.

Emissivities and absorptivities

All distribution functions take part in the radiative transfer calculations in the form of their respective emission and absorption coefficients. For thermal emission, Leung *et al.* provide an approximate expression [43]:

$$j_{\nu,\,\text{thermal}} = n_e \frac{\sqrt{2}\pi e^2 \nu_s}{3 K_2 \left(1/\Theta_e\right) c} \left(X^{1/2} + 2^{11/12} X^{1/6}\right)^2 \exp\left(-X^{1/3}\right), \qquad (81)$$

where, with the electron cyclotron frequency ν_c,

$$X \equiv \frac{\nu}{\nu_s} = \frac{\nu}{(2/9)\nu_c \Theta_e^2 \sin\theta}\,.$$

The absorptivity is given as the emissivity divided by the Planck function, as required by Kirchhoff's law of thermal radiation [43]. The kappa model coefficients are given as approximate expressions taken from [85]. Since in this work polarization is neglected, only one component of the Stokes basis is of importance. Both coefficients are approximated by low and high frequency limits connected by a

bridging function. The dimensionless emissivity limits for $3 \leq \kappa \leq 7$ read

$$J_{S,lo} = X_\kappa^{1/3} \sin(\theta) \frac{4\pi \, \Gamma(\kappa - 4/3)}{3^{7/3} \, \Gamma(\kappa - 2)} \,, \tag{82}$$

$$J_{S,hi} = X_\kappa^{-(\kappa-2)/2} \sin(\theta) \, 3^{(\kappa-1)/2} \frac{(\kappa-2)(\kappa-1)}{4} \Gamma\left(\frac{\kappa}{4} - \frac{1}{3}\right) \Gamma\left(\frac{\kappa}{4} + \frac{4}{3}\right) , \tag{83}$$

where $X_\kappa \equiv \nu/\nu_\kappa \equiv \nu/(\nu_c (w\kappa)^2 \sin\theta)$ and, with $x = 3\,\kappa^{-3/2}$,

$$j_{\nu,\,\text{non-thermal}} = \frac{n_e e^2 \nu_c}{c} J_S = \frac{n_e e^2 \nu_c}{c} \left(J_{S,lo}^{-x} + J_{S,hi}^{-x}\right)^{-1/x}. \tag{84}$$

For the dimensionless absorptivity limits,

$$\begin{aligned}
A_{S,lo} &= X_\kappa^{-2/3} \, 3^{1/6} \frac{10}{41} \frac{2\pi}{(w\kappa)^{10/3-\kappa}} \frac{(\kappa-2)(\kappa-1)\kappa}{3\kappa-1} \Gamma\left(\frac{5}{3}\right)_2 \\
&\quad \times F_1\left(\kappa - \frac{1}{3}, \kappa+1, \kappa+\frac{2}{3}, -\kappa w\right) ,
\end{aligned} \tag{85}$$

$$A_{S,hi} = X_\kappa^{-(1+\kappa)/2} \frac{\pi^{3/2}}{3} \frac{(\kappa-2)(\kappa-1)\kappa}{(w\kappa)^3} \left(\frac{2\,\Gamma(2+\kappa/2)}{2+\kappa} - 1\right) \left(\left(\frac{3}{\kappa}\right)^{19/4} + \frac{3}{5}\right). \tag{86}$$

The bridging function is of the same form as above, however $x = \left(-\frac{7}{4} + \frac{8}{5}\kappa\right)^{-43/50}$:

$$\alpha_{\nu,\,\text{non-thermal}} = \frac{n_e e^2}{\nu m_e c} A_S = \frac{n_e e^2}{\nu m_e c} \left(A_{S,lo}^{-x} + A_{S,hi}^{-x}\right)^{-1/x}. \tag{87}$$

For illustration, $j_{\nu,\,\text{thermal}}$ and $j_{\nu,\,\text{non-thermal}}$ are shown together with their blackbody counterpart in figure 4.

4.2 Ray tracing and radiative transfer

The process of radiative post processing consists of two main parts: numerical evaluation of the geodesic equations to determine the path of each light ray, and calculating the intensity from emissivities and absorptivities along the path. There have been numerous advances to implement both aspects into a numerical code for the Kerr spacetime exclusively (e.g. [93–97]); [98] contains a short overview for a parametrization scheme in order for the code (5.2) to be able to operate in arbitrary axisymmetric spacetimes, based on [71].
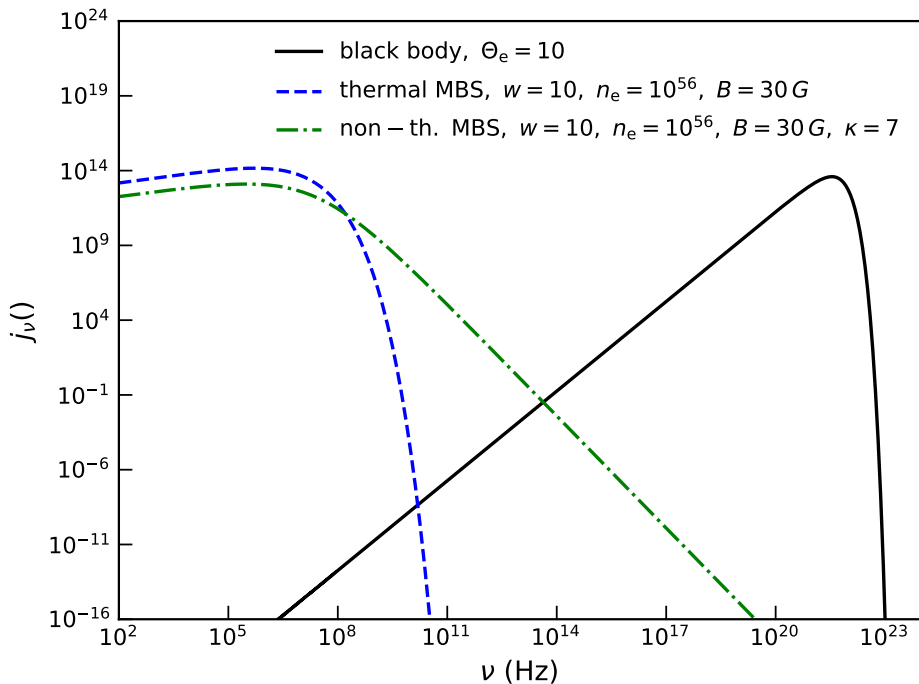
Figure 4: Example emission coefficients j_ν. n_e: electron number density, B: magnetic field strength. Black: black body. Blue: thermal magneto-bremsstrahlung (MBS) emission coefficient. Green: non-thermal MBS with $\kappa = 7$. The MBS curves are for emission angle $\theta = \pi/2$.

Geodesic motion in curved spacetime

Light rays move along so-called null geodesics. In this work, these geodesics are integrated directly ([11] and refs. therein). The geodesic equations are given in the form

$$\ddot{x}^\mu + \Gamma^\mu_{\sigma\rho}\dot{x}^\sigma\dot{x}^\rho = 0 \,, \tag{88}$$

where $\dot{x} \equiv \partial_\lambda x$ with affine parameter λ. It can be easily derived from the expression for parallel transport, in particular for a curve transporting its tangent [56], making use of the covariant derivative. Such a curve has the unique property of resembling a "straight" line in an arbitrary spacetime, i.e. the shortest connection between to points.

For parametrized spacetimes, the geodesics (88) potentially need to be reformulated in order to not include Christoffel symbols $\Gamma^\mu_{\sigma\rho}$ since the parametrized components increase greatly in complexity and length, hindering implementation significantly [98]. As shown in previous sections, the metrics used in this work are however either of a simple enough structure to use the analytic expressions or they are implemented in a simple spherically symmetric parametrization [72] (see 3.1.4), therefore (88) is readily used.

Radiative transfer equations

As mentioned above, the radiation emitted depends both on the total emission and on the parts that are self-absorbed. The radiative transfer equation, rewritten using the optical depth τ_ν reads

$$\frac{dI_\nu}{d\tau_\nu} = -I_\nu + \frac{j_\nu}{\alpha_\nu} \,, \tag{89}$$

for an intensity I_ν, absorption coefficient α_ν and emission coefficient j_ν at frequency ν. The solution at position s can be obtained by direct integration [11]:

$$I_\nu(s) = I_\nu(s_0)\, e^{-\tau_\nu} + \int_{s_0}^{s} j_\nu(s')\, e^{-(\tau_\nu(s) - \tau_\nu(s'))} ds' \tag{90}$$

$$= I_\nu(0)\, e^{-\tau_\nu} + \int_0^{\tau_\nu} S_\nu(\tau_\nu')\, e^{-(\tau_\nu - \tau_\nu')} d\tau_\nu' \,, \tag{91}$$

where in the second equality the source term $S_\nu \equiv j_\nu/\alpha_\nu$ was introduced. Since equation (89) is not Lorentz invariant, it is necessary to make use of conservation of phase space volume [99] and particle number to derive a covariant formulation for radiative transfer [11]. First, the Lorentz invariant intensity is defined as

$$\mathcal{I} \equiv \frac{I_\nu}{\nu^3} = \frac{I_E}{E^3} \,, \tag{92}$$

where [84]

$$I_E = \frac{E\, dN}{dA\, dt\, dE\, d\Omega} \,, \tag{93}$$

is the specific intensity of a light ray, i. e. a bundle of collimated photons. Recalling that $c = 1$, $dA\, dt$ and $E^2\, dE\, d\Omega$ are volume elements in space and momentum space for relativistic particles. dN is the particle number element and E the energy of the ray. Along with (92), it is convenient to define

$$\chi = \nu\alpha_\nu \,, \quad \eta = j_\nu/\nu^2 \,, \tag{94}$$

as corresponding invariant coefficients with $(\chi, \eta) = (\chi_0, \eta_0)$, "0" referring to measurement in the rest frame [11]. Equation (89) in covariant form therefore reads

$$\frac{d\mathcal{I}}{d\tau_\nu} = -\mathcal{I} + \frac{\eta}{\chi} \,. \tag{95}$$

Making use of $d\tau_\nu = \alpha_\nu ds$ and differentiating the solution of (95), $\mathcal{I}(\lambda)$, with

31

respect to λ, the radiative transfer equation can be cast into a set of differential equations [11]:

$$\frac{d\tau_\nu}{d\lambda} = \xi^{-1}\,\alpha_{0,\nu}\,, \tag{96}$$

$$\frac{d\mathcal{I}}{d\lambda} = \xi^{-1}\left(\frac{j_{0,\nu}}{\nu^3}\right)e^{-\tau_\nu}\,, \tag{97}$$

where ξ is the redshift factor. This formulation is particularly convenient for numerical evaluation of the intensity along a previously computed path of a light ray.

5 Numerical background

5.1 The BHAC code

All GRMHD simulations used in this work have been carried out with the black hole accretion code (BHAC) by O. Porth *et al.* [21]. It is a multidimensional extension module for the MPI-AMRVAC framework [100, 101]. BHAC is able to evolve the GRMHD equations in arbitrary spacetimes and coordinates in a finite volume representation. For a comparison against other available GRMHD codes, see [102].

5.1.1 Time advance

As explained in chapter 3.3 and above, the GRMHD equations in conservative form (59) are implemented in a finite-volume formulation. It consists of not only volume cell averaged source terms $\bar{\boldsymbol{S}}$ and conserved variables $\bar{\boldsymbol{U}}$, but also cell interface-averaged numerical fluxes $\bar{\boldsymbol{F}}^i$. The latter need a more extensive treatment at each time step since they first have to be individually calculated from the cell-averaged quantities. Additionally, knowledge of the primitive variables $\boldsymbol{P}(\boldsymbol{U})$ is required to calculate $\bar{\boldsymbol{S}}$ and $\bar{\boldsymbol{F}}^i$:

$$\boldsymbol{P}(\boldsymbol{U}) = \left[\rho, \Gamma v^i, p, B^i\right].$$ (98)

The cell-averaged primitive variables $\bar{\boldsymbol{P}}(\boldsymbol{U})$ first need to be recovered from the conserved variables. While $\boldsymbol{U}(\boldsymbol{P})$ is a straightforward transformation, $\boldsymbol{P}(\boldsymbol{U})$ is not. For this reason, auxiliary variables $\boldsymbol{A} = [\Gamma, \Gamma^2 \rho h] \equiv [\Gamma, \xi]$ are saved along with $\boldsymbol{U}$. Using equations (67) and (69), an expression can be obtained which ξ is the root of. From ξ and the equation of state (EOS), the other primitive variables can be calculated. In terms of the parameter ξ, the ideal gas EOS reads [21]

$$p = \frac{\hat{\gamma}}{\hat{\gamma} - 1} \left(\frac{\xi}{\Gamma^2} - \rho\right)$$ (99)

where $\hat{\gamma}$ is the adiabatic index.

Second, using a piecewise parabolic method (PPM), the left and right interface values of the primitive variables are calculated by fitting a parabola inside each grid cell [56]. $\boldsymbol{P}^L$ and $\boldsymbol{P}^R$ are then converted back to their conserved forms, arriving at states $\boldsymbol{U}^L$ and $\boldsymbol{U}^R$. Third, the approximate Riemann solver calculates the numerical fluxes at the cell interfaces. In this work, the total variation diminishing

Lax-Friedrichs theme (TVDLF) is used [21]. Once all intermediate quantities are calculated, the time advance of the evolution equation is carried out by a two-step predictor-corrector scheme.

5.1.2 Simulation setup

The setup of the accretion tori around the Kerr- and dilaton black holes follows [103]. Both tori are initially stationary, filling their entire Roche lobe such that the potential at the inner edge is the cusp potential. In the case of a constant angular momentum distribution, the torus is sub-Keplerian [104] and the expression for the equipotential surfaces simplifies to $W(r, \theta) = \ln |u_t|$. The time component of the fluid four-velocity u_t is derived as [104, 105]

$$-u_t = \sqrt{\frac{g_{t\phi}^2 - g_{tt}g_{\phi\phi}}{g_{tt}l^2 + 2g_{t\phi}l + g_{\phi\phi}}} \tag{100}$$

from $u_\mu u_\sigma g^{\mu\sigma} = -1$, defining the specific angular momentum $l = -u_\phi/u_t$ and angular velocity $\Omega = u^\phi/u^t$. Once the outermost closed equipotential surface $W(r_{\text{in}}) = W(r_{\text{out}})$ is determined, everywhere within that surface thermodynamic quantities are computed with an ideal gas EOS ($\hat{\gamma} = 4/3$) [21].

$$p = \varepsilon\rho(\hat{\gamma} - 1) \longrightarrow h(\rho, p) = 1 + \frac{\hat{\gamma}}{\hat{\gamma} - 1}\frac{p}{\rho} \tag{101}$$

Where ε is the specific energy density. For both tori, the inner radius is set to be $r_{\text{in}} = 10.3\,\text{M}$, coinciding with the cusp, whereas the specific angular momenta are chosen to be $l_{\text{Kerr}} = 4.5$ and $l_{\text{Dilaton}} = 4.567$.

Table 3 lists all parameters of the grid and simulation setup. Floor values are straightforwardly applied, mimicking an "atmosphere" whenever a cell satisfies $\rho \leq \rho_{\text{fl}} = 10^{-4}r^{-3/2}$ or $p \leq p_{\text{fl}} = (10^{-6}/3)\,r^{-5/2}$ in order to avoid vacuum regions outside the initial torus. Employed boundary conditions are those for standard in– and outflow in the radial direction, periodic in the azimuthal direction and a reflective wall for the polar boundaries [48]. The magnetic field is put onto the equilibrium torus artificially (the torus construction is therefore not strictly self-consistent), and the only non-zero vector potential component reads

$$A_\phi \propto \max(q, 0), \tag{102}$$

adiabatic index	$\Gamma = 4/3$
density floor	$\rho_{\mathrm{fl}} = 10^{-4} r^{-3/2}$
gas pressure floor	$p_{\mathrm{fl}} = (10^{-6}/3)\, r^{-5/2}$
radial grid extent	$r \in (0.8\, r_{\mathrm{eh}}, 1{,}000\,\mathrm{M})$
azimuthal extent	$\theta \in (0.01\pi, 0.99\pi)$
polar extent	$\phi \in (0, 2\pi)$
(N_r, N_θ, N_ϕ)	$(256, 128, 128)$
a	0.6
b	0.504
l_{Kerr}	4.5
l_{Dilaton}	4.567

Table 3: Simulation parameters by [48].

where for a standard and normal accretion (SANE) scenario [48, 106]

$$q = \frac{\rho}{\rho_{\max}} - 0.2\,. \tag{103}$$

In a SANE system, the magnetic fields constantly allow matter to accrete onto the black hole since the fields are weak and disordered [107]. Strong poloidal magnetic fields can however also lead to magnetic flux piling up near the black hole and blocking off accretion, thereby "arresting" the disk and leading to a magnetically arrested disk (MAD) scenario [107]. Then [106],

$$q = \frac{\rho}{\rho_{\max}} \left(\frac{r}{r_{\mathrm{in}}}\right)^3 \sin^3\theta \exp\left(-\frac{r}{400}\right) - 0.2\,. \tag{104}$$

In this work, only the SANE model is employed, in accordance with Mizuno *et al.* 2018 [48]. Once the torus is constructed in hydrostatic equilibrium, the poloidal field is put on top. Since the system is stable at this stage, the magnetorotational instability is triggered by a 1% random perturbation in the gas pressure to start the accretion process.

5.2 The BHOSS code

This work makes use of the BHOSS code ("black hole observations in stationary spacetimes", Younsi *et al.* 2020, in prep.). It is an OpenMP parallelized GRRT code written in Fortran 95/2003 solving both the geodesic equations and the intensity ODEs (96), (97) in 3 D.

For the geodesics, a Runge-Kutta-Fehlberg integrator is implemented to solve the equations to fourth order and be able to adjust the step size based on a fifth

Number of pixels	1024×1024
Width/r_g	40×40
Width/µas	211×211
Inclination/deg.	60
$T_\mathrm{p}/T_\mathrm{e}$	3
D_BH/kpc	8.175 (7.86)
$M_\mathrm{BH}/10^6\,\mathrm{M}_\odot$	4.148 (4.02)
Black hole spin a	0.6
Target flux/Jy	3.0 (3.4)

Table 4: Image parameters for the BHOSS code. In brackets: parameters from [48] for reproduction.

order error estimate [108]. The choice of coordinate system is arbitrary; if it is different to the GRMHD simulation system, data is linearly interpolated. The transformations are handled automatically. Along each ray, the intensity differential equations (97) and (96) are integrated in a simple Eulerian scheme.

The observer is located at $(r_\mathrm{obs}, \theta_\mathrm{obs}, \phi_\mathrm{obs})$ and far away from the black hole, in the form of an image plane (x, y). The z direction is aligned with the radial coordinate of the black hole system. Therefore, the initial light ray positions have to be transformed from Cartesian to Boyer-Lindquist coordinates before integrating the geodesics. The pixel positions then read

$$r^2 = \sigma + \sqrt{\sigma^2 + a^2 Z^2}\,, \tag{105}$$

$$\cos\theta = Z/r\,, \tag{106}$$

$$\tan\phi = Y/X\,, \tag{107}$$

where explicit expressions for X, Y, Z and σ are given in [98] and are reported in appendix B. Derivatives of these equations yield the three-velocity of each ray, with the t-component of the four-vector given by the invariance of the line element. All rays start at $t = 0$ from the observer's position (in this case, earth).

The intensity along each light ray is calculated with a simple Eulerian scheme using equations (96) and (97). Various absorption and emission coefficients are implemented in a modular way for the code to be easily expandable and modifiable. In order to be properly able to reproduce Mizuno *et al.* 2018, initial conditions were first adapted from [48]. Afterwards, D_BH and M_BH were updated with new results obtained by the GRAVITY collaboration [25].

6 Results

6.1 GRMHD simulations

All GRRT calculations and synthetic imaging are carried out on the SANE simulation used in M18. The initial conditions are an equilibrium torus with a weak poloidal magnetic field. Since this system is stable by construction, the accretion process is triggered by perturbing the gas pressure to develop a magneto-rotational instability. Figure 5 shows mass accretion rate $\dot{M}$ and magnetic flux ϕ_B measured at the event horizon. They are calculated as [102]:

$$\dot{M} \equiv \int_0^{2\pi} d\varphi \int_0^\pi d\theta \ \sqrt{-g} \ \rho u^r, \qquad (108)$$

$$\phi_B \equiv \int_0^{2\pi} d\varphi \int_0^\pi d\theta \ \sqrt{-g} \ \frac{1}{2} \left| B^r \right|, \qquad (109)$$

with, determinant of the metric g, density ρ, radial four-velocity component u^r and radial magnetic field component B^r.

After large initial accretion rates due to the instability in the torus, both the Kerr and the dilaton black hole systems reach a quasi-steady state after $\sim 10\,000$. Both the analysis of GRMHD quantities plasma β, density ρ and magnetization σ and the GRRT imaging takes place time-averaged from $11\,000\,\mathrm{M}$ to $12\,000\,\mathrm{M}$, with snapshots every $10\,\mathrm{M}$, in total corresponding to roughly six hours for the mass of Sgr A* [48]. The region is marked as a black rectangle in figure 5.

While the mass accretion rates exhibit similar behavior, the magnetic flux at the horizon doubles in the Kerr system. The difference in magnetic flux after $\sim 30\,\mathrm{h}$ ($\sim 6,000\,\mathrm{M}$) is in part due to the spin-dependent potential used to construct the torus and therefore impacting the accretion process and initial magnetic field distribution. On the other hand, magnetic flux also piles up near the horizon due to rotation of the Kerr black hole.

Figure 6 shows time-averaged plasma β, density ρ and magnetization σ in one quadrant of the region GRRT calculations are carried out in. Due to rotation of the Kerr black hole, magnetic field lines are tangled near the horizon and along the jet onset, leading to a region of very low β that disconnects the so-called jet "spine" from the jet "sheath". The disconnection or sheath onset when moving from the equatorial to the polar region is roughly outlined by both the green dashed

37
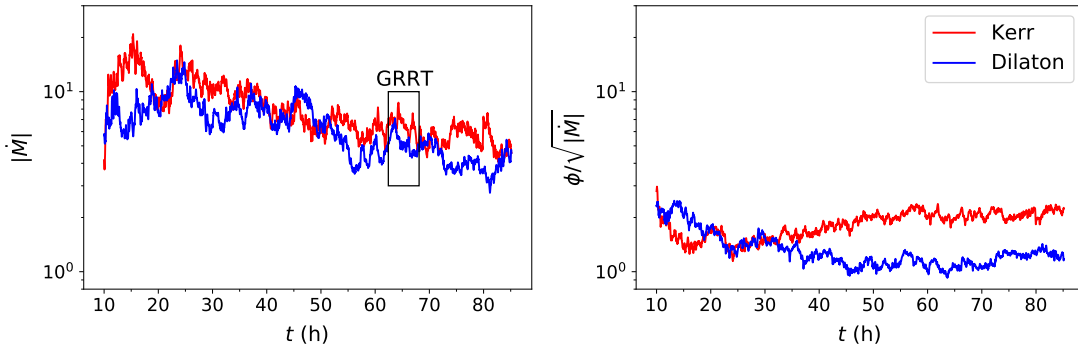
Figure 5: Normalized mass accretion rate, magnetic flux, energy rate and particle kinetic energy rate. The normalizations have been adapted from [102]. In the top left panel, the black box marks the region used for the GRRT images.

contour line in the middle column of figure 6 and the yellow solid line. The former is the relativistic Bernoulli parameter $Be = -h\,u_t = 1.2$, where $Be > 1$ generally describes unbounded gas feeding jet and wind outflow [109], and the latter is $\sigma = 0.1$. Together for an upper value of σ, these boundaries also constrain the region that non-thermal emission will be employed in, as further described in section 6.2.2. Apart from the non-zero spin parameter and a slightly larger horizon, this disconnection is the most significant dynamical difference between the two spacetimes in the system structure.

Since the two black hole systems were matched at the ISCO, their overall dynamical behavior is, unsurprisingly, very similar to one another (M18). The middle and rightmost columns show that the disconnection region is also almost evacuated but highly magnetized ($\beta \ll 1$), a characteristic trait of a jet funnel. In the dilaton system, where no such disconnection is present, the low-β region ($\beta \sim 10^{-2}$) is not as prominent and only extends to $\sim 15\,\mathrm{r}_g$ in the polar direction.

The rightmost column also shows how in the Kerr system, the magnetization in the torus is very low, but very high in the evacuated disconnection region. In the dilaton system, the torus magnetization is slightly higher, but the only highly magnetized region is the jet spine. This has great impact on the total flux of torus-dominated GRRT images, as will be explained in section 6.2.1. Quantitatively, $\sigma_{\mathrm{max}}^{\mathrm{K}} \approx 3.8\,\sigma_{\mathrm{max}}^{\mathrm{D}}$, in a region near the black hole consistent with the fact that magnetic flux accumulates there. This is highlighted by the relation $\beta_{\mathrm{max}}^{\mathrm{K}} \approx 0.6\,\beta_{\mathrm{max}}^{\mathrm{D}}$, since β and σ are inversely proportional. In the Kerr system, the value of plasma β is higher in a very broad region especially in the equatorial plane, shown in the first column.
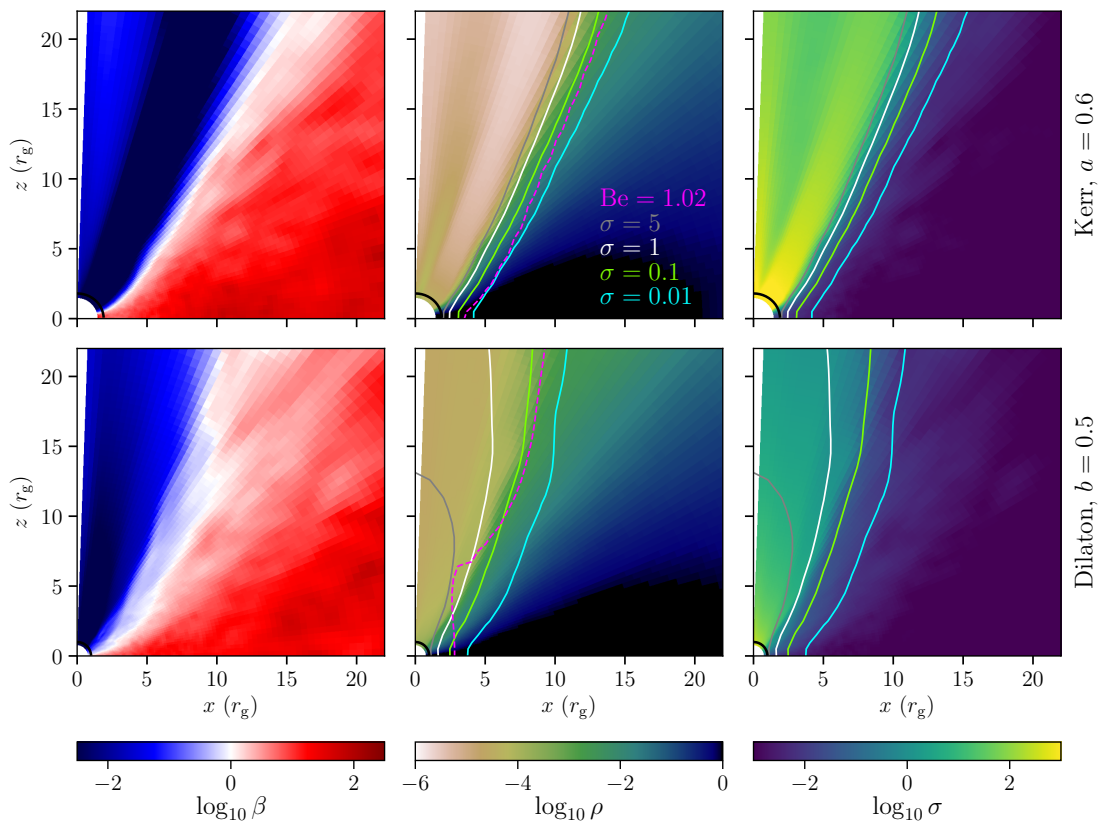
Figure 6: Logarithmic β, ρ and σ. Contour lines: different σ, i.e. common jet sheath definitions, likewise logarithmically plotted. Averaged from $11\,000\,\mathrm{M}$ to $12\,000\,\mathrm{M}$, 101 snapshots. $\beta_{\mathrm{max}}^{\mathrm{K}} = 1033.71$, $\beta_{\mathrm{max}}^{\mathrm{D}} = 1656.15$, $\rho_{\mathrm{max}}^{\mathrm{K}} = 2.63$, $\rho_{\mathrm{max}}^{\mathrm{D}} = 2.61$, $\sigma_{\mathrm{max}}^{\mathrm{K}} = 3561.23$, $\sigma_{\mathrm{max}}^{\mathrm{D}} = 927.47$ (code units). The black line close to $(x, y) = (0, 0)$ shows the event horizon.

Figure 7 is consistent with this analysis. Annotated with $R_{\mathrm{high}} \in \{10, 80, 160\}$, the columns in figure 7 show how by increasing R_{high}, the electron temperature in the torus is decreased. This manifests in the GRRT images as a comparatively brighter jet at larger values of R_{high}, as is shown in section 6.2. The disconnection region in the Kerr spacetime is again clearly visible as a low-temperature band. Contour lines are drawn again to visualize the regions the kappa electron distribution function will be employed in.
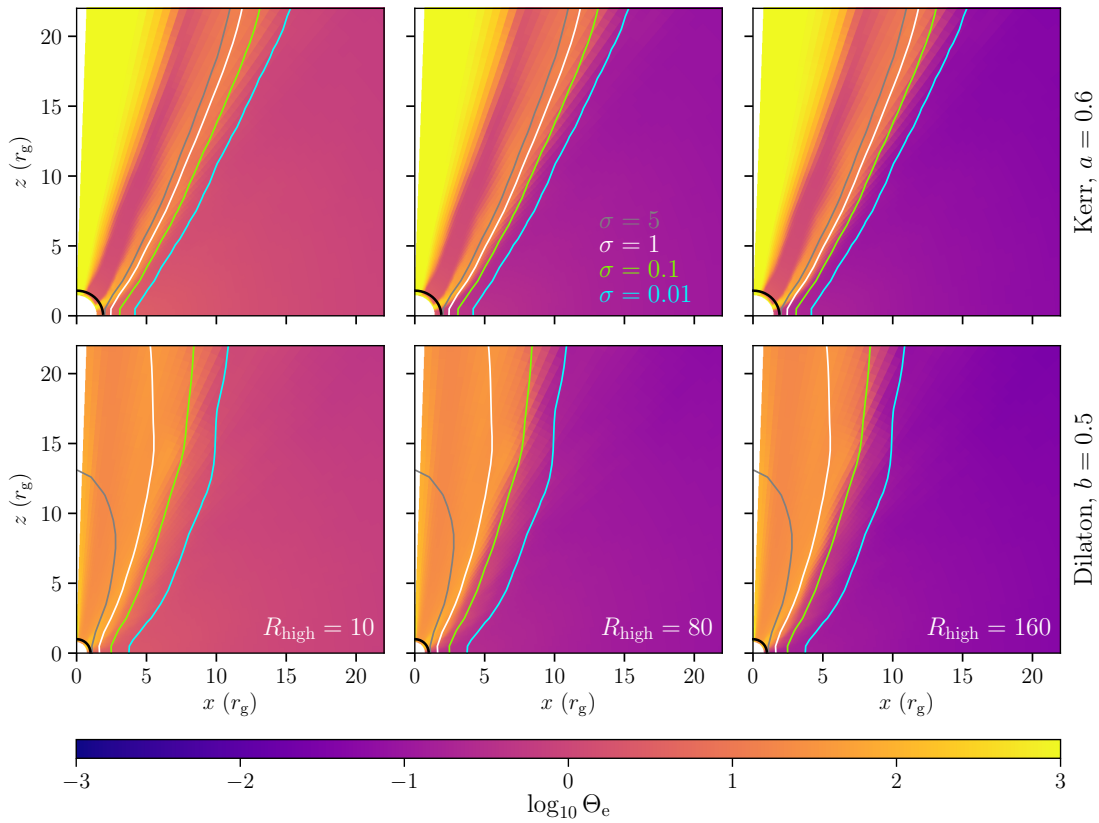
Figure 7: Logarithmic dimensionless electron temeprature Θ_e for three values of R_{high} (see eq. (72)). Contour lines: different σ, i.e. common jet sheath definitions, likewise logarithmically plotted. Averaged from $11\,000\,\mathrm{M}$ to $12\,000\,\mathrm{M}$, 101 snapshots. For $R_{\mathrm{high}} = (10, 80, 160)$: $\Theta_{e,\mathrm{max}}^{\mathrm{K}} = (41773.4, 40086.7, 38282.5)$ and $\Theta_{e,\mathrm{max}}^{\mathrm{D}} = (8639.7, 8443.1, 8228.1)$.

6.2 Imaging with different emission models

In order to produce comparable results, the pioneering work of M18 [48] had to be reproduced accurately. From the GRMHD data, snapshots were taken every 10 M from 11 000 M to 12 000 M, an approximate time span of six hours, and averaged over. The GRRT calculations for the reproduction step were limited to an observational frequency of 230 GHz, table 4 lists the necessary initial conditions for the BHOSS code.

In the pixel-by-pixel differences, all of which calculated by subtracting the dilaton image from the Kerr one, the maximum Kerr brightness overshoot between the images exceeds the one reported in M18 by $\sim 25\,\mu$Jy. The brightness overshoot in the dilaton image was reproduced more accurately: in the reproduction, the overshoot is only $\sim 3\,\mu$Jy larger than in the original release.

The mass accretion rate was normalized at $10,000$ M to reach the target flux of 3.4 Jy at 230 GHz, which was subsequently adjusted to 3.0 Jy to account for adaptations in recent publications [30, 110]. Further, the distance to and mass of the black hole were updated as reported in table 4. Since no emission parameters were changed, these adjustments only scale the total flux in the image. It shows a decline in both spacetimes of ~ 0.5 Jy due to the lower target flux at 230 GHz for the $10,000$ M snapshot.

After successfully reproducing M18, two types of emission models could be employed: the electron temperature parametrization and non-thermal emission. In order to not introduce both models at once, first only the electron temperature was parametrized and emission was left purely thermal (section 6.2.1). The non-thermal electron energy distribution function was employed in the following step (section 6.2.2).

eDF	R_{high}	$\dot{M}_{\mathrm{K}}/(10^{-7}\,\mathrm{M}_\odot/\mathrm{yr})$	$\dot{M}_{\mathrm{D}}/(10^{-7}\,\mathrm{M}_\odot/\mathrm{yr})$
th.	$T_{\mathrm{p}}/T_{\mathrm{e}} = 3$	0.102	0.096
th.	10	0.651	1.10
	80	2.37	4.20
	160	2.37	5.21
$\epsilon = 0$	10	0.657	1.12
	80	2.46	4.55
	160	3.52	5.72
$\epsilon = 0.015$	10	0.657	1.12
	80	2.43	4.55
	160	3.37	5.66

Table 5: Mass accretion rates for all Kerr and dilaton model configurations ($a = 0.6$, $b = 0.504$). In the first column, "rep." denotes the M18 reproduction step with $T_{\mathrm{p}}/T_{\mathrm{e}} = 3$, and the second column contains thermal ("th.") and kappa models with $\epsilon \in \{0, 0.015\}$. $\dot{M}$ obtained by multiplying the BHOSS accretion parameter by the GRMHD accretion rates $\dot{M}_{\mathrm{K,D}}^{\mathrm{C}}$ at the same time-stamp: $10\,000\,\mathrm{M}$, $\dot{M}_{\mathrm{K}}^{\mathrm{C}} = 5.97$ and $\dot{M}_{\mathrm{D}}^{\mathrm{C}} = 3.70$ (code units), measured at the event horizon. All $\dot{M}$ obtained to fit the $230\,\mathrm{GHz}$ flux to $3\,\mathrm{Jy}$ at that time stamp.
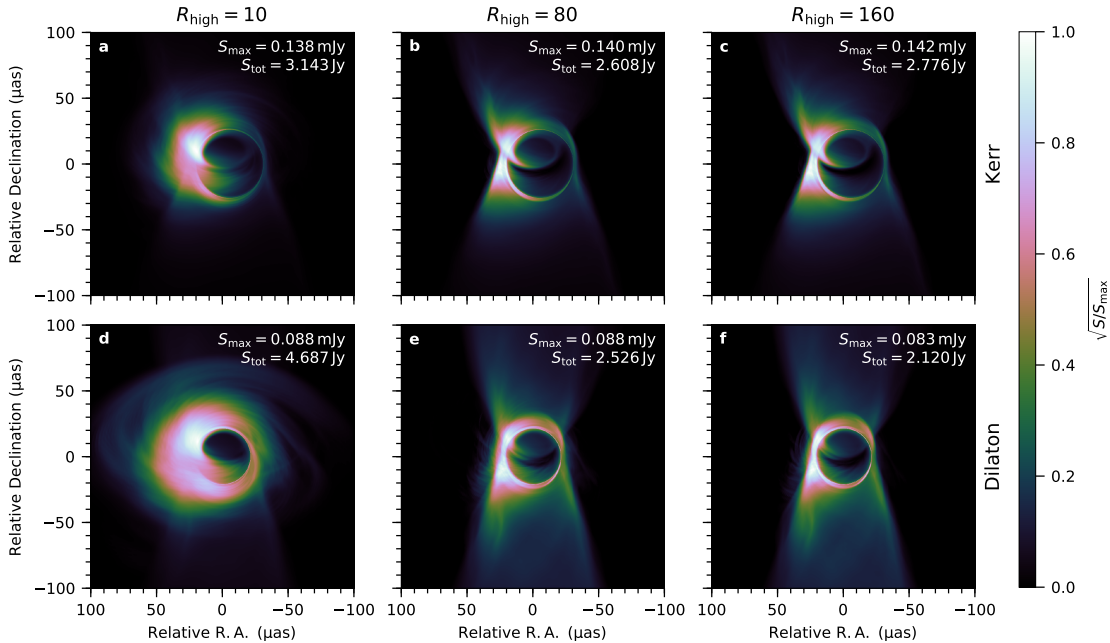
Figure 8: Effect of the $R(\beta)$ parametrization. Top row: Kerr, bottom row: dilaton black hole. Purely thermal emission, at $340\,\mathrm{GHz}$, averaged over 101 snapshots taken from $11{,}000\,\mathrm{M}$ to $12{,}000\,\mathrm{M}$. The color scale is displayed square rooted to highlight the effect.

6.2.1 Thermal emission

The $R(\beta)$ parametrization of the proton-to-electron temperature ratio has by far the most prominent effect on the GRRT images, dividing them into two categories: torus-dominated ($R_{\mathrm{high}} = 10$) and jet-dominated configurations ($R_{\mathrm{high}} = 80, 160$). Figure (8) shows a representative set of six images at $R_{\mathrm{high}} = 10, 80, 160$. All images are taken at $340\,\mathrm{GHz}$ in purely thermal emission; the normalized flux is plotted square rooted to highlight details. Annotated are maximum and total fluxes.

With increasing R_{high}, a clear upward trend is visible in the accretion rate (see table 5). As briefly touched upon in the previous section, an increase in R_{high} decreases the electron temperature in the disk. Additionally, the distributions of β in the systems are different in extent and strength. Figure (6) shows that in the Kerr spacetime, in the torus β values near the maximum are reached in a larger region compared to the dilaton system, while in the Kerr jet β drops to very small values. These regions of high or low plasma β are caused by low or high magnetization, respectively. Since the electron temperature is inversely proportional to the parametrization expression (71), high values of β and R_{high} result in loss of flux from the disk that has to be compensated by the now dominant jet region by increasing the accretion rate.

For $R_{\mathrm{high}} = 10$, both black holes exhibit a torus extending both further inward and outward for the dilaton black hole since there is more distance to cover for accreted matter due to the smaller event horizon, consistent with M18. Increased Doppler beaming around the Kerr black hole leads to significant differences in the brightness distributions between the spacetimes in the torus-dominated configurations. Due to the inclination of $60°$ and the orientation of the spin axis, the flux maximum lies in the northwest section of each image. These features are universal to all selected frequencies, they however vary in extent.

Figure 8 shows that at $340\,\mathrm{GHz}$, in the Kerr spacetime at zero relative declination the emission region is mostly confined to $\sim 25\,\mathrm{\mu as}$ in the east-west and $\sim 60\,\mathrm{\mu as}$ in the north-south direction on the approaching limb. The receding side is almost invisible due to Doppler beaming in the direction facing away from the observer. From the approaching limb, two emission "arcs" trace the northern and southern

43

edges of the shadow, while another split arc spans about two thirds over to the receding side across the shadow.

In the dilaton images, the arcs visible across the Kerr shadow merge to a veil on the southern half of the shadow. The $\sim 30\,\%$ emission region stretches $\sim 20\,\mu$as further out in the west direction, with an extended peak flux drop-off region. The latter is even prominently visible below the veil onset. The torus appears even thicker because of the difference in shadow sizes: as the systems are matched at the ISCO, the dilaton black hole has a smaller horizon and therefore a smaller shadow. Since the dilaton black hole does not rotate, Doppler beaming is not enhanced by the black hole spin and the receding side is more prominent compared to the Kerr images. Low-intensity filaments extend outwards up to $\sim 30\,\mu$as from the main emission region.

Between Kerr and dilaton images, the pixel-by-pixel maps obtained by subtracting the dilaton from the Kerr image show differences of the order of some tens of micro-Janskys. They back up and emphasize previous observations: The Kerr images are brighter in a region spanning $\sim 20\,\mu$as east-west and $\sim 50\,\mu$as north-west, at the east edge of the horizon. Apart from the arc across the horizon, the dilaton images are brighter everywhere else, which is again due to the reduced Doppler beaming.

Between Kerr and dilaton images there is a $\sim 1.5\,$Jy total flux difference, which is due to the differences in magnetization in the systems (see fig. (6)). Since $340\,$GHz shows the optically thinnest emission of the three selected frequencies, the inner regions of the torus contribute significantly to the observed flux. Since in the dilaton system the torus is more magnetized, the plasma β does not push down the electron temperature as much as in the Kerr system. This difference in flux decreases with observational frequency and fixed R_{high}, as further shown below. Since emission from within the jet is neglected, for larger R_{high} this difference will also decrease.

Moving to $230\,$GHz, the approaching limb containing the peak of maximum brightness extends $\sim 30\,\mu$as in the east-west and $\sim 90\,\mu$as in the north-south direction, while the receding limb is still barely visible at all. The approaching side in the dilaton spacetime spans $\sim 50\,\mu$as in the east-west and $\sim 90\,\mu$as in the north-south direction. Across the Kerr shadow, the splitting of the emission arc is now clearer and it stretches almost all the way across the southern half of the shadow. The feature of an horizon-spanning arc is also present in the result of M18, the flux

around the maximum brightness point however drops off more quickly into a region $\sim 30\,\%$ of the peak flux in the images obtained here. This drop-off region is again surrounded by thin 10–20 % filaments. Other than the existence of emission arcs across and along the shadow, the main difference in source structure compared to M18 is the wide aforementioned $\sim 30\,\%$ region covering the southern parts of the images.

While the region of 100 to $\sim 60\,\%$ of the maximum flux has a similar extent on the approaching side for both spacetimes, albeit showing "smeared out" flux levels in the dilaton system, in the latter case a thin 60 % "tail" extends along the northern edge of the shadow. The pixel-by-pixel differences again highlight prominent Doppler boosted emission on the approaching side of the Kerr system , while the dilaton system exhibits filamentary structures from $\sim 30\,\mu$as from the center outwards in all directions. The amplitude (absolute value) of these differences is comparable to 340 GHz, at about 40 μJy maximum.

In the 86 GHz images, the torus is optically thick. Torus dominated images for both spacetimes show the it as a large region uniformly emitting at $\sim 20\,\%$ of the maximum flux. The southern half of the black hole shadow is always obscured, and the main emission region $\gtrsim 40\,\%$ of the maximum concentrates in the inner side of the northern part of the torus and lower jet onset. Compared to higher frequencies, the region of peak emission is extended significantly especially in the Kerr case. The total fluxes of Kerr- and dilaton images lie around 1.125 Jy within a few hundredths; this is due to only the outer "shell" of the torus contributing to the radiation. There, the magnetization in both black hole systems is comparable. Coming from 230 GHz images, pixel-by-pixel differences decrease by an order of magnitude at 86 GHz, to $\sim 5\,\mu$Jy. They show the Kerr system to be brighter within $\lesssim 50\,\mu$as of the shadow, and the dilaton system to exhibit a brighter but relatively faint region extending further outwards. This extension can also be explained by only the outer layers in the torus contributing to the emission (in addition to the jet onset). Some "spots" near the black hole, where the dilaton system is brighter, are caused by the asymmetry of the shadows, as is more clearly visible for higher frequencies.

For $R_{\text{high}} = 80$, the source structure changes fundamentally from a torus-dominated system towards a jet onset extending outwards into thin, long filaments (middle column of figure 8). For both spacetimes, the main part of the emission comes

from two "hot-spots" located at the northern and southern halves of the approaching limb. Since the source structure is identical up to variations in intensity of features at 340 and 230 GHz, they are discussed together.

Up to $\sim 30\,\mu$as outwards from the edge of the shadow, the source structures of Kerr- and dilaton images are over all very similar. In the dilaton system, the region of highest emission is slightly smaller. A faint arc extends across the shadow starting at the northern hot-spot, along the upper edge of the inner (not visible) torus. The arc turns north-ways before reaching the receding side and seemingly merges back into the northern emission, forming the foot of the observer-facing jet.

The prominent difference between Kerr and dilaton images is the jet onset structure. In the Kerr system, the flux drops off to $\lesssim 5\,\%$ of the maximum within $\sim 20\,\mu$as of the $\sim 30\,\%$ flux region towards the north and south directions, forming a thin filament-like jet– and counter-jet onset.

In the dilaton images, below the jet foot, rest emission from the torus is visible on the lower part of the shadow. As was the case for the torus-dominated models, the dilaton system exhibits more emission on the receding side concentrated on the north-west side of the shadow.

In the dilaton counter-jet, a tail-like structure extends south-wards from the lower emission region on the approaching side. Both observer-facing and counter-jet onsets are more clearly visible compared to the Kerr images, with the lower-flux filamentary emission region conically extending twice as far out. Directly comparing Kerr- and dilaton images, the jet opening angle seems wider in the Kerr case. This is due to the disconnection of jet sheath and spine by a region of very high magnetization, created by magnetic field lines tangling up in a conic shape due to the Kerr black hole's rotation. This disconnection leads to a jet onset simply wider in the east-west direction, not with a different opening angle. This can be easily verified by the pixel-py-pixel difference maps. As mentioned above, the total fluxes are comparable between Kerr and dilaton systems and lie around 2.5 Jy for the higher frequencies.

While showing the jet onset a lot more clearly compared to higher frequencies, the shadow in the 86 GHz, $R_{high} = 80$ images remains obscured. The inner side of the torus is visible as a dark band across the shadow, separating a northern and a southern emission region for both systems. The Kerr jet opening angle now is indeed slightly wider than in the dilaton system, and within the southern emission

region the peak is extended in the east-west direction. For the dilaton black hole, this southern peak emission region is split into two bright spots on the east- and west sides of the counter-jet.

For $R_{\mathrm{high}} = 160$, the source structure does not significantly change anymore (rightmost column of figure 8). The electron temperature in the torus is already very low at $R_{\mathrm{high}} = 80$, and therefore pushing it down even further has little effect. At R_{high} values this high, the flux loss from pushing down the electron temperature in the torus even further can be smaller than the flux gain from enhancing the jet region. For this reason, at 230 and 340 GHz, Kerr $R_{\mathrm{high}} = 160$ images show a higher total flux compared to $R_{\mathrm{high}} = 80$ (an effect of $\sim 0.1\,\mathrm{Jy}$). Since in the dilaton system less magnetic flux is concentrated in the jet sheath, the total flux for $R_{\mathrm{high}} = 160$ is $\sim 0.4\,\mathrm{Jy}$ smaller than for $R_{\mathrm{high}} = 80$. This enhances the total flux difference between spacetimes: while for $R_{\mathrm{high}} = 80$ the total fluxes were generally comparable between Kerr- and dilaton systems, the difference increases to half a Jansky for $R_{\mathrm{high}} = 160$. While at 86 GHz the torus is opaque, the jet onset is clearly visible; here, $R_{\mathrm{high}} = 160$ images exceed both $R_{\mathrm{high}} = 80$ and even $R_{\mathrm{high}} = 10$ images in total flux. This is again because only little flux lost by suppressing the opaque torus.

GRRT calculations lead to best-case infinite resolution images. However, in the real world the resolution is limited by the telescopes, imaging algorithm and various effects introducing random errors on visibility phase and amplitude. Since the goal of this work is to compare the two black hole systems, any random effects such as interstellar scattering, thermal noise and station-based gain terms accounting for electronics were excluded. This highlights the importance of including 340 GHz in this study, as scattering and plasma effects are believed to be suppressed at higher frequencies. These effects are usually modeled by a diffractive kernel and a refractive scattering, respectively, and depend on the inverse square of the observational wavelength [111]. Still, it is imperative to explore what effect the process of an observation in principle has on the images and interpretations. Synthetic VLBI data is generated from all GRRT models and images are reconstructed from these mimicked observations. The observation parameters are listed in table 1.

For all reconstructed images, features are of course significantly blurred out compared to the GRRT images. At 340 GHz, the torus-dominated Kerr images reduce to an emission region extending $\sim 80\,\mu\mathrm{as}$ in the north-south and $\sim 40\,\mu\mathrm{as}$ in the

east-west direction. Beyond that, the flux drops below $\sim 5\,\%$ of the maximum. In the dilaton spacetime, the black hole shadow is fully enclosed by a $\sim 30\,\%$ emission region (in contrast ot the Kerr system). The torus also stretches further out. Filamentary, low-flux features from the GRRT images do not survive the observation process and disappear in residual noisy features the algorithm needs to reach the target flux.

At $230\,\mathrm{GHz}$, the source size does appear larger, extending to $\sim 100\,\mu\mathrm{as}$ north-south and $\sim 70\,\mu\mathrm{as}$ in the east-west in the Kerr system. What used to be the arcs spanning across and following the edges of the horizon in the GRRT images, is now barely visible as a "dent" in the emission region $\sim 50\,\%$ of the peak flux, just south of the $\gtrsim 80\,\%$ region containing the peak. The shadow appears smaller in the reconstructed image because the lower half of it is fully obscured by the now blurred-out arcs. Note that in the Kerr system the shadow is fully enclosed only by a very low flux region on the receding side, while in the dilaton case the shadow is clearly visible as such.

As is the case at $R_{\mathrm{high}} = 10$, in the $R_{\mathrm{high}} = 80$ and $R_{\mathrm{high}} = 160$ images only the most prominent structural source features carry over from GRRT but all small-scale features are blurred out. The Kerr shadow is only fully enclosed at $R_{\mathrm{high}} = 160$, while the reduced Doppler beaming in the dilaton case always leads to a clearly visible receding side. Comments about the jet opening angle cannot be made anymore since only the first $\sim 10\,\mu\mathrm{as}$ of the onset of the observer-facing jet survive the reconstruction process. The trend in total flux discussed above however carry over, as the total flux is a constraint given to the reconstruction algorithm.

6.2.2   Non-thermal emission

The kappa electron distribution function (section 4.1) is employed restricted by boundary values of σ and a lower bound for the Bernoulli parameter $Be = -h\,u_t$. In this work, $0.1 \leq \sigma \leq 1.0$, where the lower bound $\sigma_{\min} = 0.1$ roughly separates the jet from the torus region, clearly visible in the dilaton panels of figure 6, while simultaneously enabling us to use the variable kappa fit functions obtained by Ball *et al.* 2018 with confidence. In the Kerr system, $\sigma_{\min}$ separates the jet sheath from the torus, while $\sigma_{\max} = 1.0$ defines the end of the jet "wall" towards the polar region. $\sigma_{\max}$ is chosen by employing different upper bounds for σ until the total flux in the GRRT images becomes roughly insensitive to this change. $Be = -h\,u_t \geq 1.02$ is chosen based on [109], where $Be > 1$ generally describes unbounded gas feeding jet and wind outflow. Figure 6 shows how the Bernoulli parameter constraint again reduces the region the kappa model is applied in. Further, any emission from within the jet spine and partly even the sheath, i.e. from past $\sigma_{\max}$ towards the polar region, is neglected.

Within one R_{high} segment, it could naively be assumed that employing a kappa model would decrease the accretion rate since the power-law tail increases the number of high-energy electrons, requiring less accretion to reach the target flux. However, in this work kappa is not constant but variable, depending on magnetization σ and plasma β (equations (75)–(78)). The distribution turns out to not have a sufficient effect to let the accretion rate drop when keeping R_{high} constant.

Due to the kappa distribution function being employed only in such a small region, the source structure is entirely unaffected. For a given spacetime and R_{high}, the total flux in the GRRT images differs between thermal and kappa models by some hundredths of a Jansky. Differences in source structure are however to be expected at larger field of view (FOV), where the jet emission generally dominates over the torus, which will be part of a future study. Further, in the literature other ways to employ the kappa distribution have been investigated, e.g. for a percentage of electrons instead of a spatial region [91]. It remains questionable whether these methods would change the result obtained here. At the FOV used in this work, non-thermal emission would play a more important role for hot spots ("plasmoids") orbiting closely around the black hole, as these are best modeled by non-thermal electrons [112].

At 230 and 340 GHz, emission by high energy electrons is more pronounced and their increased abundance in the kappa model leads to a flux higher by a few tenths of micro-Janskys in these images. This effect, while apparent for any R_{high}, is particularly small in the torus-dominated configurations as emission from the region the kappa model is employed in is suppressed further. At $R_{\mathrm{high}} = 80$, the Kerr and dilaton total fluxes are $\sim 2.6\,\mathrm{Jy}$ at 340 and $\sim 2.3\,\mathrm{Jy}$ at 230 GHz, while for $R_{\mathrm{high}} = 160$ there is a $\sim 0.1\,\mathrm{Jy}$ increase for Kerr and a $\sim 0.3\,\mathrm{Jy}$ decrease for the dilaton system. This is, unsurprisingly, consistent with the trend in purely thermal emission.

Except for the $R_{\mathrm{high}} = 10$ dilaton configurations, at both 230 and 340 GHz the images with $\epsilon = 0$ are brighter compared to $\epsilon = 0.015$ by a few milli-Janskys. This was to be expected since the magnetic field contribution that ϵ controls widens the distribution function and shifts its maximum in the process. As explained above, at high frequencies the high-energy electrons contribute more to the emission, leading to the thermal images being the dimmer compared to the kappa models.

Figure 9 shows GRRT and reconstructed images for a representative configuration chosen based on the l^2 norm of the pixel-by-pixel differences (see section 6.3).

At 86 GHz, the kappa images show a lower total flux compared to the purely thermal ones, again by a few tenths of milli-Janskys, since the high energy electrons contribute less to the emission. Additionally, the thermal core of the kappa distribution has a lower maximum compared to a purely thermal distribution, leading to a smaller number of electrons in the lower energetic domain wherever the kappa model is applied. For all R_{high}, the total flux is comparable to $\sim 1.2\,\mathrm{Jy}$.

The total flux constraint in the synthetic VLBI imaging algorithm is robust enough for the trends in total flux described above to carry over to the reconstructed images, albeit less pronounced. Any difference in source structure is due to numerical noise; the kappa distribution of course cannot have more influence on reconstructed images than on GRRT ones.
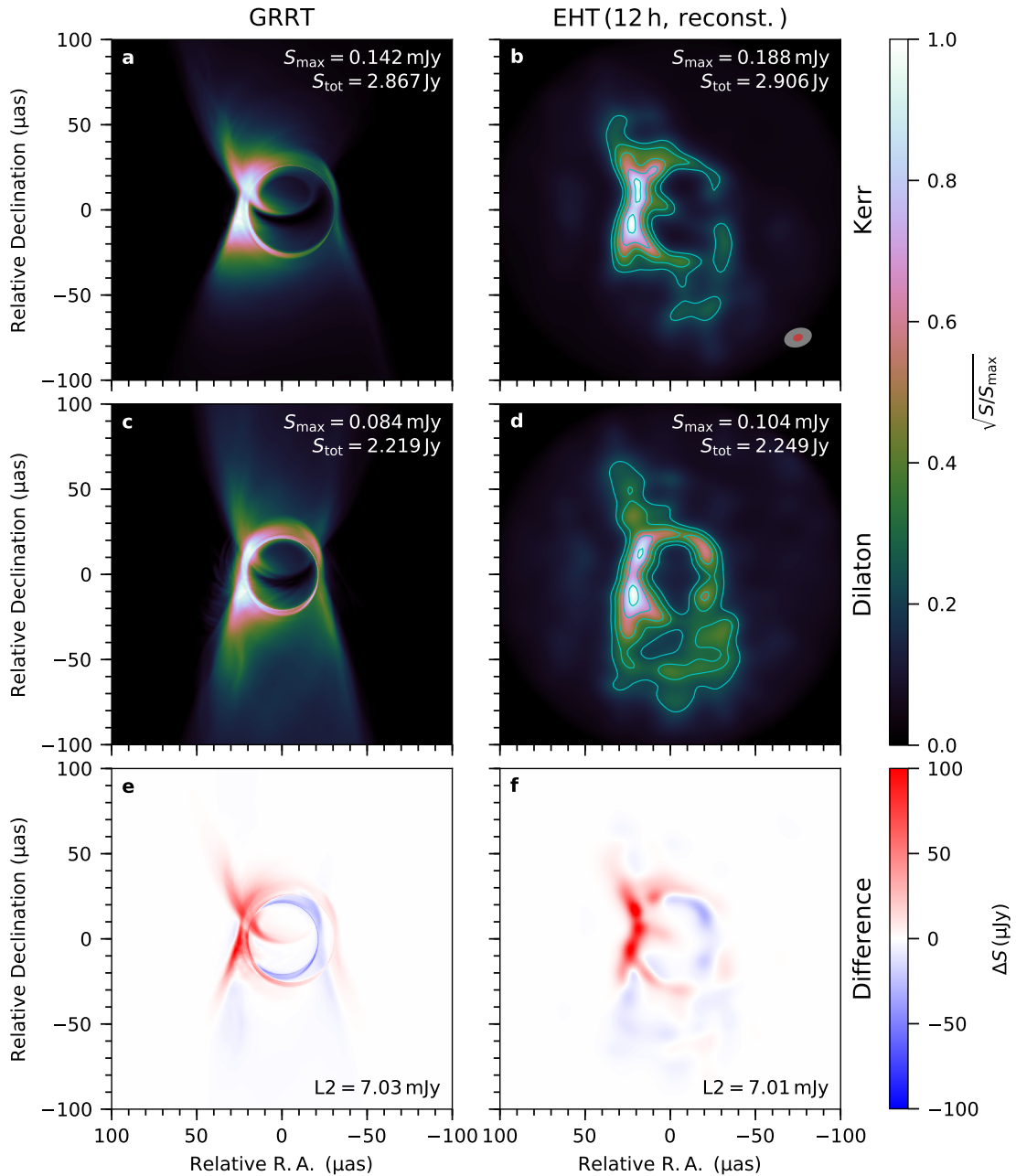
Figure 9: GRRT images and reconstructions from a mimicked 12 h observation by the EHT 2017 configuration [34, 35], updated to 340 GHz. $R_{high} = 160$, non-thermal emission with $\epsilon = 0$. Left column: GRRT Kerr, dilaton, and pixel-by-pixel difference plots. Right column: Reconstructed images and pixel-by-pixel difference between the reconstructions. Annotated are maximum and total fluxes $S_{max, tot}$, emission model (top left), observing beam and the 30 % fraction (top right), and the l^2 norms of the differences. The top four plots are shown square rooted, while differences are shown in linear scale. Contour lines range from 80 % of the peak flux down to 5 % in factors of two. In the top right panel the beam size is shown as grey ellipse, with its 30 % fraction in red on top.
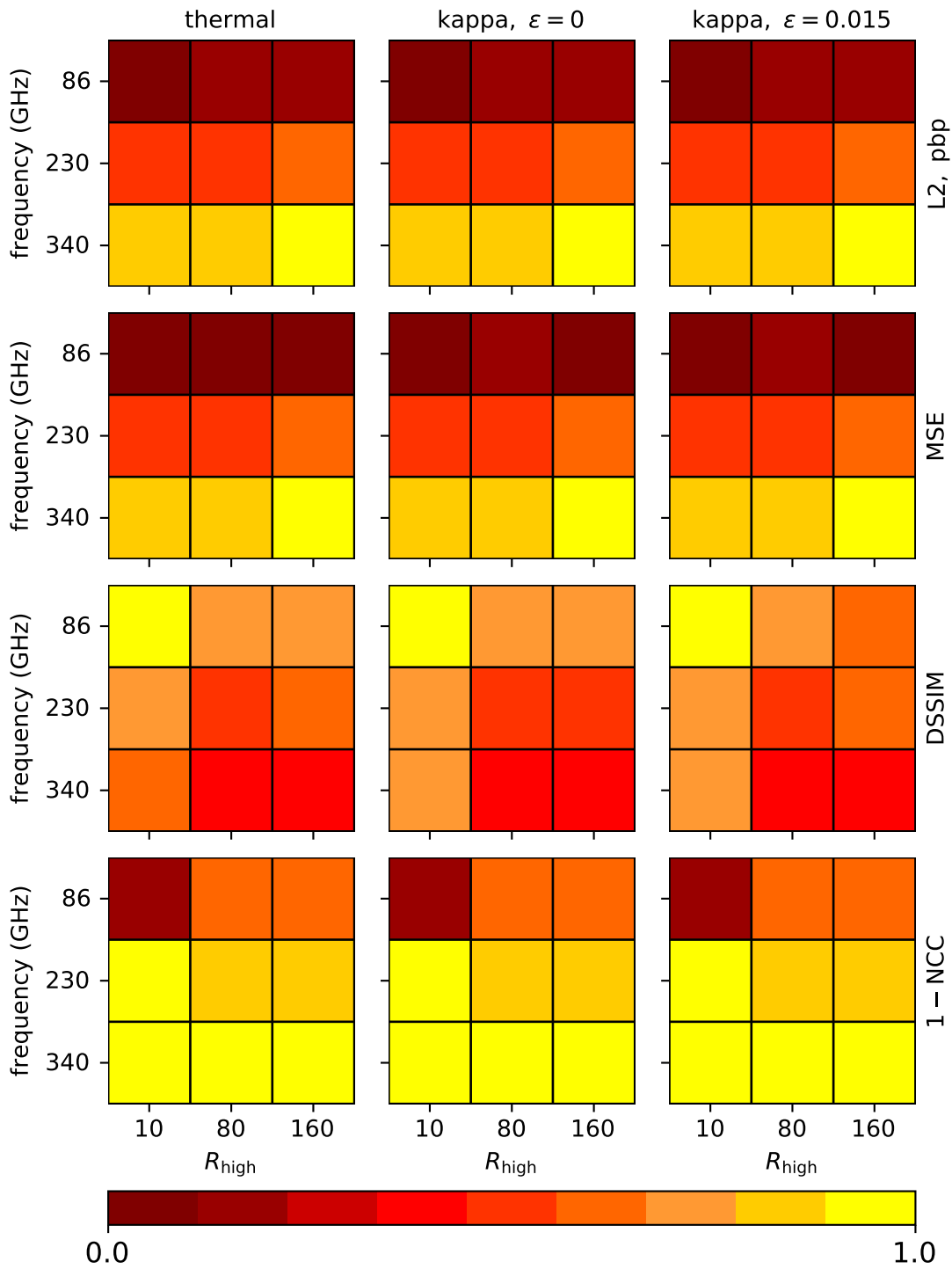
Figure 10: Maps of normalized image comparison metrics.

6.3 Comparing Kerr– and dilaton black holes

In order to compare the two spacetimes, it is convenient to quantify differences with a single number. Here, the l^2 norm of the pixel-by-pixel differences along with MSE, DSSIM and $1-$NCC between reconstructed images are chosen, as explained in section 2.3. Figure 10 shows normalized maps for each metric.

For one electron distribution function, l^2 grows monotonically from 86 GHz and $R_{\text{high}} = 10$ to 340 GHz and $R_{\text{high}} = 160$ such that the growth is continuous when reading one 3×3 plot from left to right and top to bottom. The field with the highest value for the norm, 340 GHz, $R_{\text{high}} = 160$ and $\epsilon = 0$ is chosen as a representative model and can be seen in figure 9. The corresponding visibility amplitudes are shown in figure 11.

The MSE exhibits a similar gradient compared to l^2, apart from a small change in gradient for the kappa models at 340 GHz and $R_{\text{high}} = 160$. This is to be expected since the definitions of MSE and l^2 are very similar (equations (16) and (17)). The MSE maxima are $\simeq 0.007$.

Monotonic growth is lost for the DSSIM. It behaves in a completely non-linear way, disqualifying it as robust image comparison metric. The biggest issue of the DSSIM is its dependence on the FOV: Given that no other image features become visible when increasing the FOV, the DSSIM can become arbitrarily low. It is therefore generally to be interpreted with great care or exchanged with a more robust metric.

The $1-$NCC gradient is monotonous up to 230 GHz and $R_{\text{high}} = 10$ for all distribution functions; it is however less sensitive than the MSE. The maxima are at $\lesssim 0.11$, indicating that the images are very similar to one another. While visual differences are striking, this high cross-correlation is due to the small pixel-by-pixel differences in between Kerr an dilaton images.

Overall, highest pixel-by-pixel differences are up to a few tenths of micro-Janskys, in both the Kerr- and the dilaton direction (referring to which system is brighter). At 340 and 230 GHz, the peak of "Kerr brightness" is roughly twice the dilaton peak, regardless of emission model. Moving to 86 GHz, the difference peaks become comparable at only $\sim 3\,\mu$Jy.

In torus-dominated configurations, the Kerr system is brightest in a region $\sim 20 \times 20\,\mu$as located at the northern half of the approaching limb. At 340 GHz the dila-

ton system is then brighter in a ring around that. This carries over to 230 GHz, but less bright arcs stretch out west-wards from the slightly enlarged Kerr zone surrounding the peak.

Between $R_{\text{high}} = 80$ and 160, the structure of the pixel-by-pixel difference maps does not change significantly. The region surrounding the Kerr difference peak of up to $\sim 100\,\mu\text{Jy}$ forms a bent north-south arc on the approaching side, about $50\,\mu\text{as}$ long and $50\,\mu\text{as}$ wide. This arc splits in a north and a south region at 230 GHz and the Kerr peak is halved.

All these differences can be connected with conclusions from the previous sections. The difference maps highlight Doppler beaming, optical thickness and the distribution of plasma β in the system.

Up to this point, comparisons and interpretations were made in image space. Interferometric data is however recorded in the form of visibilities, as explained above. Figure 11 shows visibility amplitudes for Kerr and dilaton black holes in the representative configuration along with the absolute differences.

On the "zero" baseline, an interferometer measures the total flux in the image as "largest-scale" structure. Up to $\sim 5\,\text{G}\lambda$ in $u - v$ distance, the similarity between curves indicates similar behavior up to intermediate-scales in the image domain. Between $\sim 7 - 9\,\text{G}\lambda$, similarity is lost and only partially regained at the longest baselines measuring the smallest-scale structures. Visibility amplitude curves for different electron energy distributions are indistinguishable from one another. Over the whole range of $u - v$ distance, absolute differences generally lie above $1\,\text{mJy}$, which is the maximum sensitivity the EHT can offer in its 2017 configuration (on some baselines) [36]. The sensitivity on other baselines is however still just $10\,\text{mJy}$, which again most differences are above. This detectability is to be taken with a grain of salt: this work merely scratches the surface of the available parameter space. It is unclear whether degeneracies can be produced by changing R_{high}, observer inclination, matching between black hole systems, or by including new accretion and emission processes along with new spacetime backgrounds. Likewise, for the sake of comparability, nor random effects are included that any real-world observation is subjected to.

For the parameters and models considered in this work, a comparison between spacetimes is best done in image space. Moving to visibility (or Fourier) space will be the go-to strategy once actual observational data comes into play. While
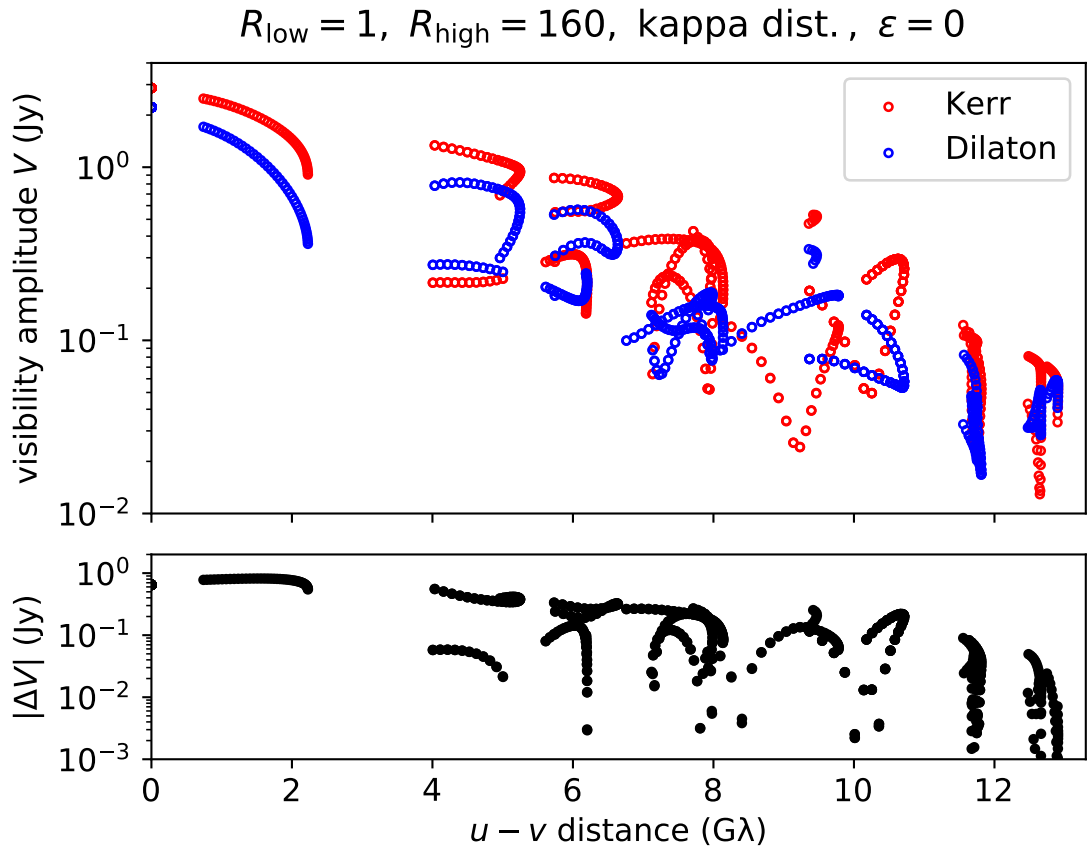
Figure 11: Top panel: visibility amplitudes for Kerr and dilaton black holes in a 12 h observation campaign. Bottom panel: absolute differences between the amplitude curves.

for the black hole systems considered here there are clear visual differences that have a counterpart in the reconstructed images, such as the shadow appearance and structure of the approaching limb, a broader sweep of the parameter space is necessary to assess the ability to distinguish.

7 Summary, conclusions and outlook

In this work, with the goal of distinguishing a Kerr- from a dilaton black hole, GRRT calculations and synthetic VLBI imaging were carried out on a GRMHD simulation performed by Mizuno *et al.* 2018 [48]. Simulated were a Kerr black hole with dimensionless spin $a = 0.6$ and a non-rotating dilaton black hole with $b = 0.504$, where the systems were matched at the ISCO. GRMHD quantities such as accretion rate and flux measured at the event horizon as well as plasma β, density and magnetization up to $\sim 20\,\mu$as from the black holes were analyzed to explain the physics behind the features found later in the GRRT images. From the GRMHD simulations, the overall behavior of the two systems is similar up to the fact that only the Kerr black hole is rotating. This causes a jet wall to disconnect from the jet spine, a feature that probably would be present in a rotating dilaton black hole system as well. This disconnection therefore does distinguish the two systems analyzed in this work, but not the spacetimes per se. Variations in total flux and behavior of mass accretion rates back up this conclusion.

After reproducing the GRRT results found in the initial work of Mizuno *et al.*, two new emission models were employed: the parametrization of electron temperature depending on plasma β and a parameter R_{high} [81], and the kappa electron distribution function [82, 89, 90]. The parameter space spans $R_{\mathrm{high}} \in \{10, 80, 160\}$, dividing the model configurations into torus– ($R_{\mathrm{high}} = 10$) and jet-dominated models ($R_{\mathrm{high}} = 80, 160$). Furthermore, three electron energy distributions were considered: thermal, and kappa with and without magnetic energy contribution ($\epsilon \in \{0, 0.015\}$). On this parameter space, GRRT images are calculated over $\sim 6\,\mathrm{h}$ ($1\,000\,\mathrm{M}$) and synthetic VLBI data is generated to compute reconstructed images mimicking a real-world observation. Similarities between these images are quantified by pixel-by-pixel differences and their l^2 norm, a well as the behavior in visibility amplitudes.

As mentioned in section 6.2.1, conclusions from GRRT images have to be drawn with care [48]. In reality, one does not have the luxury of being able to arbitrarily increase the resolution to investigate even the smallest image features. Again, differences in the plasma flow are due to the rotation of the Kerr black hole and the associated distribution of plasma β (and, in turn, magnetization) in the torus and jet wall. An important new feature however is the differently shaped black-hole shadow, also affecting the image shadow [113].

Wei and Liu [77] showed that black hole spin and dilaton parameter do not produce a degeneracy in the shape of shadows, characterizing deviations in terms of the shadow radius of the corresponding non-rotating case and the difference at the most deformed point. In this work, only a non-rotating dilaton black hole was compared to a rotating Kerr black hole to enhance possible differences compared to a scenario including a dilaton black hole with nonzero spin. Matching the systems at the ISCO lead to comparable accretion dynamics but left the event horizons, and therefore the shadows, to be of different shapes. This setup poses a scenario specifically created to show clear visual differences between dynamically similar systems. However, as explained in section 6.3, other free parameters such as the observer inclination also have significant impact on the source structure and shadow appearance.

The shadows in the GRRT images are clearly distinguishable: The Kerr shadow is asymmetric and off-centered, while the the dilaton shadow is circular and smaller. For jet-dominated configurations, the image shadow [113] matches the black-hole shadow up to a thin emission arc spanning across the horizon tracing the foot of the observer-facing jet. Torus-dominated models show the clearest difference in both source structure and total flux and exhibit obscured black-hole shadows. In conclusion, parameterizing the proton-to-electron temperature has the main impact in the extension of the Mizuno *et al.* study. The effect of non-thermal emission on the other hand only is negligible, due to the small region the kappa distribution is applied to and the small FOV. In the future, an increase in FOV in the imaging may reveal characteristic features on larger scales in the jet wall.

Introducing reconstructed images from synthetic VLBI data unsurprisingly does not improve the ability to distinguish spacetimes. While Wei and Liu argued that the EHT sensitivity would likely be sufficient to deduce spin and dilaton parameter from a 1 mm VLBI observation, the work of Mizuno *et al.* already showed this was not the case. Low-flux filamentary structures are blurred to the point where it is no longer possible to distinguish between physical feature and numerical noise, while the more prominent features merge to larger regions especially in the torus. The image shadow sizes are only significantly different in the jet models but technically require a more in-depth analysis, such as the one carried out in [39]. This might be hindered by the fact that in the jet configuration the torus is often not enclosed by emission regions.

With the currently available models, it is not possible to unambiguously distinguish between the configuration of Kerr- and dilaton spacetimes. The visual differences are explainable and well consistent with the underlying physical processes. In the future, a wider range of emission parameters as well as inclination, spin, and other quantities characterizing the background will increase the parameter space significantly. Shadow geometries can be measured by analyzing the intensity profiles along perpendicular slices through the GRRT and synthetic images, as was done for example in the EHT paper VI [39], obtaining posterior distributions on the deviations of observed angular sizes from those supplied by real-world measurements. In regards to imaging, including different accretion models such as the MAD configuration will motivate polarimetric imaging to analyze magnetic fields in the direct vicinity of black holes [114, 115]. Further, with the source variability of Sgr A* in mind, dynamical imaging [116] is another step up from the static image analysis carried out in this work.

A   Physical constants

Symbol	SI units
c	$299{,}792{,}458\,\mathrm{m\,s^{-1}}$
G	$6.6738 \times 10^{-11}\,\mathrm{m^3\,kg^{-1}\,s^{-2}}$
k_B	$1.3807 \times 10^{-23}\,\mathrm{m^2\,kg\,s^{-2}\,K^{-1}}$
$M_\odot$	$1.9885 \times 10^{30}\,\mathrm{kg}$
m_e	$9.1094 \times 10^{-31}\,\mathrm{kg}$
$m_\mathrm{p}/m_\mathrm{e}$	1836.152

B   Camera setup

In the following, the quantities from equations (105)–(106) are listed as they are defined in [98].

$$X \equiv \mathcal{D}\cos\phi_{\mathrm{obs}} - x\sin\phi_{\mathrm{obs}}\,, \tag{110}$$

$$Y \equiv \mathcal{D}\sin\phi_{\mathrm{obs}} + x\cos\phi_{\mathrm{obs}}\,, \tag{111}$$

$$Z \equiv r_{\mathrm{obs}}\cos\theta_{\mathrm{obs}} + y\sin\theta_{\mathrm{obs}}\,, \tag{112}$$

$$\sigma \equiv \left(X^2 + Y^2 + Z^2 - a^2\right)/2\,, \tag{113}$$

$$\mathcal{D} \equiv \sin\theta_{\mathrm{obs}}\sqrt{r_{\mathrm{obs}}^2 + a^2} - y\cos\theta_{\mathrm{obs}}\,. \tag{114}$$

The derivatives of equations (105)–(107) read:

$$-\Sigma\,\dot{x}^r = r\mathcal{R}\sin\theta\sin\theta_{\mathrm{obs}}\cos\Phi + \mathcal{R}^2\cos\theta\cos\theta_{\mathrm{obs}}\,, \tag{115}$$

$$-\Sigma\,\dot{x}^\theta = \mathcal{R}\cos\theta\sin\theta_{\mathrm{obs}}\cos\Phi - r\sin\theta\cos\theta_{\mathrm{obs}}\,, \tag{116}$$

$$\mathcal{R}\,\dot{x}^\phi = \sin\theta_{\mathrm{obs}}\sin\Phi\,\mathrm{cosec}\,\theta\,, \tag{117}$$

with

$$\Sigma \equiv r^2 + a^2\cos^2\theta\,, \quad \mathcal{R} \equiv \sqrt{r^2 + a^2}\,, \quad \Phi \equiv \phi - \phi_{\mathrm{obs}}\,, \tag{118}$$

and the time component is

$$\dot{x}^t = \beta + \sqrt{\beta^2 + \gamma}\,, \tag{119}$$

with

$$\beta \equiv -\frac{g_{ti}\,\dot{x}^i}{g_{tt}}\,, \quad \gamma \equiv \frac{\delta - g_{ij}\,\dot{x}^i\dot{x}^j}{g_{tt}}\,, \tag{120}$$

where latin indices $\{i, j\}$ range from 1 to 3, denoting spatial components.

C Matching characteristic radii

Below, characteristic radii for Kerr– and dilaton spacetimes are listed together with the expression for the dilaton parameter corresponding to a spin of the Kerr black hole when equating (matching) the radii.

Event horizon

$$r_{\text{eh, K}} = M + \sqrt{M^2 - a^2}, \tag{121}$$

$$r_{\text{eh, D}} = 2(M - b), \tag{122}$$

$$b_{\text{H}} = \frac{1}{2}\left(M - \sqrt{M^2 - a^2}\right), \tag{123}$$

Photon Orbit

$$r_{\text{ph, K}} = 2M\left(1 + \mathcal{C}\right), \tag{124}$$

$$r_{\text{ph, D}} = \frac{1}{2}\left[3(M - b) + \sqrt{(M - b)(9M - b)}\right], \tag{125}$$

$$b_{\text{P}} = \frac{1}{2}M\left(-2 - 3\mathcal{C} + \sqrt{8 + \mathcal{C}(\mathcal{C} + 8)}\right), \tag{126}$$

Innermost stable circular orbit

$$r_{\text{isco, K}} = M\left[3 + Z_2 - (3 - Z_1)(3 + Z_1 + 2Z_2)\right], \tag{127}$$

$$r_{\text{isco, D}} = 2M\left(\mathcal{B} + \mathcal{B}^2 + \mathcal{B}^3\right), \tag{128}$$

$$b_{\text{I}} = M\left[1 + \frac{1}{27}\left(1\sigma - \frac{2}{\sigma}\right)^3\right], \tag{129}$$

where $(x = a/M)$

$$\mathcal{C} = \cos\left[\frac{2}{3}\cos^{-1}(-x)\right], \tag{130}$$

$$\mathcal{B} = \left(1 - \frac{b}{M}\right)^{1/3}, \tag{131}$$

$$Z_1 = 1 + \sqrt[3]{1 - x^2}\left(\sqrt[3]{1 + x} + \sqrt[3]{1 - x}\right), \tag{132}$$

$$Z_2 = \sqrt{3x^2 + Z_1^2}, \tag{133}$$

$$\sigma^3 = -\frac{7}{2} + \frac{3}{4M}\left(-9\,r_{\text{isco, K}} + \sqrt{36M^2 + 84M\,r_{\text{isco, K}} + 81\,r_{\text{isco, K}}^2}\right). \tag{134}$$

60

D The kappa electron distribution function

In the following, non-extensive thermodynamics and the kappa electron distribution function will be derived in greater detail. This section will follow closely the description of Livadiotis and McComas 2009 [89].

D.1 Boltzmann-Gibbs statistics

In Boltzmann-Gibbs (BG) (often also referred to Maxwell-Boltzmann) statistics, entropy is defined as

$$S = - \sum_i^W p_i \ln p_i \, , \tag{135}$$

with probabilities p_i and the total number of states W. The system is said to be in thermal equilibrium (in the sense of the canonical ensemble) and the probabilities satisfy the following two constraints,

$$(a) \ \sum_i^W p_i = 1, \ \ (b) \ \sum_i^W p_i \, \varepsilon_i = U \, , \tag{136}$$

i. e., the probability distribution is normalized and the internal energy U is the expectation value of energy eigenvalues ε_i. In order to obtain an explicit expression for the probability distribution, the entropy needs to be maximized under constraints (136). Making use of the method of Lagrange multipliers,

$$0 \overset{!}{=} \frac{\partial}{\partial p_j} \left[- \sum_i^W p_i \ln p_i + \lambda_1 \sum_i^W p_i + \lambda_2 \sum_i^W p_i \, \varepsilon_i \right]$$

$$\Leftrightarrow \ \ln p_j = \lambda_1 - 1 + \lambda_2 \, \varepsilon_j$$

$$\Leftrightarrow \ \ \ p_j = e^{\lambda_1 - 1} e^{\lambda_2 \, \varepsilon_j} \, .$$

Using now again the above constraints with the expression for p_j,

$$1 \overset{!}{=} \sum_i^W p_i = \sum_i^W e^{\lambda_1 - 1} e^{\lambda_2 \, \varepsilon_i} \ \Leftrightarrow \ e^{\lambda_1 - 1} = \left(\sum_i^W e^{\lambda_2 \, \varepsilon_i} \right)^{-1} \, ,$$

$$U \overset{!}{=} \sum_i^W p_i \, \varepsilon_i = \left(\sum_k^W e^{\lambda_2 \, \varepsilon_k} \right)^{-1} \left(\sum_i^W \varepsilon_i \, e^{\lambda_2 \, \varepsilon_i} \right) \, .$$

The first result, eliminating λ_1 from the equation, has already been inserted in the

second line. Further, the expression for λ_2 can be simplified by introducing the partition function Z,

$$Z \equiv \sum_i^W e^{\lambda_2 \varepsilon_i} \Rightarrow U = \frac{\partial \ln Z}{\partial \lambda_2} \,. \tag{137}$$

The second Lagrange multiplier is set to be the negative inverse temperature, $\lambda_2 = -\beta$. The full probability distribution now reads (dropping the indices for continuous description)

$$p = \frac{1}{Z} e^{-\beta \varepsilon} \,, \tag{138}$$

and is called Boltzmann distribution. Assuming the energy of particles in a gas can be described purely kinetically, the energy expression is simply $\varepsilon = \frac{1}{2} \mu \, u^2$ with particle mass μ and speeds u [89]. The resulting Maxwell-Boltzmann distribution, due to its derivation in thermal equilibrium often and hereafter referred to as "thermal distribution", reads

$$p = \frac{1}{\tilde{Z}} e^{-(u/\theta)^2}, \quad \theta^2 \equiv \frac{2T}{\mu} \tag{139}$$

where the partition function has been modified accordingly, denoted by $\tilde{Z}$. Here, the notation of Livadiotis and McComas [89] has been adapted for consistency with the following sections. The first step towards a connection between BG statistics and both the "kappa distribution" and a generalized version of statistical mechanics, is to mathematically deform equation (139), described in section D.2.

Use of Maxwellian distributions in research

Even though Maxwellian curves might fail to describe an increasing number of observational data, in the past they have been in use especially to investigate low-energy plasmas. Gruntman [117] for example used a two-dimensional Maxwellian curve to fit the distribution of plasma protons in order to calculate the distribution of "HELENAs" (heliospheric energetic neutral atoms); similarly, Hammond et al. [118] fitted multiple Maxwellians to ion beams in the solar wind. The following section will clarify why upon developing detectors for higher energies the Maxwellian distribution becomes less viable to describe newly observed phenomena.

D.2 The kappa electron distribution function

In 1968, Vasyliunas introduced the kappa distribution as a generalized Maxwellian with variable κ, versions of the distribution with a fixed value for κ had been used in foregoing research. In search of the velocity distribution of the electrons in Earth's magnetosphere, he had discovered that fitting a Maxwellian to the lower energies was underestimating the high energy channels [86]. Therefore, the chosen distribution connected a Maxwellian low-energy region with a power law to fit the upper end of the spectrum:

$$f(v) = \frac{N}{\omega_0^3} \frac{\Gamma(\kappa+1)}{(\pi\kappa)^{3/2} \Gamma\left(\kappa - \frac{1}{2}\right)} \left(1 + \frac{v^2}{\kappa\omega_0^2}\right)^{-(\kappa+1)}, \tag{140}$$

where N and ω_0 are the total number density and the most probable speed, respectively, and κ is the power law exponent for the high energy region. In the limit $\kappa \to \infty$, the Maxwell distribution is recovered; the temperature is then defined by the Energy E_0 corresponding to ω_0. Using equation (140) to fit the distribution of observed electrons, Vasyliunas was however neither able to constrain κ better than ± 2, nor to determine its physical significance properly due to insufficient energy range coverage of the detector towards high energies [86]. Moreover, his motivation to introduce the new distribution was entirely empirical.

Mathematical quasi-derivation

The form of a kappa distribution can be reproduced mathematically by deforming the Maxwellian curve (139) [89, 119]. Here, this is referred to as "quasi-derivation" since it merely serves as a motivation of why the kappa distribution is viable for scientific use. In order to perform said deformation, the exponential first needs to be expressed in the form of a limit [89]:

$$e^x = \lim_{\kappa \to \infty} \left(1 - \frac{x}{\kappa}\right)^{-\kappa}, \ \kappa \in \mathbb{R}^+, \tag{141}$$

where κ is, for now, only an arbitrarily named real positive number. Comparing this expression with (139), x can be read off and inserted, yielding ([89] and references therein)

$$p \sim \lim_{\kappa \to \infty} \left[1 + \frac{1}{\kappa}\left(\frac{u}{\theta_\kappa}\right)^2\right]^{-\kappa}, \tag{142}$$

where θ_κ is a general form of θ that is a function of κ. This expression clearly

recovers the Maxwellian distribution (139) in the limit $\kappa \to \infty$; it is therefore important to discuss whether finite κ represent physical states as well (states out of equilibrium) instead of just $\kappa \to \infty$, and if equation (142) is able to describe observed physical systems [89].

Even though it is likewise possible to arrive at a kappa distribution by deriving it directly from BG statistics, the results will only be mathematically correct. This will become evident when the inconsistency of the kappa distribution with BG statistics is discussed in section D.3.

Kappa electron distributions describing plasmas

As stated above, the power-law tail is the defining feature of the kappa distribution in contrast to the widely used Maxwellian curve. The need for generalizations of the Maxwellian distribution increased with observations of space plasmas, which turned out to exhibit non-thermal properties in the high-energy regime in a variety of cases. Decker *et al.* [120] find that anomalous cosmic rays measured by Voyager 1 at the edge of the solar system follow a power law at high energies, while Fisk and Gloeckler [121] find a supra-thermal "tail" in the distribution of accelerated ions in the solar wind.

Low– and high-energy limits of equation (140) do indeed reproduce a Maxwellian "core" and a high-energy power-law "tail", as shown in [89]:

$$p\left(\vec{u};\,\theta_{\kappa};\,\kappa\right) \sim \left[1 + \frac{1}{\kappa}\left(\frac{|\vec{u} - \vec{u}_b|}{\theta_{\kappa}}\right)^2\right]_{+}^{-\kappa-1} \sim \begin{cases} \exp\left(-\dfrac{\vec{u}^2}{\theta_{\kappa}^2}\dfrac{\kappa+1}{\kappa}\right) & \text{low-en.} \\ |\vec{u} - \vec{u}_b|^{-2(\kappa+1)} & \text{high-en.} \end{cases} \tag{143}$$

Where the notation of Livadiotis & McComas (2009) has been adapted. $\vec{u}$ and $\vec{u}_b$ are the particle and bulk flow velocities, and θ_{κ} is the "characteristic speed-scale parameter" [89]. It will become evident in section D.4 that the second term in the outer square bracket in the distribution is proportional to the energy. In a simplified fashion, with a dimensionless quantity x proportional to the energy, $p \sim [1 + x]^{-\kappa-1}$ and therefore for low energies (small x): $\ln p \sim \ln(1 + x) \simeq x$, leading to the upper term in equation (143). The high energy approximation is straightforwardly obtained as $p \sim [1 + x]^{-\kappa-1} \simeq x^{-\kappa-1}$ for large x [89].

Since negative values of κ are not inherently excluded, a cutoff condition is employed such that $|\vec{u} - \vec{u}_b| < \sqrt{|\kappa|}\,\theta_{\kappa}$ for $\forall \kappa < 0$. This ensures for the argument in square brackets in equation (143) to be positive, denoted by the "+" subscript,

and is often referred to as "Tsallis cutoff condition" [89, 122, 123].

While over the years various values of κ have been employed and investigated, a lower bound is imposed by requiring the mean energy integral to converge (then, for large u, so does the normalization integral), i. e.

$$\int_0^\infty p(u)\, g_V(u)\, du < \int_0^\infty u^2\, p(u)\, g_V(u)\, du < +\infty\,. \tag{144}$$

Equation (143) shows that the kappa distribution exhibits a power law-like decay towards high energies in contrast to the classical exponential decay. In order for equation (144) to hold, the integrand has to decay like u^{-r} with $r > 1$ in the high-energy limit [89]. Assuming a spherical symmetry, the density of speed states becomes $g_V(u) = 4\pi u^2$ and therefore the second integrand in equation (144) decays with $r = 2\kappa - 2$. This leads to a lower limit of $\kappa > 3/2$.

D.3 Derivation from equilibrium statistics

Regardless of the problematic physical implications, it is possible to derive a kappa distribution from well-known BG statistics. Past attempts include generalizations of statistical mechanics [124] or inverse construction of constraints for entropy maximization [125]. A general formulation of these advances can be reduced to exchange of the internal energy constraint (136b) as [89]

$$\sum_i^W p_i \, \varepsilon_i \equiv \langle \varepsilon \rangle \equiv U \quad \longrightarrow \quad \sum_i^W p_i \, \varphi\left(\varepsilon_i\right) \equiv \langle \varphi\left(\varepsilon\right) \rangle \equiv \varphi\left(U_\varphi\right) . \tag{145}$$

Following now the steps in section D.1 and arbitrarily setting $\varphi\left(\varepsilon\right) = \ln\left(\varepsilon\right)$, the derivation yields a power-law distribution instead of the Maxwellian curve

$$p \sim \varepsilon^{-\beta} . \tag{146}$$

As is the case for BG statistics, the second Lagrange parameter is inversely related to the temperature [89]. Keeping generality, the energy is set to consist of a kinetic and a non-kinetic part; substituting this assumption into the power-law distribution, the result reads

$$p \sim \left[1 + \frac{1}{\kappa}\left(\frac{u}{\theta_\kappa}\right)^2\right]^{-\kappa} , \tag{147a}$$

where

$$\varepsilon \equiv \varepsilon_0 + \frac{\mu}{2}u^2, \quad \kappa \equiv \beta = -\lambda_2, \quad \theta_\kappa \equiv \sqrt{\frac{2\varepsilon_0}{\mu\kappa}} . \tag{147b}$$

As before, μ is the particle mass, u is the bulk velocity, and ε_0 is a non-kinetic factor [89]. Equation (147) has taken the form of equation (142), however the value of κ is not restricted to the limiting case but instead all values are allowed. It is further important to note that equation (147) differs slightly from the form of distribution that will be derived in section D.4. It is referred to as the "first kind" of kappa distribution, with exponent $-\kappa$, in contrast to the more widely used and adapted "second kind" with index $-(\kappa+1)$ [89]. It will also become evident that this duality is connected to the concept of "ordinary" and "escort" probability distributions in Tsallis statistics.

Calculating the logarithmic mean with equation (145), i.e. substituting the arbitrary function φ with the logarithm as $\langle \varphi\left(\varepsilon\right) \rangle = \langle \ln\left(\varepsilon\right) \rangle \equiv U_{\ln}$, and normalizing

yields

$$U_\varphi = U_{\ln} = \frac{3}{2} T_K \, e^{\frac{3}{2} \frac{c_\kappa}{\kappa}} \left(\frac{3}{2} \frac{c_\kappa}{\kappa} \right)^{-1} \equiv \varepsilon_0 \, e^{\frac{3}{2} \frac{c_\kappa}{\kappa}} \,, \tag{148}$$

where c_κ is a function of kappa and set to be [89]

$$c_\kappa \equiv \frac{2\kappa}{3} A_\kappa \int_0^\infty \left[1 + \frac{1}{\kappa} \left(\frac{u}{\theta_\kappa} \right)^2 \right]^{-\kappa} \ln \left[1 + \frac{1}{\kappa} \left(\frac{u}{\theta_\kappa} \right)^2 \right] 4\pi \left(\frac{u}{\theta_\kappa} \right)^2 d \left(\frac{u}{\theta_\kappa} \right) \,, \tag{149}$$

with a normalization factor $A_\kappa \equiv A(\kappa)$ to ensure that $\lim_{\kappa \to \infty} c_\kappa = 1$. The kinetic temperature T_K then enters the distribution (147) by introducing

$$\theta_{\text{eff}} = \sqrt{\frac{2T_K}{\mu}} \,, \tag{150}$$

and therefore, substituting into (147),

$$p \sim \left[1 + \frac{c_\kappa}{\kappa} \left(\frac{u}{\theta_{\text{eff}}} \right)^2 \right]^{-\kappa} . \tag{151}$$

While the above calculation is mathematically correct, the physical implications disqualify it as a viable derivation of statistical mechanics for a number of reasons [89]. First and foremost, equation (148) implies that

$$\varepsilon_0 = T_K \frac{c_\kappa}{\kappa} \,, \tag{152}$$

which has to be the definition of temperature since, as stated above, $\kappa \equiv \beta = -\lambda_2$ removes the temperature dependence of the exponent. Physically this means that temperature is given a priori by equation (152) instead of being developed as $T = (\partial_S U)_{V,N}$, which is unacceptable [89]. Further, equation (148) shows that $U_{\ln}$ is not constant for isothermal processes as is required by the laws of thermodynamics. Finally, with equation (147 b) a recovery of the Maxwellian curve from equation (151) in the limit $\kappa \to \infty$ implies $-\lambda_2 \to \infty$ [89]; this is likewise catastrophic since λ_2 is normally the connection of statistical mechanics to a well-defined temperature.

In section D.4 it will turn out that by using Tsallis instead of BG statistics, the aforementioned issues are naturally resolved and physical temperature will be well-defined to be the kinetic temperature for systems in and out of equilibrium.

D.4 Non-equilibrium statistics

20 years after Vasyliunas' empirical advances, Tsallis published his first work on a "possible generalization of Boltzmann-Gibbs statistics" [87] postulating the following definition of entropy:

$$S_q \equiv \frac{1 - \sum_{i=1}^{W} p_i^q}{q - 1}, \tag{153}$$

which satisfies $S_{BG} = \lim_{q \to 1} S_q$, and $\sum_{i=1}^{W} p_i = 1$. Further properties of this entropy definition, such as the "pseudo-additivity" have been investigated ever since (for a full characterization of the entropy postulate see [126] and references therein). The rule of additivity is likewise modified [88] and reads

$$S_q(A + B) = S_q(A) + S_q(B) + (1 - q)\, S_q(A)S_q(B). \tag{154}$$

The case $q = 1$ recovers the BG statistics additivity (equivalently, the extensivity), $q \lessgtr 1$ therefore describes sub–/superextensivity. If the subsystems A and B are however not entirely independent, equation (154) might either not hold at all or there might be a q^* that restores its classical form :

$$S_{q^*}(A + B) = S_{q^*}(A) + S_{q^*}(B) \tag{155}$$

i. e. without the third term on the right hand side (but with $q = q^*$) [126]. In order to develop statistical mechanics from S_q it has to be extremized under a set of constraints as demonstrated for the canonical ensemble of BG statistics in section D.1.

Clearly, the first constraint is for the probability distribution to be normalized. The second constraint on the other hand requires a more detailed treatment, as explained below. Intuitively the internal energy expression reads

$$\sum_{i=1}^{W} p_i\, \varepsilon_i = U, \tag{136 b revisited}$$

as is known from BG statistics, or, since we already modified the entropy in a similar fashion,

$$\sum_{i=1}^{W} p_i^q\, \varepsilon_i = U. \tag{156}$$

Both versions of this constraint however lead to unwanted consequences, such as divergences of equation (144) in the former case, or non-invariance of the obtained probability distribution under shift of the energy ground state in the latter case [88]. These issues are resolved when choosing

$$\frac{\sum_{i=1}^{W} p_i^q \, \varepsilon_i}{\sum_{j=1}^{W} p_j^q} = U \iff \sum_{i=1}^{W} P_i \, \varepsilon_i = U, \ P_i = \frac{p_i^q}{\sum_{j=1}^{W} p_j^q} \, , \tag{157}$$

with the so-called escort probabilities P_i that all expectation values in Tsallis statistics are calculated with [88, 126, 127]. The extremization equation now reads

$$0 \overset{!}{=} \frac{\partial}{\partial p_j} \left(\frac{1 - \sum_i^W p_i^q}{q-1} \right) + \lambda_1 \frac{\partial}{\partial p_j} \left(\sum_i^W p_i \right) + \lambda_2 \frac{\partial}{\partial p_j} \left(\frac{\sum_{i=1}^W p_i^q \, \varepsilon_i}{\sum_k^W p_k^q} \right) \tag{158\,i}$$

$$\iff p_j = \left(\lambda_1 \frac{q-1}{q} \right)^{-\frac{1}{1-q}} [1 - (1-q)\beta_q \, (\varepsilon_j - U_q)]^{\frac{1}{1-q}} \tag{158\,ii}$$

$$\iff p_j \equiv \frac{1}{\tilde{Z}_q} \exp_q \left(-\beta_q \, (\varepsilon_j - U_q) \right), \ \beta_q = \frac{\beta}{\sum_k^W p_k^q} \equiv \frac{\beta}{\phi_q} \, , \tag{158\,iii}$$

where in the last equation the q-deformed exponential was introduced. Along with the q-deformed logarithmic, unit, and gamma functions, it is defined as [89]

$$\exp_q(x) \coloneqq (1 + (1-q)x)^{\frac{1}{1-q}} \, , \tag{159}$$

$$\ln_q(x) \coloneqq \frac{1 - x^{1-q}}{q-1} \, , \tag{160}$$

$$1_q(x) \coloneqq 1 + (1-q)x \, , \tag{161}$$

$$\Gamma_q^{(1)} \coloneqq \int_0^\infty dy \, \exp_q(-y) \, y^{a-1} \, , \tag{162}$$

$$\Gamma_q^{(2)} \coloneqq \int_0^\infty dy \, \exp_q(-y)^q \, y^{a-1} \, . \tag{163}$$

For details on the q-deformed gamma functions of first and second kind (162, 163) see Appendix A of [89]. Equations (159-163) recover the non-deformed expressions in the limit $q \to 1$ and are a matter of convenience. They reappear many times over in Tsallis statistics and are therefore abbreviated as shown. The last line in the extremization calculation (158 iii) implies also

$$T_q \equiv T \, \phi_q \, , \tag{164}$$

which will become important discussing the physical temperature at the end of this section.

Escort probabilities

Using functions (159)-(161), the probability distribution derived above can be rewritten in a more consistent manner. Here, it is directly generalized to continuous energy spectra [89, 128] and the density of states $g_E(\varepsilon)$ is accounted for. The second equality is the escort distribution.

$$p\left(\varepsilon\right) = \frac{\exp_q\left[-\frac{\beta_q\,\varepsilon}{1_q(\beta_q\,U_q)}\right]}{\int_0^\infty d\varepsilon\,\exp_q\left[-\frac{\beta_q\,\varepsilon}{1_q(\beta_q\,U_q)}\right]g_E(\varepsilon)}\,, \tag{165}$$

$$P\left(\varepsilon\right) = \frac{\exp_q\left[-\frac{\beta_q\,\varepsilon}{1_q(\beta_q\,U_q)}\right]^q}{\int_0^\infty d\varepsilon\,\exp_q\left[-\frac{\beta_q\,\varepsilon}{1_q(\beta_q\,U_q)}\right]^q g_E(\varepsilon)}\,. \tag{166}$$

From here, a series of steps is required in order to arrive at the form of kappa distribution widely used in the literature, where the distribution exponent and argument are functions of kappa and the temperature, respectively[3]. Normalizing the probabilities, i.e. $P\left(\varepsilon, a, q\right) \to P\left(\varepsilon, \beta_q, q\right)g_E\left(\varepsilon\right)$, moving from energy to speed representation and taking the energy to be purely kinetic [89],

$$P\left(u, \theta_q, q\right)g_V(u) = \frac{2}{\theta_q^{2a}\,\Gamma_q(a)}\,\exp_q\left[-\left(\frac{u}{\theta_q}\right)^2\right]^q u^{2a-1},\ \theta_q \equiv \sqrt{1_q(a)\frac{2T_q}{\mu}}\,. \tag{167}$$

The internal energy is calculated as

$$U_q = \frac{\int_0^\infty d\varepsilon\,P(\varepsilon, a, q)\,g_E(\varepsilon)\,\varepsilon}{\int_0^\infty d\varepsilon\,P(\varepsilon, a, q)\,g_E(\varepsilon)} \tag{168 i}$$

$$\Leftrightarrow\quad U_q = \frac{1_q\left(\beta_q\,U_q\right)}{\beta_q}\frac{a}{1_q(a)} \tag{168 ii}$$

$$\Leftrightarrow\ U_q\,\beta_q = a\,, \tag{168 iii}$$

where $a = f/2$ and f is the degrees of freedom. This leads to, setting $f = 3$

$$U_q = \frac{3}{2}\,T_q\,, \tag{169}$$

---

[3]Since a detailed derivation can be found in Appendix B of [89], only the most important steps will be recalled here.

with the physical temperature T_q as previously commented on. In equations (168) the dependencies of P have been written explicitly to specify the representation unambiguously.

With kinetic energy exclusively, the temperature is likewise purely kinetic and, with equation (169), leads to

$$U_q = \frac{3}{2} T_{\mathrm{K}}.$$ (170)

Comparing equations (170) and (169), it is evident that

$$T_q = T_{\mathrm{K}},$$ (171)

i. e. the physical and kinetic temperature coincide in and out of equilibrium. It is important to note that this does not happen if the statistical moments were computed with the ordinary probability distribution, emphasizing the crucial role of the escort probabilities in Tsallis statistics. Repeating the calculation (168) with the ordinary distribution function, equation (171) takes the form

$$T_{\mathrm{K}} = \frac{T_{q^*}}{1_{q^*}(1)}$$ (172)

where the asterisk denotes use of p instead of P. Equation (172) indicates that T_{K} no longer coincides with T_q.

Choosing a well-defined temperature

Before arriving at the widely used kappa distribution, a question related to equation (164) needs to be taken up. Equation (164) relates the Lagrangian temperature T to the physical temperature T_q, not specifying which one is the actual measured temperature of a physical system. On the other hand, equation (171) already strongly hints towards T_q being the correct choice, while equations (169) and (170) make it obvious. If T were the proper temperature, plugging (164) into (169) would imply that the kinetic temperature needed to be a function of q (i.e. $T_{\mathrm{K}} = T \phi_q$) and therefore the internal energy would no longer be invariant for isothermal processes [89].

D. THE KAPPA ELECTRON DISTRIBUTION FUNCTION

D.5 Final remarks

Concluding from above arguments, $T_q \equiv T_K$ can be safely set and an effective speed scale $\theta_{\text{eff}} = \sqrt{2T_q/\mu}$ with single-particle mass μ can be introduced, which can be rewritten using the kappa index as $\theta_\kappa = \sqrt{(\kappa - a)/\kappa}\,\theta_{\text{eff}}$, where $a = f/2 = 3/2$. Further, rewriting of equation (167) leads to [89]

$$p\left(u, \theta_{\text{eff}}, q\right) = \frac{1}{2\pi\,\theta_{\text{eff}}^3} \frac{1}{1_q\left(\frac{3}{2}\right)^{\frac{1}{2}} \Gamma_q^{(1)}\left(\frac{3}{2}\right)} \exp_q\left[-\frac{1}{1_q\left(\frac{3}{2}\right)}\left(\frac{u}{\theta_{\text{eff}}}\right)^2\right], \qquad (173)$$

$$P\left(u, \theta_{\text{eff}}, q\right) = \frac{A(q)}{\pi^{\frac{3}{2}}\,\theta_{\text{eff}}^3}\left[1 + \frac{2(q-1)}{5-3q}\left(\frac{u}{\theta_{\text{eff}}}\right)^2\right]^{-\frac{q}{q-1}}, \qquad (174)$$

$$P\left(u, \theta_{\text{eff}}, \kappa\right) = \frac{A(\kappa)}{\pi^{\frac{3}{2}}\,\theta_{\text{eff}}^3}\left[1 + \frac{1}{\kappa - \frac{3}{2}}\left(\frac{u}{\theta_{\text{eff}}}\right)^2\right]^{-\kappa-1}. \qquad (175)$$

The calculation along with expressions for the normalization constants $A(q)$ and $A(\kappa)$ as well as ϕ_q are included in Appendix B of [89] in great detail.

Equation (175) makes use of the transformation $\kappa \equiv 1/(q-1)$, connecting the deformation q with the kappa index. Including now the bulk velocity $\vec{u}_b$, generalizing to f-dimensional systems and denoting kappa for the ordinary distribution with an asterisk,

$$p\left(\vec{u}, \theta_{\text{eff}}, \kappa^*\right) \sim \left[1 + \frac{1}{\kappa^* - \frac{f+2}{2}}\left(\frac{|\vec{u} - \vec{u}_b|}{\theta_{\text{eff}}}\right)^2\right]_+^{-\kappa^*}, \qquad (176)$$

$$P\left(\vec{u}, \theta_{\text{eff}}, \kappa\right) \sim \left[1 + \frac{1}{\kappa - \frac{f}{2}}\left(\frac{|\vec{u} - \vec{u}_b|}{\theta_{\text{eff}}}\right)^2\right]_+^{-\kappa-1}, \qquad (177)$$

where the "+" subscript again denotes the application of the Tsallis cutoff condition. Both forms of the distributions have been in use in the literature; until the discoveries by Tsallis they were however called the kappa distributions of first and second kind, respectively, as mentioned in section D.3.

Over the years, a variety of different models have been employed and the electron distribution functions have been rewritten to fit problems ad hoc. For example Pandya *et al.* [85], using the notation of Xiao [90], calculate absorption and emission coefficients to be used in e.g. radiative transfer codes. More recently, Davelaar *et al.* [82, 91] have used the same notation modeling emission from jets and accretion disks of supermassive black holes.

E List of abbreviations

AMR adaptive mesh refinement

BHAC black hole accretion code

BHOSS black hole observations in stationary spacetimes

BG Boltzmann-Gibbs

DSSIM structural dissimilarity index

eDF energy distribution function

EOS equation of state

EH event horizon

EHT Event Horizon Telescope

EHTIM EHT-Imaging

FOV field of view

GC Galactic Center

GRMHD general relativistic magnetohydrodynamics

GRRT general relativistic radiative transfer

ISCO innermost stable circular orbit

M18 Mizuno *et al.* 2018

MAD magnetically arrested disk

MSE mean square error

NCC normalized cross-correlation

ODE ordinary differential equation

PO photon orbit

RK4 fourth-order Runge-Kutta algorithm

RZ Rezzolla-Zhidenko

SANE standard and normal accretion

SED spectral energy distribution

SMBH supermassive black hole

SSIM structural similarity index

TSV total squared variation

VLBI very long baseline interferometry

References

[1] G. A. Shields. A Brief History of Active Galactic Nuclei. *PASP*, 111(760):661–678, June 1999.

[2] A. Einstein. Die Grundlage der allgemeinen Relativitätstheorie. *Annalen der Physik*, 354(7):769–822, January 1916.

[3] A. Eckart and R. Genzel. Observations of stellar proper motions near the Galactic Centre. *Nature*, 383(6599):415–417, October 1996.

[4] A. M. Ghez, B. L. Klein, M. Morris, and E. E. Becklin. High Proper-Motion Stars in the Vicinity of Sagittarius A*: Evidence for a Supermassive Black Hole at the Center of Our Galaxy. *The Astrophyiscal Journal*, 509(2):678–686, December 1998.

[5] V. Bromm and A. Loeb. Formation of the First Supermassive Black Holes. *The Astrophysical Journal*, 596(1):34–46, October 2003.

[6] B. Yue, A. Ferrara, R. Salvaterra, Y. Xu, and X. Chen. The brief era of direct collapse black hole formation. *MNRAS*, 440(2):1263–1273, May 2014.

[7] M. Habouzit, M. Volonteri, M. Latif, Y. Dubois, and S. Peirani. On the number density of 'direct collapse' black hole seeds. *MNRAS*, 463(1):529–540, November 2016.

[8] C. J. White, E. Quataert, and O. Blaes. Tilted Disks around Black Holes: A Numerical Parameter Survey for Spin and Inclination Angle. *The Astrophysical Journal*, 878(1):51, June 2019.

[9] V. Mewes, F. Galeazzi, J. A. Font, P. J. Montero, and N. Stergioulas. On the dynamics of tilted black hole-torus systems. *MNRAS*, 461(3):2480–2489, September 2016.

[10] M. Brightman, M. Bachetti, H. P. Earnshaw, F. Fuerst, J. Garcia, B. Grefenstette, M. Heida, E. Kara, K. K. Madsen, M. J. Middleton, D. Stern, F. Tombesi, and D. J. Walton. Breaking the limit: Super-Eddington accretion onto black holes and neutron stars. *Bulletin of the American Astronomical Society*, 51(3):352, May 2019.

[11] Z. Younsi, K. Wu, and S. V. Fuerst. General relativistic radiative transfer: formulation and emission from structured tori around black holes. *Astronomy & Astrophysics*, 545:A13, September 2012.

[12] M. A. Abramowicz and P. C. Fragile. Foundations of Black Hole Accretion Disk Theory. *Living Reviews in Relativity*, 16(1):1, January 2013.

[13] N. I. Shakura and R. A. Sunyaev. Reprint of 1973A&A....24..337S. Black holes in binary systems. Observational appearance. *Astronomy & Astrophysics*, 500:33–51, June 1973.

[14] I. D. Novikov and K. S. Thorne. Astrophysics of black holes. In *Black Holes (Les Astres Occlus)*, pages 343–450, January 1973.

[15] D. N. Page and K. S. Thorne. Disk-Accretion onto a Black Hole. Time-Averaged Structure of Accretion Disk. *The Astrophysical Journal*, 191:499–506, July 1974.

[16] H. Riffert and H. Herold. Relativistic Accretion Disk Structure Revisited. *The Astrophysical Journal*, 450:508, September 1995.

[17] R. F. Penna, A. Sąowski, and J. C. McKinney. Thin-disc theory with a non-zero-torque boundary condition and comparisons with simulations. *MNRAS*, 420(1):684–698, February 2012.

[18] S. A. Balbus and J. F. Hawley. A Powerful Local Shear Instability in Weakly Magnetized Disks. I. Linear Analysis. *The Astrophysical Journal*, 376:214, July 1991.

[19] S. A. Balbus. Enhanced Angular Momentum Transport in Accretion Disks. *Annual Review of Astronomy & Astrophysics*, 41:555–597, January 2003.

[20] J. F. Hawley. Global Magnetohydrodynamical Simulations of Accretion Tori. *The Astrophysical Journal*, 528(1):462–479, January 2000.

[21] O. Porth, H. Olivares, Y. Mizuno, Z. Younsi, L. Rezzolla, M. Moscibrodzka, H. Falcke, and M. Kramer. The black hole accretion code. *Computational Astrophysics and Cosmology*, 4(1):1, May 2017.

[22] W. Ley. The Galactic Giants. "For Your Information". *Galaxy Science Fiction*, pages 130–142, 08 1965.

[23] S. Gillessen, F. Eisenhauer, S. Trippe, T. Alexander, R. Genzel, F. Martins, and T. Ott. Monitoring Stellar Orbits Around the Massive Black Hole in the Galactic Center. *The Astrophysical Journal*, 692(2):1075–1109, February 2009.

[24] A. M. Ghez, S. Salim, N. N. Weinberg, J. R. Lu, T. Do, J. K. Dunn, K. Matthews, M. R. Morris, S. Yelda, E. E. Becklin, T. Kremenek, M. Milosavljevic, and J. Naiman. Measuring Distance and Properties of the Milky Way's Central Supermassive Black Hole with Stellar Orbits. *The Astrophyiscal Journal*, 689(2):1044–1062, December 2008.

[25] Gravity Collaboration, R. Abuter, and A. Amorim *et al.* A geometric distance measurement to the Galactic center black hole with 0.3% uncertainty. *Astronomy & Astrophysics*, 625:L10, May 2019.

[26] H. Falcke, W. M. Goss, H. Matsuo, P. Teuben, J.-H. Zhao, and R. Zylka. The Simultaneous Spectrum of Sagittarius A* from 20 Centimeters to 1 Millimeter and the Nature of the Millimeter Excess. *The Astrophysical Journal*, 499(2):731–734, May 1998.

[27] R.-S. Lu, T. P. Krichbaum, A. L. Roy, V. L. Fish, S. S. Doeleman, M. D. Johnson, K. Akiyama, and D. Psaltis *et al.* Detection of Intrinsic Source Structure at ~3 Schwarzschild Radii with Millimeter-VLBI Observations of SAGITTARIUS A*. *The Astrophysical Journal*, 859(1):60, May 2018.

[28] S. Issaoun, M. D. Johnson, L. Blackburn, C. D. Brinkerink, M. Mości-brodzka, A. Chael, and C. Goddi *et al.* The Size, Shape, and Scattering of Sagittarius A* at 86 GHz: First VLBI with ALMA. *The Astrophysical Journal*, 871(1):30, January 2019.

[29] D. P. Marrone, J. M. Moran, J.-H. Zhao, and R. Rao. Interferometric Measurements of Variable 340 GHz Linear Polarization in Sagittarius A*. *The Astrophysical Journal*, 640(1):308–318, March 2006.

[30] G. C. Bower, S. Markoff, J. Dexter, M. A. Gurwell, J. M. Moran, A. Brunthaler, H. Falcke, P. C. Fragile, D. Maitra, D. Marrone, A. Peck, A. Rushton, and M. C. H. Wright. Radio and Millimeter Monitoring of Sgr A*: Spectrum, Variability, and Constraints on the G2 Encounter. *The Astrophysical Journal*, 802(1):69, March 2015.

[31] Yuhei Iwata, Tomoharu Oka, Masato Tsuboi, Makoto Miyoshi, and Shunya Takekawa. Time Variations in the Flux Density of Sgr A* at 230 GHz Detected with ALMA. *The Astrophysical Journal Letters*, 892(2):L30, April 2020.

[32] H. Falcke, F. Melia, and E. Agol. Viewing the Shadow of the Black Hole at the Galactic Center. *The Astrophysical Journal*, 528(1):L13–L16, January 2000.

[33] S. S. Doeleman, J. Weintroub, A. E. E. Rogers, R. Plambeck, and R. Freund *et al.* Event-horizon-scale structure in the supermassive black hole candidate at the Galactic Centre. *Nature*, 455(7209):78–80, September 2008.

[34] Event Horizon Telescope Collaboration, K. Akiyama, and A. Alberdi *et al.* First M87 Event Horizon Telescope Results. I. The Shadow of the Supermassive Black Hole. *The Astrophysical Journal Letters*, 875(1):L1, April 2019.

[35] Event Horizon Telescope Collaboration, K. Akiyama, and A. Alberdi *et al.* First M87 Event Horizon Telescope Results. II. Array and Instrumentation. *The Astrophysical Journal Letters*, 875(1):L2, April 2019.

[36] Event Horizon Telescope Collaboration, K. Akiyama, and A. Alberdi *et al.* First M87 Event Horizon Telescope Results. III. Data Processing and Calibration. *The Astrophysical Journal Letters*, 875(1):L3, April 2019.

[37] Event Horizon Telescope Collaboration, K. Akiyama, and A. Alberdi *et al.* First M87 Event Horizon Telescope Results. IV. Imaging the Central Supermassive Black Hole. *The Astrophysical Journal Letters*, 875(1):L4, April 2019.

[38] Event Horizon Telescope Collaboration, K. Akiyama, and A. Alberdi *et al.* First M87 Event Horizon Telescope Results. V. Physical Origin of the Asymmetric Ring. *The Astrophysical Journal Letters*, 875(1):L5, April 2019.

[39] Event Horizon Telescope Collaboration, K. Akiyama, and A. Alberdi *et al.* First M87 Event Horizon Telescope Results. VI. The Shadow and Mass of the Central Black Hole. *The Astrophysical Journal Letters*, 875(1):L6, April 2019.

[40] R. Narayan, I. Yi, and R. Mahadevan. Explaining the spectrum of Sagittarius A* with a model of an accreting black hole. *Nature*, 374(6523):623–625, April 1995.

[41] H. Falcke, K. Mannheim, and P. L. Biermann. The Galactic Center radio jet. *Astronomy & Astrophysics*, 278:L1–L4, October 1993.

[42] F. Yuan, S. Markoff, and H. Falcke. A Jet-ADAF model for Sgr A*. *Astronomy & Astrophysics*, 383:854–863, March 2002.

[43] P. K. Leung, C. F. Gammie, and S. C. Noble. Numerical Calculation of Magnetobremsstrahlung Emission and Absorption Coefficients. *The Astrophysical Journal*, 737(1):21, August 2011.

[44] A. R. Thompson, J. M. Moran, and Jr. Swenson, G. W. *Interferometry and Synthesis in Radio Astronomy, 3rd Edition*. 2017.

[45] A. A. Chael, M. D. Johnson, K. L. Bouman, L. L. Blackburn, K. Akiyama, and R. Narayan. Interferometric Imaging Directly with Closure Phases and Closure Amplitudes. *The Astrophysical Journal*, 857(1):23, April 2018.

[46] Z. Wang, A. C. Bovik, H. R. Sheikh, and E. P. Simoncelli. Image quality assessment: from error visibility to structural similarity. *IEEE Transactions on Image Processing*, 13(4):600–612, 2004.

[47] Z. Wang and A. C. Bovik. A universal image quality index. *IEEE Signal Processing Letters*, 9(3):81–84, 2002.

[48] Y. Mizuno, Z. Younsi, C. M. Fromm, O. Porth, M. De Laurentis, H. Olivares, H. Falcke, M. Kramer, and L. Rezzolla. The current ability to test theories of gravity with black hole shadows. *Nature Astronomy*, 2:585–590, April 2018.

[49] A. A. Chael, M. D. Johnson, R. Narayan, S. S. Doeleman, J. F. C. Wardle, and K. L. Bouman. High-resolution Linear Polarimetric Imaging for the Event Horizon Telescope. *The Astrophysical Journal*, 829(1):11, September 2016.

[50] R. H. Byrd, P. Lu, J. Nocedal, and C. Zhu. A limited memory algorithm for bound constrained optimization. *SIAM Journal on Scientific Computing*, 16(5):1190–1208, 1995.

[51] P. Virtanen, R. Gommers, T. E. Oliphant, and M. Haberland *et al.* SciPy 1.0: Fundamental Algorithms for Scientific Computing in Python. *Nature Methods*, 17:261–272, 2020.

[52] A. Einstein. Zur Elektrodynamik bewegter Körper. *Annalen der Physik*, 322(10):891–921, January 1905.

[53] M. P. Haugan and C. Lämmerzahl. *Principles of Equivalence: Their Role in Gravitation Physics and Experiments That Test Them*, volume 562, page 195. 2001.

[54] A. Einstein. Die Feldgleichungen der Gravitation. *Sitzungsberichte der Königlich Preußischen Akademie der Wissenschaften (Berlin*, pages 844–847, January 1915.

[55] R. P. Kerr. Gravitational Field of a Spinning Mass as an Example of Algebraically Special Metrics. *Physical Review Letters*, 11(5):237–238, September 1963.

[56] L. Rezzolla and O. Zanotti. *Relativistic Hydrodynamics*. Oxford University Press, 2013.

[57] J. C. McKinney and C. F. Gammie. A Measurement of the Electromagnetic Luminosity of a Kerr Black Hole. *The Astrophysical Journal*, 611(2):977–995, August 2004.

[58] T. E. Collett, L. J. Oldham, R. J. Smith, M. W. Auger, K. B. Westfall, D. Bacon, R. C. Nichol, K. L. Masters, K. Koyama, and R. van den Bosch. A precise extragalactic test of General Relativity. *Science*, 360(6395):1342–1346, June 2018.

[59] C. M. Will. The Confrontation between General Relativity and Experiment. *Living Reviews in Relativity*, 17(1):4, December 2014.

[60] J. H. Taylor and J. M. Weisberg. A new test of general relativity - Gravitational radiation and the binary pulsar PSR 1913+16. *The Astrophysical Journal*, 253:908–920, February 1982.

[61] A. Held, R. Gold, and A. Eichhorn. Asymptotic safety casts its shadow. *Journal of Cosmology and Astroparticle Physics*, 2019(6):029, June 2019.

[62] S. A. Hayward. Formation and Evaporation of Nonsingular Black Holes. *Physical Review Letters*, 96(3):031103, January 2006.

[63] V. P. Frolov. Notes on nonsingular models of black holes. *Physical Review D*, 94(10):104056, November 2016.

[64] P. Berglund, J. Bhattacharyya, and D. Mattingly. Mechanics of universal horizons. *Physical Review D*, 85(12):124019, June 2012.

[65] A. García, D. Galtsov, and O. Kechkin. Class of Stationary Axisymmetric Solutions of the Einstein-Maxwell-Dilaton-Axion Field Equations. *Physical Review Letters*, 74(8):1276–1279, February 1995.

[66] D. I. Kazakov and S. N. Solodukhin. On quantum deformation of the Schwarzschild solution. *Nuclear Physics B*, 429(1):153–176, October 1994.

[67] G. W. Gibbons and K.-I. Maeda. Black holes and membranes in higher-dimensional theories with dilaton fields. *Nuclear Physics B*, 298(4):741–775, March 1988.

[68] R. Casadio, A. Fabbri, and L. Mazzacurati. New black holes in the brane world? *Physical Review D*, 65(8):084040, April 2002.

[69] P. Kocherlakota and L. Rezzolla. Accurate mapping of spherically symmetric black holes in a parametrized framework. *Physical Review D*, 102(6):064058, September 2020.

[70] T. Johannsen and D. Psaltis. Metric for rapidly spinning black holes suitable for strong-field tests of the no-hair theorem. *Physical Review D*, 83(12):124015, June 2011.

[71] R. Konoplya, L. Rezzolla, and A. Zhidenko. General parametrization of axisymmetric black holes in metric theories of gravity. *Physical Review D*, 93(6):064015, March 2016.

[72] L. Rezzolla and A. Zhidenko. New parametrization for spherically symmetric black holes in metric theories of gravity. *Physical Review D*, 90(8):084009, October 2014.

[73] H. Olivares, Z. Younsi, C. M. Fromm, M. De Laurentis, O. Porth, Y. Mizuno, H. Falcke, M. Kramer, and L. Rezzolla. How to tell an accreting boson star from a black hole. *MNRAS*, 497(1):521–535, July 2020.

[74] M. Grould, Z. Meliani, F. H. Vincent, P. Grandclément, and E. Gourgoulhon. Comparing timelike geodesics around a Kerr black hole and a boson star. *Classical and Quantum Gravity*, 34(21):215007, November 2017.

[75] F. H. Vincent, Z. Meliani, P. Grandclément, E. Gourgoulhon, and O. Straub. Imaging a boson star at the Galactic center. *Classical and Quantum Gravity*, 33(10):105015, May 2016.

[76] A. I. Janis, E. T. Newman, and J. Winicour. Reality of the Schwarzschild Singularity. *Physical Review Letters*, 20(16):878–880, April 1968.

[77] S.-W. Wei and Y.-X. Liu. Observing the shadow of Einstein-Maxwell-Dilaton-Axion black hole. *Journal of Cosmology and Astroparticle Physics*, 2013(11):063, November 2013.

[78] K. Hioki and K.-I. Maeda. Measurement of the Kerr spin parameter by observation of a compact object's shadow. *Physical Review D*, 80(2):024042, July 2009.

[79] T. Damour and A. M. Polyakov. The String dilaton and a least coupling principle. *Nucl. Phys. B*, 423:532–558, 1994.

[80] J. M. Bardeen, W. H. Press, and S. A. Teukolsky. Rotating Black Holes: Locally Nonrotating Frames, Energy Extraction, and Scalar Synchrotron Radiation. *The Astrophysical Journal*, 178:347–370, December 1972.

[81] M. Mościbrodzka, H. Falcke, and H. Shiokawa. General relativistic magneto-hydrodynamical simulations of the jet in M 87. *Astronomy & Astrophysics*, 586:A38, February 2016.

[82] J. Davelaar, H. Olivares, O. Porth, T. Bronzwaer, M. Janssen, F. Roelofs, Y. Mizuno, C. M. Fromm, H. Falcke, and L. Rezzolla. Modeling non-thermal emission from the jet-launching region of M 87 with adaptive mesh refinement. *Astronomy & Astrophysics*, 632:A2, December 2019.

[83] S. M. Ressler, C. J. White, E. Quataert, and J. M. Stone. Ab Initio Horizon-scale Simulations of Magnetically Arrested Accretion in Sagittarius A* Fed by Stellar Winds. *The Astrophysical Journal Letters*, 896(1):L6, June 2020.

[84] G. B. Rybicki and A. P. Lightman. *Radiative Processes in Astrophysics*. Wiley-VCH, 1986.

[85] A Pandya, Z. Zhang, M. Chandra, and C. F. Gammie. Polarized Synchrotron Emissivities and Absorptivities for Relativistic Thermal, Power-law, and Kappa Distribution Functions. *The Astrophysical Journal*, 822(1):34, May 2016.

[86] V. M. Vasyliunas. A survey of low-energy electrons in the evening sector of the magnetosphere with ogo 1 and ogo 3. *Journal of Geophysical Research (1896-1977)*, 73(9):2839–2884, 1968.

[87] C. Tsallis. Possible generalization of boltzmann-gibbs statistics. *Journal of Statistical Physics*, 52(1):479–487, Jul 1988.

[88] C. Tsallis, R. S. Mendes, and A. R. Plastino. The role of constraints within generalized nonextensive statistics. *Physica A Statistical Mechanics and its Applications*, 261(3):534–554, January 1998.

[89] G. Livadiotis and D. J. McComas. Beyond kappa distributions: Exploiting tsallis statistical mechanics in space plasmas. *Journal of Geophysical Research: Space Physics*, 114(A11), 2009.

[90] F. Xiao. Modelling energetic particles by a relativistic kappa-loss-cone distribution function in plasmas. *Plasma Physics and Controlled Fusion*, 48(2):203–213, February 2006.

[91] J. Davelaar, M. Mościbrodzka, T. Bronzwaer, and H. Falcke. General relativistic magnetohydrodynamical κ-jet models for Sagittarius A*. *Astronomy & Astrophysics*, 612:A34, April 2018.

[92] D. Ball, L. Sironi, and F. Özel. Electron and Proton Acceleration in Trans-relativistic Magnetic Reconnection: Dependence on Plasma Beta and Magnetization. *The Astrophysical Journal*, 862(1):80, July 2018.

[93] J. Dexter. A public code for general relativistic, polarised radiative transfer around spinning black holes. *MNRAS*, 462(1):115–136, October 2016.

[94] H. Y. Pu, K. Yun, Z. Younsi, and S. J. Yoon. Odyssey: A Public GPU-based Code for General Relativistic Radiative Transfer in Kerr Spacetime. *The Astrophysical Journal*, 820(2):105, April 2016.

[95] S. V. Fuerst and K. Wu. Radiation transfer of emission lines in curved space-time. *Astronomy & Astrophysics*, 424:733–746, September 2004.

[96] X. Yang and J. Wang. YNOGK: A New Public Code for Calculating Null Geodesics in the Kerr Spacetime. *The Astrophysical Journal Supplement*, 207(1):6, July 2013.

[97] C. k. Chan, D. Psaltis, and F. Özel. GRay: A Massively Parallel GPU-based Code for Ray Tracing in Relativistic Spacetimes. *The Astrophysical Journal*, 777(1):13, November 2013.

[98] Z. Younsi, A. Zhidenko, L. Rezzolla, R. Konoplya, and Y. Mizuno. New method for shadow calculations: Application to parametrized axisymmetric black holes. *Physical Review D*, 94(8):084025, October 2016.

[99] C. W. Misner, K. S. Thorne, and J. A. Wheeler. *Gravitation*. San Francisco: W.H. Freeman and Co., 1973.

[100] O. Porth, C. Xia, T. Hendrix, S. P. Moschou, and R. Keppens. MPI-AMRVAC FOR SOLAR AND ASTROPHYSICS. *The Astrophysical Journal Supplement Series*, 214(1):4, aug 2014.

[101] R. Keppens, Z. Meliani, A.J. van Marle, P. Delmont, A. Vlasis, and B. van der Holst. Parallel, grid-adaptive approaches for relativistic hydro and magnetohydrodynamics. *Journal of Computational Physics*, 231(3):718 – 744, 2012. Special Issue: Computational Plasma Physics.

[102] O. Porth, K. Chatterjee, and Event Horizon Telescope Collaboration *et al.* The Event Horizon General Relativistic Magnetohydrodynamic Code Comparison Project. *The Astrophysical Journal Supplement Series*, 243(2):26, August 2019.

[103] Z. Meliani, Y. Mizuno, H. Olivares, O. Porth, L. Rezzolla, and Z. Younsi. Simulations of recoiling black holes: adaptive mesh refinement and radiative transfer. *Astronomy & Astrophysics*, 598:A38, Jan 2017.

[104] F. Daigne and J. A. Font. The runaway instability of thick discs around black holes - II. Non-constant angular momentum discs. *MNRAS*, 349(3):841–868, April 2004.

[105] J. A. Font and F. Daigne. The runaway instability of thick discs around black holes - I. The constant angular momentum case. *MNRAS*, 334(2):383–400, August 2002.

[106] B. Ripperda, F. Bacchini, and A. A. Philippov. Magnetic Reconnection and Hot Spot Formation in Black Hole Accretion Disks. *The Astrophysical Journal*, 900(2):100, September 2020.

[107] R. Narayan, A. SÄ dowski, R. F. Penna, and A. K. Kulkarni. GRMHD simulations of magnetized advection-dominated accretion on a non-spinning black hole: role of outflows. *MNRAS*, 426(4):3241–3259, November 2012.

[108] E. Fehlberg. Low order Runge-Kutta formulas with step control for heat transfer problems. Technical report, NASA Marshall Space Flight Center, July 1969.

[109] M. Mościbrodzka and H. Falcke. Coupled jet-disk model for Sagittarius A*: explaining the flat-spectrum radio core with GRMHD simulations of jets. *Astronomy & Astrophysics*, 559:L3, November 2013.

[110] J. Dexter, A. Jiménez-Rosales, S. M. Ressler, A. Tchekhovskoy, M. Bauböck, P. T. de Zeeuw, F. Eisenhauer, S. von Fellenberg, F. Gao, R. Genzel, S. Gillessen, M. Habibi, T. Ott, J. Stadler, O. Straub, and F. Widmann. A parameter survey of Sgr A* radiative models from GRMHD simulations with self-consistent electron heating. *MNRAS*, 494(3):4168–4186, April 2020.

[111] M. D. Johnson. Stochastic Optics: A Scattering Mitigation Framework for Radio Interferometric Imaging. *The Astrophysical Journal*, 833(1):74, December 2016.

[112] A. E. Broderick and A. Loeb. Imaging optically-thin hotspots near the black hole horizon of Sgr A* at radio and near-infrared wavelengths. *MNRAS*, 367(3):905–916, April 2006.

[113] T. Bronzwaer, J. Davelaar, Z Younsi, M. Mościbrodzka, H. Olivares, Y. Mizuno, J. Vos, and H. Falcke. Visibility of Black Hole Shadows in Low-luminosity AGN. *MNRAS*, November 2020.

[114] M. Mościbrodzka and C. F. Gammie. IPOLE - semi-analytic scheme for relativistic polarized radiative transport. *MNRAS*, 475(1):43–54, March 2018.

[115] Z. Younsi, O. Porth, Y. Mizuno, C. M. Fromm, and H. Olivares. Modelling the polarised emission from black holes on event horizon-scales. In Kieechi Asada, Elisabete de Gouveia Dal Pino, Marcello Giroletti, Hiroshi Nagai, and Rodrigo Nemmen, editors, *IAU Symposium*, volume 342 of *IAU Symposium*, pages 9–12, January 2020.

[116] M. D. Johnson, K. L. Bouman, L. Blackburn, A. A. Chael, J. Rosen, H. Shiokawa, F. Roelofs, K. Akiyama, V. L. Fish, and S. S. Doeleman. Dynamical Imaging with Interferometry. *The Astrophysical Journal*, 850(2):172, December 2017.

[117] M. A. Gruntman. Anisotropy of the energetic neutral atom flux in the heliosphere. *Planetary and Space Science*, 40(4):439–445, April 1992.

[118] C. M. Hammond, W. C. Feldman, J. L. Phillips, B. E. Goldstein, and A. Balogh. Solar wind double ion beams and the heliospheric current sheet. *Journal of Geophysical Research*, 100(A5):7881–7890, May 1995.

[119] R. Silva Jr., A. R. Plastino, and J. A. S. Lima. A Maxwellian path to the q-nonextensive velocity distribution function. *Physics Letters A*, 249(5-6):401–408, December 1998.

[120] R. B. Decker, S. M. Krimigis, E. C. Roelof, M. E. Hill, T. P. Armstrong, G. Gloeckler, D. C. Hamilton, and L. J. Lanzerotti. Voyager 1 in the Foreshock, Termination Shock, and Heliosheath. *Science*, 309(5743):2020–2024, September 2005.

[121] L. A. Fisk and G. Gloeckler. The Common Spectrum for Accelerated Ions in the Quiet-Time Solar Wind. *The Astrophysical Journal*, 640(1):L79–L82, March 2006.

[122] S. Abe and Y. Okamoto. *Nonextensive Statistical Mechanics and Its Application. Lecture Notes in Physics*, volume 560. Springer-Verlag, Berlin, New York, 2001.

[123] S. Martínez, F. Nicolás, F. Pennini, and A. Plastino. Tsallis' entropy maximization procedure revisited. *Physica A Statistical Mechanics and its Applications*, 286(3):489–502, November 2000.

[124] R. A. Treumann. Generalized-Lorentzian Thermodynamics. *Physica Scripta*, 59(3):204–214, January 1999.

[125] E. W. Montroll and M. F. Shlesinger. Maximum entropy formalism, fractals, scaling phenomena, and 1/ f noise: A tale of tails. *Journal of Statistical Physics*, 32(2):209–230, August 1983.

[126] M. Gell-Mann and C. Tsallis. *Nonextensive Entropy - Interdisciplinary Applications*. Oxford University Press, 2004.

[127] C. Beck and F. Schlogl. Books-Received - Thermodynamics of Chaotic Systems - an Introduction. *Science*, 262:2073, December 1993.

[128] C. Tsallis. Nonextensive Statistics: Theoretical, Experimental and Computational Evidences and Connections. *Brazilian Journal of Physics*, 29(1):01–35, March 1999.

Statutory Declaration

I herewith declare that I have composed the present thesis myself and without use of any other than the cited sources and aids. Sentences or parts of sentences quoted literally are marked as such; other references with regard to the statement and scope are indicated by full details of the publications concerned. The thesis in the same or similar form has not been submitted to any examination body and has not been published. This thesis was not yet, even in part, used in another examination or as a course performance.

Place, Date   Jan Röder

Eidesstattliche Erklärung

Ich versichere hiermit, dass ich die vorliegende Arbeit selbständig und ohne Benutzung anderer als der angegebenen Quellen und Hilfsmittel verfasst habe.
Wörtlich übernommene Sätze oder Satzteile sind als Zitat belegt, andere Anlehnungen, hinsichtlich Aussage und Umfang, unter Quellenangabe kenntlich gemacht. Die Arbeit hat in gleicher oder ähnlicher Form noch keiner Prüfungsbehörde vorgelegen und ist nicht veröffentlicht. Sie wurde nicht, auch nicht auszugsweise, für eine andere Prüfungs- oder Studienleistung verwendet.

Ort, Datum   Jan Röder